論文 / 著書情報
Article / Book Information

題目(和文)	
Title(English)	How are the core and mantle speaking to each other? A hybrid approach towards core-mantle interaction
著者(和文)	LIM Kang Wei
Author(English)	Lim Kang Wei
出典(和文)	学位:博士(理学), 学位授与機関:東京工業大学, 報告番号:甲第11706号, 授与年月日:2022年3月26日, 学位の種別:課程博士, 審査員:HERNLUND JOHN WILLIA,横山 哲也,井田 茂,玄田 英典,太田 健二
Citation(English)	Degree:Doctor (Science), Conferring organization: Tokyo Institute of Technology, Report number:甲第11706号, Conferred date:2022/3/26, Degree Type:Course doctor, Examiner:,,,,
学位種別(和文)	博士論文
Type(English)	Doctoral Thesis

東京工業大学
Tokyo Institute of Technology

EARTH-LIFE SCIENCE INSTITUTE
TOKYO INSTITUTE OF TECHNOLOGY

HOW ARE THE CORE AND MANTLE SPEAKING TO EACH OTHER?

A HYBRID APPROACH TOWARDS CORE-MANTLE INTERACTION

KANG WEI LIM

DOCTORAL THESIS

Submitted in accordance with the requirements for the degree of

Doctor of Philosophy (Ph.D.)

Department of Earth and Planetary Sciences

Tokyo Institute of Technology

東京工業大学

Committee members

Prof. Dr. John W. Hernlund (supervisor)	Tokyo Institute of Technology (Japan)
Prof. Dr. Shigeru Ida (examiner)	Tokyo Institute of Technology (Japan)
Prof. Dr. Hidenori Genda (examiner)	Tokyo Institute of Technology (Japan)
Prof. Dr. Kenji Ohta (examiner)	Tokyo Institute of Technology (Japan)
Prof. Dr. Tetsuya Yokoyama (examiner)	Tokyo Institute of Technology (Japan)

2022

Abstract

The core and mantle of the Earth are known to be chemically and physically distinct, especially since the outer core is composed of a liquid iron alloy while the mantle is largely made of rocks containing silicates and oxides. As a result, many questions have been raised regarding the extent of chemical and physical interactions between these two domains at the core mantle boundary (CMB), as well as the connections with seismic anomalies that have been detected around the region. Recent detection of chemical signatures from the CMB have been thought to provide an unprecedented glimpse into the Earth's deep interior and ancient past. Although several isotopic and elemental anomalies in ocean island basalts (OIBs) have been proposed as core tracers, the process(es) by which particular chemical signatures from the core are conveyed into the mantle still remains uncertain.

To establish a broader framework for understanding the connection between potential processes operating at the CMB, proposed geochemical tracers of core-mantle interaction (such as μ^{182}W, ^{3}He/^{4}He, and D/H) and their dependence on physical properties at CMB conditions, a comprehensive review of the geochemical evidence, mineral physics, and previously proposed core-mantle interaction mechanisms are presented in the first chapter. Numerous core-mantle interaction mechanisms have been proposed to date, but not many have been able to explain the accompanying geochemical evidence satisfactorily. Hence, a new emergent mechanism for core-mantle interaction is proposed that results from a nonlinear combination of mechanisms that can operate in the deep mantle. This new hybrid mechanism termed "soft CMB" results from collaborative feedback between dynamic topography, porous infiltration of liquid metal into submerged rock, gravitational collapse of weakened metal-silicate mush, and draw-down of additional rocks from the mantle above in the induced small-scale mantle circulation.

Subsequent chapters delve deeper into the equations modelling this hybrid mechanism, followed by investigating the impacts on mantle dynamics using mantle convection models coupled to gravitational spreading of a thin layer at the CMB. The second chapter describes a basic illustrative model where the mechanism operates in the context of an isoviscous mantle, and results show that the induced mantle circulation due to the gravitational collapse of the layer becomes comparable to buoyancy-driven mantle flow when the viscosity of the mushy layer is almost 10^5 times smaller than the overlying mantle. In addition, enhanced flow into the layer becomes weaker with increasing convective strength of the mantle.

The next chapter looks at the hybrid mechanism in context of a variable viscosity mantle where viscosity depends on temperature, and results show that increasing both the strength of temperature dependence of viscosity and the reference viscosity reduce the efficiency of the "soft CMB" mechanism. This suggests that it is unlikely for the mechanism to be the dominant interaction mechanism in the early Earth when temperatures in the mantle were much higher, resulting in lower viscosities and more vigorous convection. Only after the mantle has cooled further and increased its viscosity will the mechanism be more efficient. Moreover, to understand the implications this new mechanism has on the composition of

the lower mantle, numerical simulations of thermochemical convection are performed where discrete tracer particles are used to track compositional changes of material that has undergone exchange within the mushy layer. The flux of particles that emerge from the exchange can serve as a proxy for the expected amount of mantle material that undergoes significant chemical interaction with the core. Numerical calculations were performed for reacted tracer particles with positive, neutral and negative buoyancy.

Finally, the limitations of the mechanism, a quick summary comparing the different core-mantle interaction mechanisms so far, as well as potential ideas and future research directions that can extend the ideas presented in this dissertation are discussed.

Publications associated with this dissertation

Parts of this thesis have appeared in the following publications and preprints:

- Chapter 2: **Lim, K. W.**, Bonati, I., & Hernlund, J. W. (2021). A hybrid mechanism for enhanced core-mantle boundary chemical interaction. Geophysical Research Letters, 48, e2021GL094456. https://doi.org/10.1029/2021GL094456

Declaration of Authorship

I, Kang Wei LIM, declare that this thesis titled, "HOW ARE THE CORE AND MANTLE SPEAKING TO EACH OTHER?: A HYBRID APPROACH TOWARDS CORE-MANTLE INTERACTION" and the work presented in it are my own. I confirm that:

- This work was done wholly while in candidature for a research degree at Tokyo Institute of Technology.
- Where I have consulted the published work of others, this is always clearly attributed.
- Where I have quoted from the work of others, the source is always given.
- I have acknowledged all main sources of help.
- Where the thesis is based on work done by myself jointly with others, I have made clear exactly what was done by others and what I have contributed myself.

Signature: Lim Kang Wei

Date: 01 March 2022

Acknowledgements

During the 10 years of primary to post-secondary education in Singapore, never had it crossed my mind that my journey from the first day in university to finishing my PhD would span three across cities in three different countries. Moving to different parts of the world is no easy feat and definitely requires stepping out of my comfort zone many times. With every challenging and exciting moment that I have came across over the past 8 years, I am grateful for all the experiences I have been through regardless good or bad. However, one thing is for certain and that is if I have remained in Singapore for my university studies, I would not have known the amazing world of geosciences and have a true appreciation of what nature is truly capable of. Pursuing a PhD is no easy feat, even more so when everything is happening in the midst of a global pandemic, and doing it alone is next to impossible. Hence, I would like to thank the following people who have helped me on this journey.

First and foremost, being able to pursue my PhD at ELSI has been a great privilege and wonderful opportunity. It was my first time being part of a world class institute that prides itself on interdisciplinary research and being able to witness many incredible scientific achievements has been nothing but inspiring. This has not been possible without John, and I would like to sincerely thank him for welcoming me and introducing me to ELSI. Thank you, John, for your unwavering support throughout these three years. Your experiences and knowledge about the world of science has been invaluable and although I am not the best student one could ask for, I am immensely thankful for your patience and guidance whenever I needed help. I am also thankful to both you and Christine for the insightful discussions about the world of academia and earth sciences over the lunches we had.

I would also like to thank the thesis committee members for accepting to vet my work and for reading through this thesis.

A big thank you to the secretaries and administrative staff, especially Tamai-san and Sato-san, for their tireless support while I was in ELSI. Thank you for accompanying me to different places when I needed help with the language and especially to Sato-san who has helped me with coming back to Japan halfway amid the travel restrictions so that I can finish my PhD as smoothly as possible. I would also like to take this chance to thank Sekine-san and Genda-san for taking part in my MEXT interview so that I can continue to receive their scholarship during my studies.

Thank you to the best seniors one could possibly ask for: Irene and Jingyi. Without your guidance and relaying your experiences of student life in Tokyo Tech, I would definitely have had a much more difficult time navigating through the school and its curriculum requirements. Thank you to Su Jun for being part of the group and helping out with all things related to Tsubame. Thank you to the Singaporean students studying in Tokyo as well for

the fun times over karaoke and good food; it is always good to have some reminder of home despite being so far away.

Finally, a really big thank you to my family, Dad and Mum, as well as my brother and sister, for believing in me and letting me go down this unfamiliar path not many have taken. The incredible amount of support and love I have received from everyone over the years has been very, very immense which I am truly grateful for every day because nothing today is possible without them.

Contents

List of Figures

List of Tables

linenumbers

1 Introduction

1.1 Background

Ever since the beginning of early human civilisation, philosophers, scientific scholars, and religious institutions have been intrigued by the Earth. Even though this planet has always been what we call home, questions regarding its origins, composition, and evolution have been constantly pondered by mankind over millennia. We have come a long way since then, from the development of creation and cosmological myths in the beginning to extraordinary advances in scientific methods and technology that have allowed us to probe the secrets of the Earth over space and time with increasing precision. However, despite the vast amounts of knowledge that has been discovered and gathered over the past century, there are many important questions that are still unanswered, especially when new discoveries seek to challenge our current perception of how the Earth “works" so far.

In this introductory chapter, a brief history of the Earth’s formation will be presented first to provide a background for the thesis topic. This will be followed by a description of unique chemical signatures detected from lavas around the world that have been alluded to core-mantle interaction, followed by a discussion of the various core-mantle interaction mechanisms that have been presented in the literature so far. Finally, an introduction of a new hybrid core-mantle interaction mechanism will be presented.

1.1.1 Earth: The Beginning

With incredibly powerful telescopes we have today, astronomical observations of active star-forming regions and protoplanetary disks have allowed us to piece together a theory of how the solar system and planets like the Earth came about. It is hypothesised that the solar system originated from a giant nebula of gas and dust, which gradually collapsed under its own gravity. Mass falling towards the centre of the nebula accompanied with increasing temperature and pressure eventually formed the protosun, while other material with sufficient angular velocities began to orbit around it. The material surrounding the protosun eventually created a proptoplanetary disk of dust and gas which contained the building blocks of the planets in the solar system.

All terrestrial planets, including the Earth, are believed to have been built from planetesimals that have aggregated within the protoplanetary disk through a process called accretion. The entire accretion mechanism of planets is still not well understood, largely due to the complex dynamics involved in the aggregation of particles and the complicated gravitational interactions that are involved, but it is likely that the terrestrial planets were formed within the timescales of the order of $10^7 - 10^8$ years (Wetherill, 1986). A survey of a group of T Tauri stars (stars with ages < 10 Ma) has shown that the amount of disk material decreases exponentially over time (Mamajek, 2009) and by the time the host star is ~ 10 Ma old, much of the dust and gas in the disk has disappeared due to the formation of gas giant planets and absorption by the host star. Since the composition of the Earth is mostly rocky with the presence of some volatiles, it is likely that most of the Earth's growth occurred after 10^6 to 10^7 years when much of the nebular gas has already disappeared (Haisch Jr et al., 2001). This is further supported by the composition of Earth's volatile elements, where correlations are observed with CI chondrites and the pronounced depletion of noble gasses like helium and neon relative to solar composition (Halliday, 2013). Despite the observed correlations, Earth's volatiles were not acquired in chondritic proportions as seen from the strong depletion of major volatiles H, C, N, and Xe and comparatively milder depletion of noble gases (2013). This depletion could also be a result of atmospheric erosion due impacts by planetesimals (Cameron, 1983; Ahrens, 1993; Schlichting & Mukhopadhyay, 2018). Some noble gas signatures that seem solar-like have been found in lavas on Earth, but their origins are still actively debated. These observations and the implications they have on Earth's deep interior will be discussed further in subsequent sections. Isotopic studies of iron meteorites (Halliday & Kleine, 2006) and detrital zircons (Valley et al., 2002; Harrison, 2009) have shown that the timescale Earth's accretion was rather protracted ~ 50 Ma, giving rise to the possibility that towards the end of Earth's formation, the planet was blanketed by hot dense atmosphere of remnant nebular gas. Should this atmosphere be optically opaque, most of the heat radiated from the planet will be retained, leading to magma oceans on Earth (Hayashi et al., 1979; Abe & Matsui, 1985; Zahnle et al., 1988; Sasaki, 1990).

1.1.2 Magma Ocean

Several lines of geochemical evidence point to the existence of a terrestrial magma ocean or occurrences of some large-scale melting events during the history of Earth's formation (Urey, 1955; Lee et al., 1976; LaTourrette & Wasserburg, 1998; Rizo et al., 2013). One of which is the chemical differentiation of Earth's mantle where the major element composition of the upper mantle is different from that of the lower mantle, in particular the ratios of Mg/Si and Mg/Fe. With the definition of the boundary between the upper and lower mantle being the spinel-perovskite transition, it has been well known that the upper mantle is superchondritic based on elevated Mg/Si ratios found in peridotitic rocks (Jagoutz et al., 1979; Ringwood, 1979; McDonough & Sun, 1995). This was initially thought to have been caused by fractional crystallisation of deep magma ocean, resulting in perovskite and silicate melts enriched with Mg-olivine being the major components in the lower and upper mantle respectively (Ohtani, 1985; Ohtani & Sawamoto, 1987; Agee & Walker, 1988). High pressure and

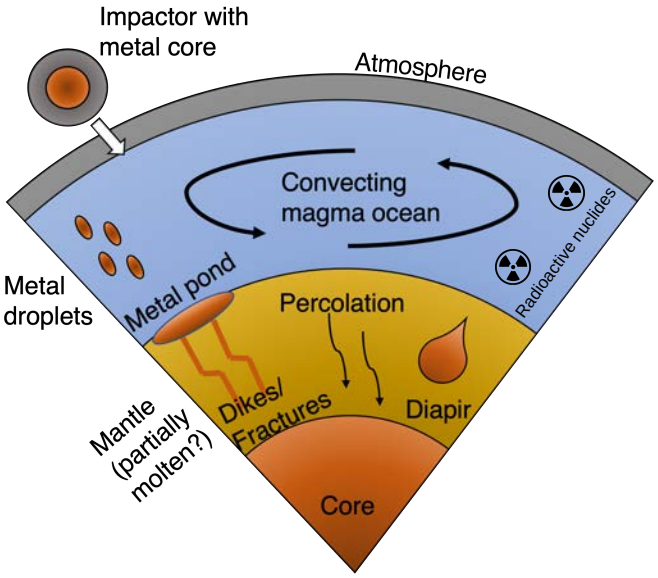

FIGURE 1.1: A cartoon depicting the processes that occur within the magma ocean during Earth's accretion and the main sources of heat that drive melting of the planet. As the silicate melts and liquid metal undergo segregation, chemical equilibration can occur during the liquid metal's descent into the core of the Earth. At the same time, the amount of gravitational potential energy released from segregation can heat significant portions of the mantle and create melts.

temperature experiment results have shown that in order to be consistent with the chondritic amount of refractory lithophile elements in the upper mantle, the amount of perovskite fractionation in the lower mantle is constrained between 5% to 17% with Ca-perovskite being the major host for rare earth elements and large ion lithophile elements (Corgne & Wood, 2002; Hirose et al., 2004; Corgne et al., 2005).

Another evidence that indicate the possibility of the existence of magma oceans during Earth's early history lies in the $^{142}Nd/^{144}Nd$ and $^{143}Nd/^{144}Nd$ isotope ratios of crustal rocks. These rocks obtained from different terrestrial sources, such as kimberlites, mid-ocean ridge basalts (MORBs), carbonatites, and Archean cratons have shown both Nd ratios to be larger than chondritic values (Harper & Jacobsen, 1992; Boyet & Carlson, 2005; Caro et al., 2006). To explain this observation, either the Earth was non-chondritic to begin with, or there is a hidden reservoir that is enriched somewhere in the mantle containing specific Nd ratios such that the overall value of the Earth is actually chondritic (Boyet et al., 2003; Caro et al., 2003; Boyet & Carlson, 2006). Geochemical models have also shown that it is possible for the continental and oceanic crusts to be derived from a reservoir depleted in incompatible elements that was formed by silicate differentiation in a magma ocean (Carlson & Boyet, 2008).

In order to form a magma ocean, there has to be sufficient heat available that can melt significant portions of the planet (Fig 1.1). Thus, there are 3 possible heat sources that can potentially generate significant melting: (1) heat from radioactive decay, (2) impacts with planetary embryos and Moon- to Mars-sized planets, and (3) core formation.

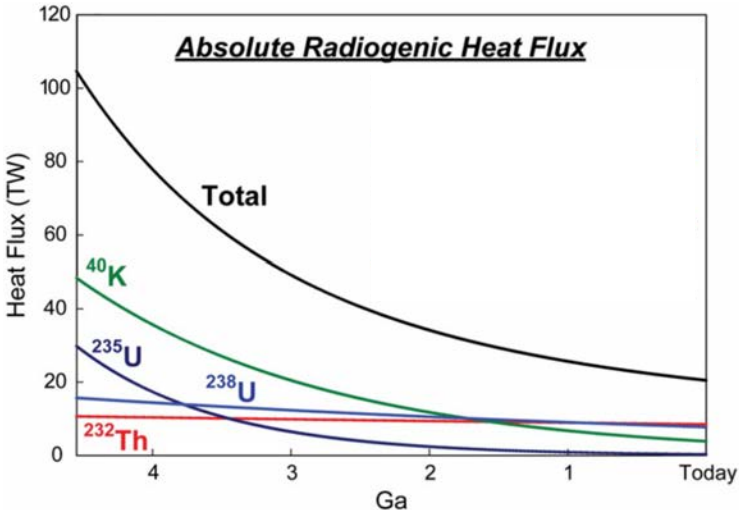

FIGURE 1.2: Earth's radiogenic heat production from the decay of long-lived radionucldies as a function of time. Figure modified from Arevalo Jr et al. (2009).

Radioactive Heat Decay

During the early history of the solar system, it is likely that there have been an abundance of short-lived radiogenic isotopes that produced various amounts of heat during its decay. Although most of these primordial isotopes do not exist today due to their relatively short half-lives, the nature of these isotopes can be identified from their daughter products found today. One of these important radiogenic isotopes is ^{26}Al, which decays into ^{26}Mg with a half-life of $\sim$0.7 Ma (MacPherson et al., 1995). Based on the the excess amount of ^{26}Mg found in meteorites, it is believed that the early Earth would have contained an abundant amount of ^{26}Al (Gray & Compston, 1974; Lee et al., 1976). This would have been in addition to the long-lived radiogenic heat-producing isotopes that still exist today – ^{238}U, ^{235}U, ^{40}K, and ^{232}Th – but more abundant in the early solar system (Arevalo Jr et al., 2009). As a result, the amount of heat that was available from radioactive decay during the early Earth would have been much higher (fig 1.2).

Impact-Induced Heating

While the Earth was growing from a protoplanet, heat that was transformed from kinetic energy during accretionary impacts was also a significant heat source that could create melt ponds and magma oceans on the surface (Davies, 1985; Melosh, 1990b; Tonks & Melosh, 1993). Compared to the short timescales of heat producing radioactive isotopes, accretionary impacts can occur over significantly longer timescales ($\sim$10-100 Ma) (Wetherill, 1980; Chambers, 2004). One of the most important impact events is the formation of the Earth-Moon system, where a giant impact is estimated to have melted the Earth anywhere from $\sim$30% to 100% and created a protolunar disk (Tonks & Melosh, 1993; Canup & Asphaug, 2001; Canup, 2012; Ćuk & Stewart, 2012; Nakajima & Stevenson, 2015) from which the Moon formed. With these energetic impacts being more enhanced in the

late stages of planet formation (Agnor et al., 1999), the geochemistry of the mantle and core could be altered should materials from impactor be incorporated into the protoplanet. However, the amount of incorporated material which subsequently undergoes chemical equilibriation as it sinks into the Earth depends on parameters such as the impactor's size, velocity, and impact angle (Dahl & Stevenson, 2010; Deguen et al., 2014; Landeau et al., 2021).

Core Formation

Another heat source associated with magma oceans is from the formation of the core. During the accretionary phase, metals would have physically separated from silicates in a process known as metal-silicate differentiation. Although liquid metal can separate from silicates that are either in the liquid or crystalline phase (Melosh, 1990a), it is quite likely that the former occurred in the presence of a magma ocean. As mentioned in the previous section, while it is possible for kinetic energy from accretionary impacts to create magma oceans on Earth, the heat released can also go into melting the impactor's body which undergoes mixing with the molten surface of the Earth (Tonks & Melosh, 1993). Any metallic iron that was part of the impactor would have descended through the magma ocean and create metal ponds at the boundary between the magma ocean and crystalline silicate (Rubie et al., 2003; Wade & Wood, 2005) (fig 1.1). However, this is not a gravitationally stable configuration and the metal will descend further, past the crystalline silicate, towards the centre of the Earth. Regardless of the mechanism of metal transport from the shallower parts of the Earth to the core region, this process results in changes in the initial and final density distribution of the planet. In other words, metal-silicate differentiation releases gravitational potential energy which is being converted to heat that increases the temperature of the metal and surrounding mantle. Estimates of the temperature increase due to core formation from an undifferentiated Earth is on the order of $\sim$1000 K (Gubbins et al., 1979; Solomon, 1979; Sasaki & Nakazawa, 1986; Šrámek et al., 2012; Rubie, Nimmo, et al., 2015).

1.1.3 The Core-Mantle Boundary

The onset of gravity-driven segregation within the Earth during its formation gave rise to two distinct regions in the Earth's interior – the metallic core in the centre and the surrounding rocky mantle comprised largely of silicates and oxides. The depth of the core-mantle boundary (CMB) was first determined by Beno Gutenberg in 1913, and it was only until later that the outer core was demonstrated to be a fluid by Harold Jeffreys. Pressures and temperatures at the CMB are estimated to be around 136 GPa and $\sim$4000 K respectively, with the density of the outer core and bottom-most rocky mantle expected to be 9900 kg m^{-3} and 5500 kg m^{-3} respectively (Dziewonski & Anderson, 1981). In addition to the large density contrast, significant differences in transport properties such as dynamic viscosity, thermal conductivity and electrical conductivity are expected especially since one side of

the boundary is largely solid rock while the other side is a liquid metal. Hence, the dynamics that govern both regions of the Earth's interior are very different with the CMB being an important interface where heat, mechanical and chemical exchange occur.

The CMB is one of the most dynamically interesting regions to study in the Earth but multiple challenges arise because: (1) it is physically inaccessible, (2) extreme pressure and temperature conditions make it difficult to ascertain accurate material properties and their behaviour in labroratory experiments, and (3) data obtained from indirect sensing methods such as seismic waves, electromagnetic and gravity surveys have to be carefully deconvolved from structural complexities that exist in the crust and upper mantle. Despite these challenges, improvements in data collection, experimental methods and data analysis have managed to broaden our understanding of the CMB, especially so when different disciplines of Earth sciences come together to tackle problems using a multidisciplinary approach. Seismological studies of the CMB region tell us that the bottom of the lowermost mantle is home to a variety of unique features and interesting phenomena, with major features that have been interpreted at the CMB include: Large Low Shear-wave Velocity Provinces (LLSVPs), Ultralow Velocity Zones (ULVZs), and outer core stratification, among others. These features have been studied extensively as they are potentially important in facilitating chemical and heat exchange between the core and mantle, while also influencing the evolution of the planet and even life on the surface.

1.2 Interactions at the Core-Mantle Boundary

Chemical fingerprints of core-mantle interaction have long been sought. Signs of such a process might show up in ocean island basalt (OIB) lavas that are hypothesized to be generated by partial melting of hot upwelling rocky mantle plumes that rise up from the CMB (Morgan, 1971). A variety of past studies have reported on isotopic and elemental anomalies in connection with core-mantle interaction, such as high $^{186}Os/^{188}Os$ and $^{187}Os/^{188}Os$ (Walker, 2000; Brandon & Walker, 2005), low $^{182}W/^{184}W$ (Mundl-Petermeier et al., 2017; Mundl-Petermeier et al., 2019), reduced D/H (Hallis et al., 2015; Wu et al., 2018), elevated $^{3}He/^{4}He$ (Bouhifd et al., 2013), high $\delta^{56,57}Fe$ (Konter et al., 2016; McCoy-West et al., 2018; Soderman et al., 2021), and Fe/Mn (Humayun et al., 2004). Various mechanisms that may involve core-mantle exchange include expulsion/crystallisation of solids from the core (Kellogg & King, 1993; Manga & Jeanloz, 1996; Buffett et al., 2000; Badro et al., 2016; O'Rourke & Stevenson, 2016; Hirose et al., 2017; Helffrich et al., 2018), metal infiltration via capillary action (Poirier et al., 1998), poroviscoelastic entrainment (Petford et al., 2005), interaction with a basally molten mantle in the early Earth (Labrosse et al., 2007), pressure-driven infiltration of metal into pore spaces at CMB topographic lows (Kanda & Stevenson, 2006), ingestion of $\sim \mu$m-scale metal blebs via morphological instabilities (Otsuka & Karato, 2012; Yoshino, 2019), and thermodiffusion (Lesher et al., 2020). However, there is little consensus around the robustness of proposed CMB tracers, nor the mechanisms that could be involved.

The most promising approach at present is to combine constraints from a variety of disciplines in order to arrive at a coherent framework that relates potential tracers of core-mantle interactions with candidate processes operating at the CMB, their dependence upon material properties at CMB pressure and temperature (P-T), and testing against other varieties of observations from geodesy, seismology, and geomagnetism. The inherently interdisciplinary nature of the problem is apparent when one considers that it is not possible to interpret geochemical data without reference to the generating processes, while the processes themselves must also be constrained by the geochemical data. The candidate mechanisms that may be responsible for core-mantle interactions are not necessarily mutually exclusive. In fact, all of the potential mechanisms could operate in parallel with one another, producing diverse signatures as a consequence. Combined multiple mechanisms could also have a non-linear outcome that is different from the sum of their effects considered in isolation. Such emergent behaviors are a hallmark of the myriad collaborative natural processes that shape our planet.

This section aims to establish a broader framework for understanding the connection between potential processes operating at the CMB, proposed geochemical tracers of core-mantle interaction, and their dependence on physical properties at CMB P-T. An overview of core-mantle interactions and previous studies are presented first, followed by a survey of potential CMB interaction mechanisms, and consider their connections to physical properties.

1.2.1 Motivation

Metal-silicate core-mantle boundaries are thought to be one of the oldest persistent features in solar system bodies, having formed inside planetary embryos and planetesimals within the first $\sim$1 Myr (Baker et al., 2005). Thus, core-mantle boundaries are formed during the early accretion of the Earth, and the segregation of elements and isotopes into metallic and silicate domains is an ancient process that may have been ongoing before the clearing of the nebular cloud. A combination of heat and a large density difference facilitated separation even inside smaller bodies with low gravity. The last major event that was energetic enough to have a significant influence on the core-mantle scale system is thought to be the Moon-forming event $\sim$4.4–4.5 Gyr ago (Nakajima & Stevenson, 2015; Landeau et al., 2016). Thus, the state of the core and its relation to the mantle was largely established during Earth's accretion. Post-accretion, the metal-silicate CMB is the most stable interface inside a terrestrial planet owing to the large density difference. The dissipation of gravitational energy as heavy metals sank to the center of planetesimals, embryos, and accreted proto-planets was more than sufficient to melt the entire body (Stevenson, 1981; Rubie, 2007), and is irreversible in the absence of new energy sources that are capable of paying the substantial cost to lift metals back up into the mantle. Furthermore, the persistently molten state of the outer core, maintained by the heat insulating effects of the surrounding mantle, endows core metals with a low viscosity that raises serious difficulties for mechanical coupling and upward entrainment of fluid into the mantle (Poirier & le Mouël, 1992).

It is therefore natural to suspect that primordial isotopic characteristics observed in OIBs – particularly those possibly dating to the period prior to the formation of the Moon – could be sourced in the CMB region, even if the mechanisms involved are poorly known. The core itself may be an ideal reservoir for preserving such signatures over billions of years, even if the overall concentration of species involved is only present in trace amounts. Given its ancient lineage, its relatively low abundance of radioactive elements that would otherwise pollute the core with daughter products, and lack of confounding processes such as volcanic degassing and surface recycling, the core has long been considered a potential reservoir for sequestering primordial isotopic signatures of our planet (Touboul et al., 2014; Mundl-Petermeier et al., 2017; Mundl-Petermeier et al., 2019; Mundl-Petermeier et al., 2020).

The promise of the core for explaining some recent isotopic anomalies in OIBs has increased pressure on our understanding of the processes taking place at the CMB which might be capable of conveying these signatures. While some efforts have been made along these lines in the past, we still lack a comprehensive picture for how the core and mantle could be on speaking terms with one another.

1.2.2 Geochemical Observations

Five isotopic systems and one transition element ratio are considered here whose detection in OIBs might be considered promising candidates for core-mantle isotopic and chemical interactions: ^{186}Os/^{188}Os–^{187}Os/^{188}Os, ^{3}He/^{4}He, ^{2}H/^{1}H (or simply D/H), μ^{182}W, $\delta^{56,57}$Fe and the Fe/Mn ratio. Correlations between the abundances of some of these isotopic systems and those we expect to find in the core support the idea of some degree of entrainment and/or chemical interaction.

Osmium

Studies examining the ^{187}Re-^{187}Os and ^{190}Pt-^{186}Os systems in plume-derived magmas have long provoked the idea of core-mantle isotopic exchange and the intriguing possibility of observing fractionation patterns due to inner core solidification (Brandon et al., 2003; Brandon & Walker, 2005). Samples retrieved in proximity of the Hawaiian plume (Brandon et al., 1999), the Siberian plume (Walker et al., 1997), and on Gorgona Island (Brandon et al., 2003) display coupled enrichments of ^{186}Os/^{188}Os and ^{187}Os/^{188}Os. These correlated osmium signatures are believed to indicate the presence of material derived from the outer core as a result of chemical interaction with the lowermost mantle. ^{187}Os is produced from the β^- decay of ^{187}Re with a half-life of $\sim$41.6 Gyr, while ^{186}Os is obtained from the α decay of ^{190}Pt with a half-life of $\sim$489 Gyr. Measurements of partition coefficients in iron meteorites indicate that Re and Pt are more incompatible in hcp-iron relative to Os (Morgan et al., 1995; Walker et al., 2002; Cook et al., 2004), which leads to a gradual enrichment of ^{187}Os/^{188}Os and ^{186}Os/^{188}Os in the outer core fluid as the inner core crystallises. The abundances of Re, Pt and Os are thus sensitive to the inner core growth rate and age.

Due to limited experimental data regarding the partitioning of Re, Pt and Os between solid and liquid metal at CMB pressures, it has usually been assumed that their partitioning behaviour is similar to that of asteroidal cores (2004; Brandon & Walker, 2005). However, partition coefficients at higher pressures could be substantially different. Recent results from high pressure experiments at 22 GPa (Van Orman et al., 2008) indicate that the partition coefficients become smaller and more similar to one another at these pressure ranges. If this trend continues at higher pressures and temperatures of the core, more Os is likely to remain in liquid the outer core, leading to a $^{186}Os/^{188}Os$ ratio which will be too low to explain the observed isotopic anomalies. The uncertainties associated with the partition coefficients for Re, Pt, and Os at Earth's core pressures are, however, quite large. Further studies of the partitioning behaviour at high pressure and temperature conditions are thus required. Additional complexities due to the effect of light alloying components in the core (e.g., sulfur, silicon, oxygen, carbon, and potentially hydrogen) on the partitioning behaviour of the radioactive species in the core is also warrants further investigation.

While material carrying core isotopic fingerprints must travel a long distance before manifesting at Earth's surface, it is generally thought that it is not be impacted by solid-liquid fractionation processes in the mantle during ascent. However, some suggest that it is possible for the outer core liquid to undergo further fractionation at the CMB (Humayun, 2011). This is thought to occur in compacting cumulate piles of Fe-rich nonmetallic precipitates on top of the core, where liquid metal is trapped and crystallised into solid metal grains while the residual metal liquid is drained back into the core. The crystallised metal grains are then subsequently entrained into mantle upwellings and be picked up on the surface. This process would require a strong thermal gradient across the CMB and take into account the timing of the formation of the inner core and its effects on the Os isotope ratios.

Although other processes like contamination of the magma source by oceanic crustal recycling has been suggested explain the anomalous signatures in Os (Lassiter & Hauri, 1998), the resulting enrichment would be insignificant (Puchtel et al., 2020) and the hybrid source (comprising mantle and crustal material) will need to have suprachondritic Re/Os and Pt/Os ratios (Puchtel et al., 2005).

If these signatures are derived from the core, then the growth rate and the age of the inner core play key roles in influencing these signatures. Previous studies (e.g. Brandon et al., 1999) have investigated different core thermal histories and found that the observed osmium abundances are best explained by an early onset (i.e., prior to 3.5 Ga ago) and gradual inner core crystallisation (Brandon et al., 2003), which would lead to increasing Pt/Os and Re/Os, and suprachondritic $^{187}Os/^{188}Os$ and $^{186}Os/^{188}Os$ abundances in the liquid outer core. While the partition coefficient for Pt was kept constant, Brandon et al. (2003) adapted the partition coefficients of Os and Re to fit the present $^{186}Os/^{188}Os$ ratio of the outer core ($^{186}Os/^{188}Os = 0.11987$), which is thought to lie at the intersection between the regression lines of OIB sample abundances.

Recent discoveries on a number of processes and material properties of Earth's core have

challenged the current knowledge on the age and the crystallisation rate of the inner core. Mineral physics experiments and ab initio simulations have argued that the core has a much greater thermal conductivity than previously thought (Pozzo et al., 2012; Gomi et al., 2013), and thus a younger inner core that grows faster in recent geological history. Due to the long the half-lives of ^{187}Re and ^{190}Pt, the concentrations of Os, Re, and Pt stay almost constant before inner core formation. However, the partition coefficients needed to fit the present core isotopic ratios might be substantially different than the ones obtained in past experimental studies (Walker, 2000; Van Orman et al., 2008).

Tungsten

Lithophile ^{182}Hf indirectly decays into moderately siderophile ^{182}W with a half-life of $\sim$9 Myr, separated by the short-lived intermediate isotope ^{182}Ta (Halliday, 2000). This geologically short half-life and the lithophile-siderophile duality of the isotope pair make the ^{182}Hf-^{182}W system attractive for core chronometry, as residual ^{182}W is interpreted to reflect the cessation of metal-silicate interaction at the end of core formation. However, as a result of increasing precision in trace element analyses, heterogeneous ^{182}W abundances have been reported across the spectrum of mantle-derived source material (Mundl-Petermeier et al., 2017; Mundl-Petermeier et al., 2019). Variations in ^{182}W are reported as μ^{182}W, which are deviations of ^{182}W/^{184}W of a given sample with respect to a laboratory W standard. Recently, Mundl-Petermeier et al. (2020) reported μ^{182}W as low as -25.6 (25.6 ppm lower than mantle standard as inferred by chondritic abundances due to the relative incompatibility variations between Hf and W; Kleine and Walker, 2017) in a large suite of OIBs including Samoa, Hawaii and the Galapagos. These samples are negatively correlated with measured ^{3}He/^{4}He abundances (see below) and suggest the existence of chemically distinct mantle reservoirs.

Altogether, the study found three distinct He-W trends and hypothesised to originate from at least three separate geochemical reservoirs – two of which are primordial and one similar to the depleted MORB mantle. The primordial reservoirs are characterised by little or almost completely undegassed components where ^{3}He/^{4}He is very high (~ 50 times higher than the present day atmosphere). However, the main difference between these two reservoirs are the μ^{182}W values, where one is suggested to have $\mu^{182}\text{W} \approx 0$ while another is assumed to be strongly negative. The former might reflect remnants of early crystallisation products of a basal magma ocean (BMO) that can exist as an isolated reservoir if it was formed after ^{182}Hf ceased to exist (> 60 Myr after formation of the solar system).

As for the latter, there are a few potential sources for a separate undegassed reservoir to possess strongly negative μ^{182}W values, with one possible source being the core. If the silicate Earth is on average $\mu^{182}\text{W} = 0$ and assuming that the bulk Earth has a chondritic μ^{182}W, a mass balance would indicate the core to have $\mu^{182}\text{W} = -220$ (Touboul et al., 2014). Since most mantle plumes originate from somewhere close to the CMB, the core can impart its negative μ^{182}W values directly to such plumes if there is significant core entrainment. However, a process that allows physical incorporation will strongly enrich the plumes in

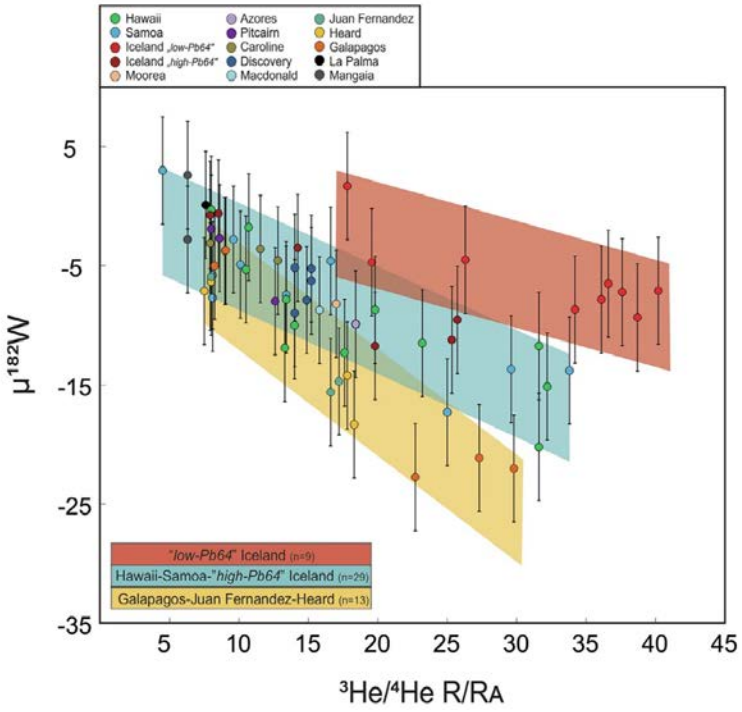

FIGURE 1.3: Plot of ^{3}He/^{4}He versus μ^{182}W showing three separate He-W trends reproduced from Mundl-Petermeier et al. (2020). R/R$_A$ is the measured ^{3}He/^{4}He normalized to the atmospheric ratio of 1.384×10^{-6} (Mabry et al., 2013).

highly siderophile elements (HSEs) which is not observed in the OIBs. Hence, a more likely source would be a reservoir where mantle material has chemically and isotopically equilibrated with the outer core. Mundl-Petermeier et al. (2020) suggest this material to be partially molten based on estimated diffusion rates of W at present day oxygen fugacity of the lower mantle. Nevertheless, if isotopic signatures of the core could be imparted to the mantle at the CMB, but without actually carrying a significant amount of metal up into the mantle, core-mantle interactions could represent an explanation for this observation.

Helium

While nearly all ^{3}He is primordial, ^{4}He is produced from the decay of ^{238}U, ^{235}U and ^{232}Th. Since the discovery of excess ^{3}He dissolved in Pacific deep water (Clarke et al., 1969), high ^{3}He/^{4}He ratios in OIBs have been well documented (e.g. Lupton and Craig, 1975; Kaneoka and Takaoka, 1978; Kurz et al., 1982), with some ^{3}He/^{4}He as high as 40 R/R$_A$ (R/R$_A$ is the measured ^{3}He/^{4}He normalised to the atmospheric ratio of 1.384×10^{-6}; Mabry et al., 2013), suggesting the existence of an undegassed mantle reservoir enriched in primordial ^{3}He (Allègre et al., 1983). If such distinct reservoirs exist, it would imply long term preservation of chemically heterogeneous domains that have been isolated from the MORB source reservoir over the Earth's geologic history. The possibility that these domains still exist today has spurred heated debates about the Earth's interior, specifically whether the mantle is distinctly layered (e.g. 1983; Kellogg and Wasserburg, 1990; Porcelli and Wasserburg, 1995;

Hofmann, 1997) and, as a consequence, if mantle convection is layered too (e.g. Galer and O'nions, 1985; Kellogg et al., 1999). On the other hand, geophysical evidence from seismic tomography has traditionally favored whole mantle processes based on the penetration of subducted slabs into the lower mantle and rising mantle plumes (e.g. Creager and Jordan, 1986; van der Hist et al., 1991; van der Meer et al., 2010).

Layered mantle models were of interest as they proposed that the mantle is divided into two distinct regions – the upper mantle that is mostly depleted and degassed due to crustal formation, and the lower mantle that is relatively undegassed containing primordial material such as ^{3}He (e.g. Allègre et al., 1983). To account for the observed ^{3}He/^{4}He ratio and other noble gas isotopes, a "steady state" upper mantle was suggested where the rare gas reservoir in the upper mantle is able to interact with that of the atmosphere and lower mantle such that rare gas concentrations in the upper mantle remained constant over time (Kellogg & Wasserburg, 1990; Porcelli & Wasserburg, 1995). These models were somewhat controversial initially as they do not seem to explain how such large primitive reservoirs can be preserved without extensive degassing during planetary accretion, core formation and large scale mantle convection since the latter provides significant mixing of material over geological time scales. However, recent geodynamical models suggest that large scale heterogeneities composed of bridgmanite with larger viscosities can resist mantle mixing for very long periods of time (Ballmer et al., 2017; Gülcher et al., 2020). Thus, they can be potential reservoirs for primordial chemical signatures.

An alternative way to account for the high ^{3}He concentrations in OIBs is to have the outer core be that reservoir which subsequently chemically equilibrates with the mantle. During the early stages of core formation, uranium and thorium are strongly partitioned into the mantle as they are highly lithophile (Wheeler et al., 2006; Bouhifd et al., 2013; Faure et al., 2020), and although ^{3}He has low solubility in the core (Bouhifd et al., 2013), it is not zero. Hence, it is possible that the early core began with a high He/U ratio and by extension, high ^{3}He/^{4}He ratio from the radioactive decay of U. If the core is able to equilibrate with some mantle material, it is entirely possible for a mantle plume to sample such sources to give basalts with high ^{3}He/^{4}He ratios.

Hydrogen

Most of the hydrogen present on Earth today is thought to be acquired as a result of accretion of chondritic material during planet formation in protoplanetary disks (Lécuyer et al., 1998; Alexander et al., 2012). The amount of hydrogen supplied from this process amounts to 5-25 Earth oceans of water (Wu et al., 2018). Since protoplanetary disks are thought to dissipate on timescales of a few million years ($\sim$3 Myr; Haisch Jr et al., 2001), gas giant planets would have already formed by then and retain a significant fraction of nebular gas. On the other hand, rocky planet formation in the inner solar system is still ongoing, but Mars-sized planetary embryos containing around 7-8 Earth's oceans of water may exist before the disk has completely disappeared (Raymond et al., 2006). The gravity of these bodies is not

high enough for them to attract much gas from the accretion disk; however, a small yet non-negligible amount of nebular hydrogen is expected to be incorporated within their primordial atmospheres (surface pressures of 1-10 bar for a 0.3-0.4 M_{Earth} planet; Stökl et al., 2016) and interiors, along with other gases such as helium and neon (Harper & Jacobsen, 1992; Pepin, 1992; Marty, 2012). If the mantles of these bodies are partially or fully molten due to energetic impacts and/or radioactive decay of short-lived isotopes, hydrogen gas is highly soluble in, and expected to penetrate into, the existing magma ocean (Hirschmann et al., 2012; Pahlevan et al., 2019).

The solar nebula could hence be the source of some of the hydrogen present in Earth's lower mantle (Sharp, 2017; Olson & Sharp, 2018; Wu et al., 2018). Besides the one present at Earth's surface, considerable amounts of hydrogen (and perhaps even most of it) are expected to be contained inside Earth's core, with fractions reaching to up to 0.1 wt.% (Wood et al., 2006; Zhang & Yin, 2012; McDonough, 2014), corresponding to around 10 oceans of water. The presence of hydrogen inside the core, along with other light elements such as Si, O, S, and C, has been suggested in the past as a way to account for the density deficit of the core, which does not correspond to the one of a pure iron-nickel alloy. As discussed below, mineral physics theoretical calculations and experiments seem to show an even larger affinity for metals at high pressure and temperature, such that the core may contain more than several dozen ocean equivalents of hydrogen (Li et al., 2020; Yuan & Steinle-Neumann, 2020; Tagawa et al., 2021).

The hydrogen content of the core should reflect partitioning into metals sinking to the Earth's center during metal-silicate differentiation (Wu et al., 2018). In this scenario, the light hydrogen isotope (^{1}H) will preferentially partition into the sinking metal to form iron hydrides, while the heavier one (^{2}H or deuterium) will remain enriched within the residual melt.

This leads to a high D/H ratio inside the mantle (D/H = 150e-6; Hallis et al., 2015; Wu et al., 2018), and a reduced one within, and in proximity of, the core (D/H = 130e-6; 2018). The recently observed low D/H ratio of Baffin Island basalts (D/H = 122e-6; Hallis et al., 2015) could thus be associated with an origin consistent with the core or the core-mantle boundary, where material exchange between core and mantle might have occurred. Plumes rising from the lower mantle to Earth's surface could thus sample material with hydrogen isotope ratios similar to the ones found in the core.

Iron Isotope Fractionation

Variations in a number of stable isotope fractionations have been detected across a wide suite of lavas (e.g. Richter et al., 2003; Teng et al., 2008; Schuessler et al., 2009; McCoy-West et al., 2018) and it is thought to illustrate the complex effects arising from the interplay between partial melting, fractional crystallisation of melts and subsequent heterogeneities of the source regions (e.g. Konter et al., 2016). One of these stable isotope ratios of interest

is $\delta^{56,57}$Fe, where

$$\delta^{56,57}\text{Fe} = \left[\frac{\left(^{56,57}\text{Fe}/^{54}\text{Fe}\right)_{\text{sample}}}{\left(^{56,57}\text{Fe}/^{54}\text{Fe}\right)_{\text{standard}}} - 1 \right] \times 1000 \tag{1.1}$$

Elevated $\delta^{56,57}$Fe have been found in OIBs originating from hotspots including Samoa, Hawaii, and Azores, with some samples in the Azores exceeding 0.25‰ (2016; Soderman et al., 2021). It has been suggested that processes resulting in the enrichment of heavier iron isotopes in residual melts include: olivine accumulation, fractional crystallisation, and geochemical heterogeneities arising from mantle mineralogy such that melting of peridotites and pyroxenites can potentially produce significant isotope fractionation (2021). However, melting models that consider these post-emplacement processes seem unable to reproduce the observed heavy δ^{57}Fe in melts, indicating that additional processes that affect the source δ^{57}Fe composition has to be considered as well. While it is possible for processes that occur at subduction zones and the lithosphere to impart heavy iron isotopes to the OIB melts (2021), it has been proposed that the high $\delta^{56,57}$Fe might have originated from the core where isotopic fractionation occurs at the lower mantle (close to the CMB) due to thermodiffusion (or Soret diffusion) (Lesher et al., 2020). In the presence of a steep thermal gradient (such as the thermal boundary layer), it is believed that iron isotopes in the core fluid will undergo kinetic fractionantion, thereby creating a region of heavy $\delta^{56,57}$Fe liquid metal closest to the mantle side that is subsequently incorporated into upwelling plumes via entrainment. As the plume rises, the core fluid will freeze and preserve the isotopic anomaly while being surrounded by ambient mantle, and the magma that erupts on the surface will contain heavy $\delta^{56,57}$Fe. If this process of obtaining heavy $\delta^{56,57}$Fe in OIBs via the incorporation of core liquids is true, there should be correlated enhancements in HSEs, μ^{182}W, ratios of ^{3}He/^{4}He and Fe/Mn. However, as we have seen in the previous section on tungsten there is no observed enrichment of HSEs in numerous OIBs. In addition, there has also been no correlations observed between $\delta^{56,57}$Fe with μ^{182}W, and ratios of ^{3}He/^{4}He and Fe/Mn (McCoy-West et al., 2018; Soderman et al., 2021). Even if the heavy $\delta^{56,57}$Fe is inherited from the core, calculations have shown that this value is still much smaller than the heaviest observed value. Overall, these evidence suggest that the link between observed heavy $\delta^{56,57}$Fe and plume-entrained core liquids is rather weak, and instead is more likely to have originated from other processes happening in the mantle and possibly the lithosphere.

Fe/Mn ratio

A large proportion of Fe in the mantle exists as Fe^{2+} (e.g. Canil et al., 1994), while all the Mn exist as Mn^{2+}. Due to their similar ionic radii and charge, both elements have similar partitioning behaviour between solids and liquids (Humayun et al., 2004). This results in an approximately constant Fe/Mn during magmatic processes such as partial melting and fractional crystallisation, as seen in measurements of peridotites (Fe/Mn $= 60 \pm 10$; McDonough and Sun, 1995) and terrestrial basalts (Fe/Mn $= 59 \pm 9$; Ruzicka et al., 2001).

However, measurements of Fe/Mn in OIBs associated with the Pacific and African superswells have yielded higher values (> 65) than MORBs (~ 54) and Icelandic picrites ($\sim 58 - 61$) (Humayun et al., 2004; Qin & Humayun, 2008), indicating that there are significant chemical variations in the mantle source regions. Although the Icelandic OIBs exhibit higher Fe/Mn than MORBs as well, they show different trends of μ^{182}W vs. ^{3}He/^{4}He and ^{206}Pb/^{204}Pb from Haiwaiian and Samoan OIBs (fig 1.3) (Mundl-Petermeier et al., 2019). Furthermore, it was found that radiogenic ^{186}Os/^{188}Os is absent in the Icelandic lavas (Brandon et al., 2007), indicating that the Iceland plume might be sampling a different mantle reservoir compared to the other OIBs (e.g. Wolfe et al., 1997; Montelli et al., 2004; Mundl-Petermeier et al., 2020).

Estimates of element concentrations of the Earth's core based on data for the Earth's mantle and carbonaceous chondrites have shown Fe/Mn ratios to be on the order of $\sim 10^2$ (McDonough & Sun, 1995; McDonough, 2014), much higher than any of the OIBs. Assuming that oxygen in the form of FeO is the most abundant light element in the core, the exchange of FeO at the CMB can impart high Fe/Mn ratios to melts in the lower mantle which are then sampled by the hotspot volcanoes. The rate of FeO transfer would depend on the solubility of O in Fe metal at CMB pressure and temperature (e.g. Ohtani and Ringwood, 1984; Rubie et al., 2004; Takafuji et al., 2005). Hence, if the core is under-saturated in O, core-mantle interaction could remove FeO from mantle material preferentially to Mn and hence decrease Fe/Mn. The opposite would be true if the core becomes over-saturated in O.

Additionally, since the melt-solid partitioning behaviour of transition metals (Fe, Mn, Ni etc.) can be affected by electronic spin transitions at high pressures (e.g. Tsuchiya et al., 2006; Komabayashi et al., 2010; Piet et al., 2016), there is also a possibility that deep mantle fractionation via basal magma ocean crystallisation or other melting/freezing processes might create pockets of Fe-rich primoridal reservoirs at the CMB where distinct signatures are imparted to the source (Lee et al., 2007).

Other Noble Gases

Apart from He, other noble gas systems have been used to differentiate MORB and plume sources, as well as characterising individual plume sources (e.g. Honda et al., 1993; Raquin and Moreira, 2009; Mukhopadhyay, 2012; Vogt et al., 2021). Ratios between primordial Ne isotopes (^{20}Ne/^{22}Ne) can reveal the accretion process of volatiles in the early Earth as the main sources of volatiles are: (1) the nebular gas, (2) irradiated dust particles by the solar wind, and (3) CI chondrites. Ne isotopes in plume-derived magmas from places such as Iceland and the Galapagos show high ^{20}Ne/^{22}Ne ratios that lie between the solar nebular and irradiated material by the solar wind (Sarda et al., 2000; Yokochi & Marty, 2004; Mukhopadhyay, 2012; Péron et al., 2016), indicating that the remnants of the Earth's early accretion are probably present in the deep mantle. Recent experiments using laser heated diamond anvil cells (LHDAC) have shown that the partition coefficient of Ne between Fe-rich alloys and silicate melts has very little pressure dependence with increasing pressure

(Bouhifd et al., 2020). Since the partition behaviour is similar to He, the core might also be a reservoir of primordial Ne based on estimated concentrations of the primordial mantle.

Some OIBs also exhibit less radiogenic Ar in the form of low ^{40}Ar/^{36}Ar ratios, where ^{40}Ar is a decay product of ^{40}K. Although this further implies a source that underwent little degassing and processing, calculations show that the core is unable to support a large ^{36}Ar flux to the mantle based on estimated upper and lower bounds of primordial volatiles that have been degassed, in addition to results from high pressure experiments on liquid iron-silicate melt partitioning (Xiong et al., 2021).

^{129}Xe is produced by the radioactive decay of iodine-129 (^{129}I) with a half-life of 15.7 Myr that is presently extinct, while ^{130}Xe is primordial. LHDAC experiments have shown that at high temperatures and pressures (> 2000 K and > 20 GPa), I is siderophile (Armytage et al., 2013; Jackson et al., 2018) and hence can sequester in the core if core formation occurred while ^{129}I was still extant (before 4.45 Ga). Calculations have also suggested that up to 85% of the Earth's iodine could have been sequestered in the core (McDonough, 2014). It is then natural to expect that the core has a higher ^{129}Xe/^{130}Xe ratio than the ambient mantle and, by extension, any mantle reservoir that has chemically and isotopically equilibrated with the core. This is assuming that both the reservoir and ambient mantle are undegassed or have undergone the same amount of degassing. Although Xe isotope measurements from hotspots such as Iceland, Hawaii, Réunion, and Samoa have shown high ^{129}Xe/^{130}Xe ratios relative to the atmosphere, they appear to be lower than MORB values (e.g. Poreda and Farley, 1992; Trieloff et al., 2000; Trieloff et al., 2002; Hopp and Trieloff, 2005; Mukhopadhyay, 2012; Pető et al., 2013). The difference in ratios has been interpreted as different I/Xe ratios between MORB sources and plume sources for OIBs.

1.2.3 Mineral Physics Constraints

A large number of mineral physics experiments have been conducted to characterise the partitioning behaviour of different trace elements between silicate and metallic melts at high pressure and temperature conditions. This is usually represented by the partition coefficient D_X which is defined as the ratio of the concentration of some chemical species X in the metal to the concentration of the same chemical species in the silicate.

Noble Gases

One of the earliest experiments looking into noble gas partitioning was performed by Matsuda et al. (1993). Results from this study indicated that for all noble gases, partitioning into the metallic component becomes less favorable with increasing pressure. They reasoned that the solubility of a noble gas depends on the surface tension of the melt such that larger surface tension reduces solubility. Thus, the preferential partitioning of noble gasses into the silicate melt at increasing pressures could be due to the surface tension of iron melts increasing faster than that of silicate melts. This led them to conclude that the Earth's core could only hold negligible amounts of noble gases.

However, LHDAC experiments conducted at higher pressures and temperatures with samples loaded under helium-saturated conditions found that although the partition coefficient of He (D_{He}) is still much less than unity, rather than decreasing with increasing pressure, D_{He} stays relatively constant for pressures $\geq$6 GPa (Jephcoat et al., 2008; Bouhifd et al., 2013) with D_{He} ranging from 4.7×10^{-3} to 1.7×10^{-2}. In addition, the same study found that the composition of the metal has little effect on the partitioning behaviour of He as well. Molecular dynamic simulations at $\sim$40 GPa and 3200 K support similar values of D_{He} (Zhang & Yin, 2012), and the combination of this result with experiments seem to support the idea that large amounts of primordial helium could have been incorporated into the Earth's early core (Bouhifd et al., 2013). The same partitioning behaviour has been observed in neon as well (Bouhifd et al., 2020) but with slightly larger coefficient values than that of helium ($10^{-2} < D_{\text{Ne}} < 10^{-1}$). This implies that neon might actually partition more favourably into the core than helium, resulting in lower ^{3}He/^{22}Ne values in the core than the mantle.

Similar partitioning experiments conducted with iodine as the trace element of interest has shown that iodine is highly siderophile, with D_I ranging from just below 1 to as much as $\sim$5 (Jephcoat et al., 2008; Armytage et al., 2013). These studies have shown that although D_{I} does not seem to depend very much on pressure, the partition coefficient is actually quite sensitive to the composition of the metallic component. The same experiments have shown that if iron is alloyed with nickel and some amounts of sulfur and silicon, the siderophile behaviour of I is enhanced and partitions more into the iron alloy than pure iron (Jephcoat et al., 2008; Armytage et al., 2013). This observation might be explained by the chalcophile behaviour of iodine (e.g. Goles and Anders, 1962; Fuge and Johnson, 1984). Depending on the estimate amounts of iodine is present in the bulk silicate Earth, the amount of radiogenic ^{129}I that goes into the core during the Earth's early core formation can result in $\sim 10 - 1000$ times more radiogenic Xe in the present day core after going through radioactive decay (Armytage et al., 2013). Additional experiments have shown that it is highly unlikely for Xe to form an alloy with iron at CMB pressures (e.g. Caldwell et al., 1997; Nishio-Hamane et al., 2010) despite evidence of Xe becoming more metallic at higher pressures (e.g. Jephcoat et al., 1987; Eremets et al., 2000). Hence, any Xe that has formed in the core after core formation could have been easily lost to reactions at the CMB (Armytage et al., 2013).

Hydrogen

Unlike noble gases that are believed to reside as trace amounts in the core, hydrogen is hypothesized to be one of the major core light elements that can actually contribute to the observed density deficit and anomalies in seismic wave speeds of the core (e.g. Umemoto and Hirose, 2015; Tagawa et al., 2021). As such, there has been increasing interest in investigating the partitioning behaviour of H between metal-silicate and stability of iron hydrides at core-forming conditions. However, experimental results (e.g. Okuchi, 1997; Shibazaki et al., 2009; Iizuka-Oku et al., 2017; Clesi et al., 2018; Malavergne et al., 2019; Tagawa et al., 2021) and theoretical calculations (e.g. Zhang and Yin, 2012; Li et al., 2020; Yuan and Steinle-Neumann, 2020) of hydrogen partitioning have been rather controversial.

Some experiments have shown that H seems to be more lithophile ($D_H < 1$) during core segregation, suggesting that the core holds < 1 wt % of H and that the magma ocean could store significant amounts of water relative to the core (Clesi et al., 2018; Malavergne et al., 2019). The low concentrations in the metallic components reported in these experiments, however, could be due because the experiments were conducted in carbon-saturated environments hence reducing the ability of H to be incorporated an already C-enriched metal. Moreover, it is possible that hydrogen might have escaped from the samples during decompression before measurements were taken as iron hydrides can decompose into Fe and molecular H_2 (Fukai & Suzuki, 1986; Iizuka-Oku et al., 2017).

To prevent hydrogen escape and ensure that accurate hydrogen concentrations in metal alloys are obtained, recent experiments conducted at much higher temperature and pressure conditions (up to 4650 K and 60 GPa) were able to perform in-situ measurements of hydrogen concentration (Tagawa et al., 2021). Results from this study found $D_H \geq 29$ and that hydrogen is actually strongly siderophile at core forming conditions, disagreeing with the findings of previous experiments. The strongly siderophile nature also agrees with theoretical calculations (Li et al., 2020; Yuan & Steinle-Neumann, 2020) and that the core might actually contain 0.3–0.6 wt % of H (Hirose et al., 2021; Tagawa et al., 2021), approximately the amount of hydrogen in 37–73 ocean mass of water (2021). This amount of hydrogen in the outer core is also shown to be able to account for the seismically observed density deficit and excess sound velocity of the outer core by 30%–60% (Umemoto & Hirose, 2015; 2020).

1.3 Physical Mechanisms of Core-Mantle Exchange

In this section, various mechanisms of core-mantle exchange that could accommodate mass transfer, chemical reactions, and/or isotopic exchange are considered (fig. 1.4). As mentioned above, an important requirement is that the isotopic flavor of the core be imparted to silicates, but the conveyance of this material cannot permit carriage of a significant volume of metal. A summary of the key points of each core-mantle interaction mechanism is shown in Table 1.1.

1.3.1 Transfer Process from the Core to the Surface

For each mechanism, the general transfer process from the initial source of the heterogeneity to the final basalt product as well as the events that occur along the way that can influence the final outcome of the measurement in the lab is illustrated in figure 1.5. Prior to the interaction between the metal and silicate, the origins of the chemical and isotopic heterogeneities for each mechanism is largely similar and have been described in the preceding section. The main parameter controlling the initial concentrations of the chemical species of interest in the core is the metal-silicate partition coefficients and the degree of isotope fractionation for each element at P-T conditions during the Earth's accretion and differentiation phases. Depending on the interaction mechanism that is taking place at the

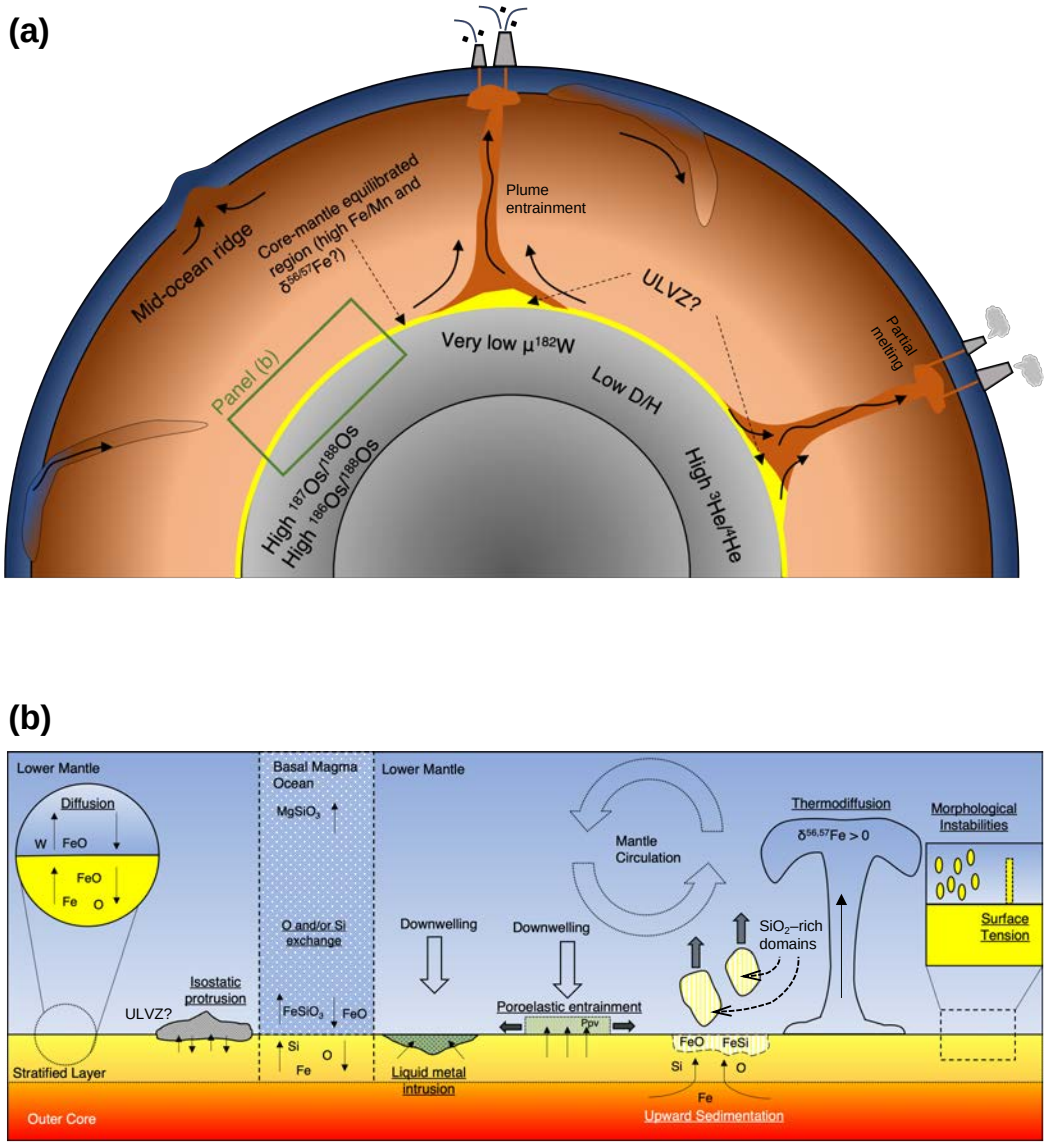

FIGURE 1.4: (a) Cartoon of the cross section of the Earth depicting how mantle plumes can incorporate material at the CMB and carry unique chemical signatures from the core to the surface. This material might be a result of chemical and isotopic equilibration between the liquid outer core and silicate mantle and the physical mechanisms for this equilibration is shown in panel (b). (b) A cartoon showing core-mantle exchange mechanisms that have been currently proposed in literature. Underlined text refer to the physical mechanisms that are described in the text. Ppv: Post-perovskite.

CMB, the relative mass of silicate and core material interacting with each other will be different, but the concentration of the chemical species at the end of the interaction will be largely determined by the metal-silicate partition coefficient at CMB P-T conditions. Subsequently, the processes that can occur post-reaction and prior to plume entrainment will depend on the interaction mechanism since additional effects on the concentration of heterogeneity in the reacted rock can occur.

Regardless of the interaction mechanism however, once the reacted rock begins to accumulate as a chemically distinct layer on the mantle side of the CMB, the entrainment efficiency of a thermal plume will dictate how much of the reacted rock from the layer travels up to shallower depths of the mantle via a thinner chemical plume. Thermal plumes originating from the CMB are formed from the upwelling of the thermal boundary layer which creates a cusp in the chemical boundary layer. This is from which the chemically distinct material is entrained into and transported upwards within the plume (Sleep, 1988). The rate of entrainment as well as the thickness of the chemical plume has been shown to depend on factors such as convection intensity, the geometry of the interface between the layers, the viscosity ratio, and the buoyancy ratio B (Davaille & Limare, 2015). B is defined as the ratio of chemical density contrast to thermal density contrast as follows:

$$B = \frac{\Delta\rho_C}{\Delta\rho_T} \tag{1.2}$$

where $\Delta\rho_C$ is the density contrast due to composition and $\Delta\rho_T$ is the density contrast due to temperature. Several studies from experiments and numerical models have reported scaling laws regarding the entrainment rate and thickness of the chemical plume in relation to parameters such as B and the viscosity ratio between the two layers (e.g Sleep, 1988; Davaille et al., 2002; Zhong and Hager, 2003; Jellinek and Manga, 2004). Although there have been differences between some scaling equations (2004), high resolution 2D numerical models from Zhong and Hager (2003) have shown that the entrainment rate Q is largely controlled by B and the radius of the thermal plume r_T as such

$$Q \sim B^{-2.48} r_T^{3.80} \tag{1.3}$$

This equation shows that the entrainment efficiency increases with smaller buoyancy ratio and a wider thermal plume, and is also independent of the thickness of the chemical layer. The thickness of the compositional plume was also found to be proportional to B^{-2} (Sleep, 1988; Davaille, 1999b).

As the plume carrying the chemically entrained material rises to the shallow mantle, the reduction in pressure will result in partial melting of the rock. Minerals such as garnet and clinopyroxene have lower melting temperatures than olivine at shallower depths, enabling major and trace elements to undergo further partitioning as the melts segregate from the bulk rock. For a given concentration of a trace element of interest C_0 in the bulk system, the

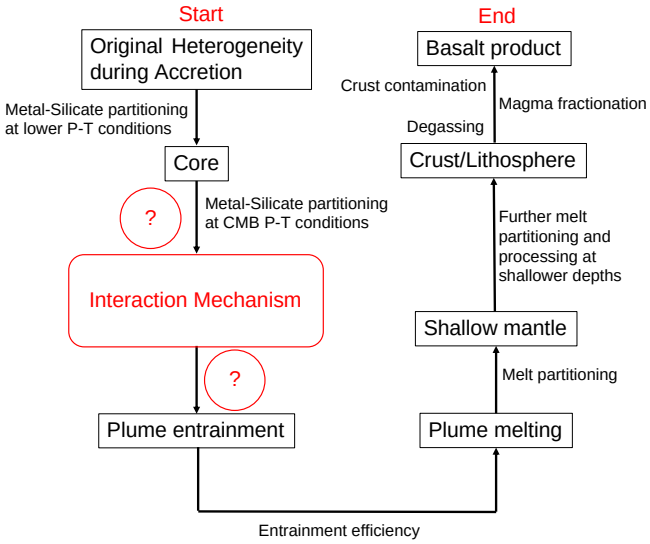

FIGURE 1.5: A flowchart describing the general process of transferring the original heterogeneity from the beginning of Earth's accretion to the final basalt product that appears on the surface of the Earth and the various events occurring in between that can affect the final measurement. Since the origins of the heterogeneities and the process of transferring them via plume entrainment onwards to the surface is largely the same for all interaction mechanisms, the main factor that can affect the final outcome is the interaction mechanism and the processes that occur before and after the interaction. These are marked in red.

equilibrium concentration in the melt C_m is given by

$$C_m = \frac{C_0}{F + d(1 - F)} \tag{1.4}$$

where F is the melt fraction and d is the partition coefficient (Shaw, 1970). If $d \gg 1$, this means that the element is compatible and stays in the solid, but if $d \ll 1$, the element is very incompatible and prefers to enter the melt. Since most OIBs are enriched in incompatible trace elements, this means: (1) $d \ll 1$ for these elements, and (2) they are generally produced by lower degrees of partial melting than MORBs.

Since the segregated melts are more buoyant, they will ascend further into the lithosphere and crust where they can erupt on the surface through volcanism or be stalled at depth through plutonism. However, before these hotspot volcanic rocks can reach the surface and be sampled in the lab, there are additional processes that can still act on the magma-derived rock and further affect its final composition. Such processes include: post-emplacement alteration, magmatic degassing, crystal-liquid fractionation, and crustal and lithospheric mantle contamination (Day, 2013).

Since OIBs usually erupt at locations far away from plate boundaries and continents, they are assumed to undergo relatively minimal contamination by the lithosphere. However, previous studies have shown this is not the case (e.g. Reisberg et al., 1993; Lassiter and Hauri, 1998; Gaffney et al., 2005) especially since Os isotopes can be sensitive to crustal contamination. The lithosphere tends to have a higher concentration of Os relative to the

volcanic rocks and as the concentration of Os decreases in the basalt, the high unradiogenic $^{187}Os/^{188}Os$ can potentially come from incorporation of oceanic crusts with high Re/Os and $^{187}Os/^{188}Os$ (Reisberg et al., 1993). This is especially so if the magma has sufficient time and heat to melt the surrounding rocks as it is stalled in the lithosphere. Hence, it is important to remove any crustal components from the OIB to obtain a more realistic value of the primary chemical composition.

While volatile elements such as noble gases are prone to magmatic degassing leading to volatile loss and reduced concentrations in the erupted basalt (e.g. Gonnermann and Mukhopadhyay, 2007), some of the HSEs can actually exhibit volatile behaviour as well. Studies have found Re compounds (e.g. Hinkley et al., 1999) and Os enriched sulphate-dominated condensates at volcanic vents (Crocket, 2000; Yudovskaya et al., 2008), but the extent of osmium isotope fractionation during degassing is relatively unclear. If there is significant fractionation effects, the Os isotope ratios obtained from laboratory measurements might lead to different interpretations of the HSE content of the core and hence, the degree of reaction between the core and mantle.

The erupted OIBs exhibit a wide range of compositions due to fractional crystallisation processes that occur prior to eruption. Apart from decompression melting that accompanies the magma as it rises to shallower depths, cooling of the magma as it stalls in the lithosphere can create further fractionation of isotopes and elements as it crystallises. The crystal-liquid fractionation in magmas usually involves the removal of different mineral phases at different depths and temperatures (Day et al., 2010), and the compatibility of different trace elements and their isotopes with the different mineral phases can potentially affect the chemical signatures inherited from the CMB. This is especially so when the abundances of some of these elements are quite low (Day, 2013). Studies have also shown that depending on the sulfur content of the melt, magmatic sulphides are generally rich in Os relative to coexisting silicate phases (e.g. Hart et al., 1996; Burton et al., 1999). Hence, the degree of crystallisation and sulfide content of the magma can provide uncertainties in some of the geocchemical and isotopic data.

Finally, after the magma crystallises, any post-emplacement alteration can potentially contaminate the volcanic rock. Such modifications can include natural processes such as hydrothermal alteration and metamorphism, to anthropogenic effects such as contamination from saw blades during sample preparation in the lab. To reduce the alterations that occur naturally, it is ideal to obtain 'fresh' samples that have erupted recently as they have the least exposure to the natural processes that can leach some of the metals or degassing of certain volatiles, thereby changing the chemical abundance in the rock. It is also worth mentioning that even after considering all these process that can affect the inherited core signatures after interaction at the CMB to eruption of the basalt product at the surface, uncertainties in the final result can also arise during measurements in the lab since there will always be uncertainties associated with the analytical measurements.

1.3.2 Diffusion Across a Sharp CMB

The simplest case of interaction between a liquid outer core and a solid crystalline mantle is the case where the CMB is a sharp interface. Although it initially appears simple, this basic case introduces a range complexities that are also relevant to all other mechanisms discussed further below, particularly the potential role of stable stratification in the shallow core and/or deepest mantle.

Stratification Atop the Core

Thermodynamic models have shown that for an expected mantle composition of Fe/(Fe + Mg) $= 0.2$ and assuming O is the sole light element in core, the liquid core can hold as much as 15 wt % of O at CMB conditions (Frost et al., 2010). Since this value is much higher than current estimated light element abundances (Badro et al., 2015), the chemical disequilibrium between the core and mantle sets the stage for interactions at the CMB. One of the ways in which this interaction has been expected to manifest is through a stable stratification on top of the core below the CMB. Buffett and Seagle (2010) modeled the evolution of a stratified layer at the top of the core where excess oxygen from the mantle (in the form of FeO) diffuses along the compositional gradient while taking into account inner core growth. In their model, the growth of the stratified layer is determined by the difference between the rate of change of concentration in the layer and well-mixed region, as well as the concentration gradient at the boundary between the two regions. The evolution of concentration in the stratified layer is a competition between two diffusive fluxes: barodiffusive and compositional, where the former depends on pressure gradients and the latter depends on concentration gradients. It can be expected that shortly after core-mantle segregation where temperatures are much higher, the initial compositional gradient at the CMB is much steeper, thereby driving a large oxygen flux into the topmost layer in the outer core. However, with secular cooling of the core and thickening of the stratified layer overtime, the compositional component of the diffusive flux weakens over time due to the decreasing gradient, whereas the barodiffusive component is expected to weaken only slightly. The combined effects results in a decrease in the oxygen flux to the core over billions of years with the thickness of the stratified layer predicted to be between $60 - 70$ km at present.

Although there have been some arguments against the existence of a stratified layer (e.g. Alexandrakis and Eaton, 2010; Irving et al., 2018), evidence from geomagnetic (Whaler, 1980; Braginsky, 1993; Buffett, 2014; Buffett et al., 2016) and seismic observations (Lay & Young, 1990; Souriau & Poupinet, 1991; Tanaka, 2007) have generally supported its presence. It has been known that if stable stratification at the top of the Earth's core exists, radial motion close to the CMB is suppressed. However, it is still possible for weak radial motion to exist due to MAC waves (Braginsky, 1993) arsing from the interplay between magnetic, Archimedes and Coriolis forces, and the period which these waves propagate depend largely on the Brunt-Väisälä frequency and thickness of the layer. Observations of magnetic field fluctuations were found to have dominant periods of ~ 60 years (Roberts et al., 2007; Jackson & Mound, 2010) and numerical calculations have shown that these waves can not

only provide a good description of these fluctuations (Buffett, 2014), they can also account for fluctuations in the dipole field (Yokoyama & Yukutake, 1991) and zonal flows at the top of the core (Jackson, 1997) inferred from secular variations in the geomagnetic field (Bloxham & Jackson, 1992). Moreover, numerical studies have found that the stably stratified layer can also account for observed changes in the length-of-day via a hybrid mechanism for momentum transport between the core and mantle (Glane & Buffett, 2018).

Even though there has been some agreements between geomagnetic and geodetic data with numerical models of the stratified layer, the origins of the layer is still a mystery. With different mechanisms of producing this layer proposed over the years (e.g. Fearn and Loper, 1981; Braginsky, 1993; Gubbins and Davies, 2013), some have suggested that its existence dates back to the early formation of the Earth (Landeau et al., 2016). Given that the Earth's magnetic field has existed for at least 3.45 billion years (Tarduno et al., 2010) and if the layer is primordial to begin with, vigorous convective motions in the outer core could potentially erode it overtime. To determine how much erosion could have potentially occurred, Bouffard et al. (2020) derived a scaling law that relates the erosion rate to the local Richardson number $E \propto Ri^{-1.7}$, where E is the erosion rate and Ri is a nondimensionless number measuring the buoyancy associated with a density jump across the interface of the layer versus the flow strength respectively, and found that stronger convection results in faster erosion rates. Based on estimates of present day convective power of the core (1-3 TW; Christensen and Aubert, 2006; Davies et al., 2015; Labrosse, 2015) and density anomaly of the stratified layer (0.01%-3%; Landeau et al., 2016; Jacobson et al., 2017), they calculated an erosion of less than 100 m over 4.5 Ga and suggested that a primordial stratified layer can still exist today.

Diffusion on the Mantle Side

The previous section discusses molecular diffusion on the core side assuming the mantle region adjacent to the CMB has the same concentration as the bulk mantle. This implies that there are no concentration gradients in the mantle while oxygen is fluxing into the core. However, it is not possible for chemical gradients to disappear instantaneously as lattice diffusion and grain boundary diffusion timescales in silicates are significant. Therefore, diffusion processes in the mantle are just as important and have to be considered as well since the diffusion process could have begun as far back as 4.5 Gyr when the mantle has fully crystallised from the magma ocean.

High pressure and temperature experiments using multi-anvil press were conducted by Yoshino et al. (2020) to determine the diffusivities of W and Re along the grain boundaries of post-spinel at shallow upper mantle conditions. They concluded that grain boundary diffusion for W in post-spinel is quite fast and under oxidized conditions, it becomes increasing lithophile and allows a large flux of W from the core to the mantle, assuming the core contains a large reservoir of W (specifically depleted with respect to ^{182}W). Due to the strong temperature dependence of diffusion observed in the experiments, the diffusion lengthscale of W is expected to increase towards the CMB such that within a span of 4.5 Gyr, W can

penetrate ~ 100s km into the lower mantle purely through grain boundary diffusion. While this lengthscale is incidentally the same order of magnitude as estimated heights of ULVZs (Yu & Garnero, 2018), the diffusion of W into subducted slabs is believed to be much quicker due to the smaller grain sizes and larger oxidation gradient. Although this mechanism can alter the chemical composition of the ULVZs and hence its seismic signature, it is not the only factor that can contribute to the seismically slow signature of the ULVZs. For instance, a dense and seismically slow domain can also be attributed to an iron-enriched silicate melt (Williams & Garnero, 1996) or iron-rich ferropericlase or bridgmanite (Mao et al., 2006; Wicks et al., 2010) at the CMB. With residence time of ~ 100 Myr, the diffusion lengthscale on the order of hundreds of metres can provide significant alteration of W isotope compositions in recycled crustal material provided that there is significant grain boundary volume. This mechanism can also in theory increase the concentration major or trace elements (including W) in the whole rock, but measurements of W, Ir and Os concentrations in OIB lavas have not found any distinct correlations with μ^{182}W (Mundl-Petermeier et al., 2020), suggesting that this mechanism might not be effective in enriching the rock with additional trace elements that might come from the core.

1.3.3 Interaction with Basal Mantle Magma

Interactions between a liquid outer core and a partially or fully molten mantle are considered in this section. The main mechanism considered here is elemental exchange between a BMO and the top of the core during the early Earth. Equilibration between two large liquid bodies should be more efficient than interactions between a solid mantle and liquid core, and there would be no excess metal residue in the silicates because heavy metal droplets rapidly settle from the magma. Diffusive exchange occurs on each side of the interface up to a thickness of $\approx \sqrt{4D_{\mathrm{i}}\tau_{\mathrm{r}}}$ where τ_{r} is the residence time of fluid at the interface and D_{i} is the effective diffusivity of species i. In laminar flows the relevant value for D_{i} is thermal diffusion, whereas in turbulent flows the relevant value of D_{i} will be similar to the turbulent viscosity. If the compositionally distinct LLSVPs or thin ULVZs detected today represent the residue of a BMO, then they may carry some isotopic characteristics of the core. However, additional considerations have to be given to the chemical fractionantion that occur during the freezing of the magma ocean over billions of years. As the magma ocean begins to cool and crystallise, incompatible trace elements will preferentially partition into the residual melt according to the existing pressure and temperature conditions. These melt-rich regions that occur in the lower mantle would be enriched in certain radioactive trace elements, such as U and Th, and if these elements undergo α-decay, they can potentially increase the concentration of ^{4}He in these regions such that any ^{3}He/^{4}He signal inherited from the core will be suppressed and appear to have undergone degassing. Some of the OIB samples have shown ^{3}He/^{4}He close to MORB values (Mundl-Petermeier et al., 2017; Mundl-Petermeier et al., 2020) which could suggest contamination from the radioactive decay of such elements in the source region.

Oxygen Exchange with a Basal Magma Ocean

Different 1-dimensional time-dependent models of FeO exchange between the outer core's stratified layer and BMO were developed by Davies et al. (2020) to investigate how coupled FeO concentrations between the bulk mantle and top of the core are affected by magma ocean crystallisation, according to different partition coefficients and initial concentrations of Fe and O in the magma ocean. In cases where the magma ocean does not crystallise, the oxygen concentration and thickness of a stably stratified layer at the top of the core grows according to $\sqrt{t}$ where t is is the diffusive timescale. Although this scenario gives a layer thickness of 120-150 km by the end of 4 Ga, it is unlikely that the magma ocean has remained uncrystallised for so long.

When crystallisation of the magma ocean from the middle is considered, the concentration of FeO in the magma ocean changes with the rate of freezing and FeO flux across the CMB. The former results in FeO enrichment of the magma ocean, while the latter depletes it if the core is undersaturated in O. Although losing FeO into the core can slow down the cooling rate of the BMO by buffering the decrease of the liquidus, the overall effect of FeO loss is actually an increase in the solidification rate of the BMO such that the BMO completely freezes within 3 Gyrs of core formation. It is also important to note that if FeO gradually depletes from the BMO during its existence, the density of the magma can be reduced to the point where it is lower than that of the overlying mantle, thereby inducing overturns that further hastens the solidification of the BMO.

Many studies have considered oxygen to be one of the major light elements in the outer core (e.g. Jeanloz and Ahrens, 1980; Alfè et al., 2002; Rubie et al., 2004; Badro et al., 2015) and calculations from ab initio molecular dynamics have shown that oxygen strongly partitions into the liquid phase as the core crystallises (Alfè et al., 2002; Ozawa et al., 2008). Although calculations show that it might be possible for oxygen to be the sole light element (Badro et al., 2014), this is only true if the resultant changes in density and bulk sound velocity is compared with PREM (Dziewonski & Anderson, 1981). Instead, the velocities in the stratified layer have been found to be slower than PREM (e.g. Tanaka, 2007; Helffrich and Kaneshima, 2010; Kaneshima and Matsuzawa, 2015) which suggests that any addition of light elements in the outer core should create a buoyant layer that is seismically slower (Helffrich, 2012). Hence, even though oxygen is likely to be the major component of light elements in the core, it is highly probable that there is more than one light element (e.g. C, H, Si, S) (e.g. Stevenson, 1981; McDonough, 2014).

Oxygen and Silicon Exchange

There have been studies that look into the creation of the stratified layer by concurrent O enrichment and Si depletion relative to the vigorously convecting outer core (Hernlund & Geissman, 2016; Brodholt & Badro, 2017). One possible mechanism for this to happen is to have an Si-enriched outer core (Fischer et al., 2015; Rubie, Jacobson, et al., 2015) react with a pyrolitic lower mantle that is driven by chemical disequilibrium. However, this

mechanism can only work for relatively low CMB temperatures of ∼4000 K (Brodholt & Badro, 2017). Another possible mechanism is for the core to react with material that is FeO-enriched and SiO_2 poor at the CMB. This can occur through either the fractional crystallisation of a BMO (Labrosse et al., 2007) or accumulation of a Fe-rich component at the CMB (Dobson & Brodholt, 2005; Wicks et al., 2010; Muir & Brodholt, 2015a; 2015b). As the BMO begins to cool, the melt can become relatively depleted in SiO_2 due to the crystallisation of bridgmanite while simultaneously enriched in FeO due to melt fractionation. The chemical disequilibrium that is established between the residual melt and outer core will result in FeO being diffused into the top of the outer core while Si diffusing into the melt that is sitting on the CMB. The resultant exchange of chemical species across the CMB therefore creates a light and slow layer at the top of the core which would be able to satisfy seismic observations of the outer core (e.g. Lay and Young, 1990; Tanaka, 2007; Helffrich and Kaneshima, 2010). However, in order to produce thicknesses of ∼100 km, diffusion would require the reaction to happen with mantle melts (or partial melts) instead of a fully solid mantle since diffusion rates are very slow in solids (Ammann et al., 2010).

1.3.4 Liquid Metal Intrusion at Mantle Downwellings "Suction"

Intrusion of core fluid into mantle rock at the grain scale, and subsequent drainage of the metal back into the core provides another mechanism for imparting core isotopic ratios to the mantle, so long as return of the metal back to the core is efficient and leaves little residual metal in the rock. A mechanism for intrusion of iron into mantle rocks via decompaction and grain scale percolation has been considered by (Kanda & Stevenson, 2006). The driving force for metal intrusion is the excess pressure created by pushing the mantle down into a higher density fluid in the presence of gravity, and the intrusion of metal works by deforming individual grains to open porosity that facilitates grain-scale intrusion of liquid into the rock. The duration of this decompaction is much shorter than mantle convection time scales, and is expected to proceed up to a porosity at which the grains are only loosely aggregated and further grain-scale deformation to open porosity is no longer possible. The thickness of the intruded region is expected to be of the same order of magnitude as the dynamic topography induced by mantle convection, ∼1 km (Olson et al., 1987). The motivation of the study by Kanda and Stevenson (2006) was to explain a high electrical conductivity layer at the CMB that could couple Maxwell stresses from the radial magnetic field in the core and mantle such that angular momentum exchange is allowed to explain observed variations in the length of day based on observations from very long baseline interferometry (VLBI). The amplitude of Earth's nutation are out of phase with tidal forcings due to dissipative processes originating from oceans and mantle anelasticity, however theoretical calculations of these amplitudes have shown some discrepancies with estimates from VLBI (Herring et al., 1991). If this discrepancy was to be accounted for by an electrically conductive layer at the base of the mantle, calculations suggest that this layer can have a conductivity ranging from $\sim 5 \times 10^5 - 10^8$ S m^{-1} with a thickness of about 200 m (Buffett, 1992; Holme, 1998). However, mantle conductivity and magnetic energy cannot be uniquely resolved by VLBI observations, implying there exists trade-offs between these two parameters. Nevertheless,

this mechanism also works great for chemical reactions between the core liquid metal and silicate mantle, and occurs relatively recently in the context of geological timescales.

Constraints on Iron-Silicate Grain Boundary "Wetting"

The efficiency of liquid metal intrusion into a silicate matrix as well as the subsequent drainage via percolative flow is highly dependent on the permeability of the matrix. This is largely controlled by the dihedral angle θ between liquid metal and solid silicate which determines how well the silicate grain boundaries are "wetted" by the liquid metal. The dihedral angle is formed where a crystalline-crystalline interface intersects with a liquid and is mathematically defined as

$$\cos\frac{\theta}{2} = \frac{\gamma_{ss}}{2\gamma_{sl}} \tag{1.5}$$

where γ_{ss} and γ_{sl} are the solid-solid and the solid-liquid interfacial energies respectively. Theoretical calculations of simple grain boundary topologies have shown that melts can form an interconnected network of channels that favours fluid percolation regardless of melt fraction if $\theta < 60^\circ$. However, if θ is larger than 60°, melts will exist as isolated pockets at grain corners and be impermeable to percolative flow unless the melt fraction exceeds a certain threshold (von Bargen & Waff, 1986) (fig 1.6). Experiments to determine the percolation threshold of liquid iron alloy in silicates via electrical conductivity have found that the threshold ranges from around 5% to 17.5% (Jurewicz & Jones, 1995; Yoshino et al., 2003; 2004; Bagdassarov et al., 2009; Watson & Roberts, 2011), well below the disaggregation limit of $\sim 20\%$ (McKenzie, 1984). Theoretical calculations on the other hand have shown that melt networks can still remain interconnected at low melt fractions of $\sim 1\%$ through hysteresis in melt connectivity (Ghanbarzadeh et al., 2017).

Dihedral angles between iron-rich metallic liquids and olivine have been experimentally determined to be somewhere between 65° to 115° (Ballhaus & Ellis, 1996; Minarik et al., 1996; Shannon & Agee, 1996; Gaetani & Grove, 1999; Yoshino et al., 2004; Terasaki et al., 2005), suggesting that they form isolated pockets of melt that make intrusion of liquid iron alloys into silicates very difficult. However, most of these experiments were conducted at around upper mantle P-T conditions as these studies were investigating whether core formation could have occurred in the Earth via percolative processes. Experiments performed at higher pressures actually indicate that the dihedral angle decreases, ranging from values below 60° (Takafuji et al., 2004; Shi et al., 2013) to around 70° (Shannon & Agee, 1998; Sakai et al., 2006). This suggests that silicates at the CMB are potentially permeable enough for liquid metal to flow within interconnected networks, especially so should the fraction of liquid metal go above $\sim 5\%$ (von Bargen & Waff, 1986), and the enhanced wettability would allow for more efficient chemical interaction between the outer core and lower mantle. Draining of the liquid metal from the silicate matrix through processes such as viscous compaction would be rather effective at the lower mantle as well, but it should be noted that there is still a possibility for isolated pockets of melt to be trapped when dihedral angles are larger than the critical value of 60° and sufficient liquid has been drained until the liquid fraction goes below the percolative threshold. These experiments have also shown that the

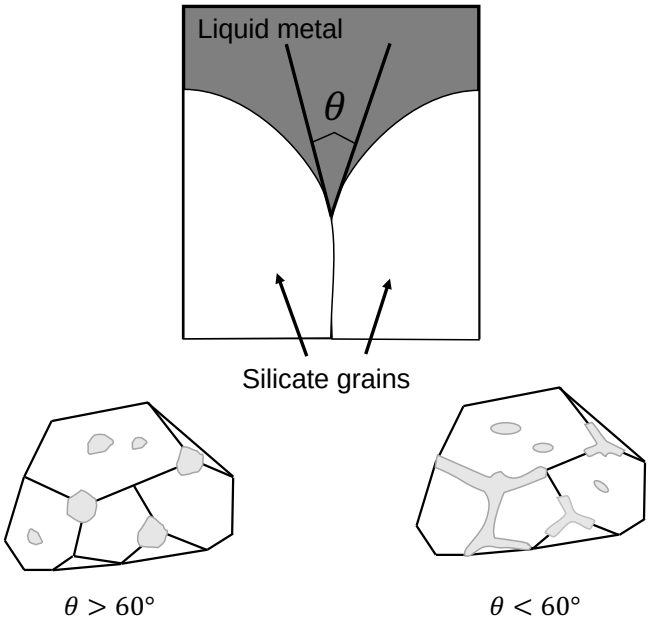

FIGURE 1.6: An illustration of the dihedral angle θ between the liquid metal and two silicate grains. At $\theta > 60^\circ$, the liquid metal will exist as isolated pockets. But if $\theta \leq 60^\circ$, an interconnected network will form and percolation of liquid metal can occur.

composition of the iron alloy affects the dihedral angle: increasing the oxygen content of the alloy decreases the dihedral angle (Sakai et al., 2006), while having an Si rich creates very large dihedral angles (Mann et al., 2008). Hence, the composition of the liquid metal is an important parameter in determining the wettability of the silicate grain boundaries.

Isostatic Protrusion of Dense Rock

In addition to dynamic topography, isostatic topography can also exist at the CMB. Since ULVZs are ∼10% denser than the ambient mantle but less dense than the outer core, parts of it can protrude into the core (just like how icebergs are partially submerged in seawater) and react with the liquid metal of the outer core (Hernlund & Tackley, 2007). Depending on how large the density contrast is between the ULVZ and the lower mantle, protrusions into the outer can be large enough to potentially overwhelm contributions from dynamic topography (2007). Furthermore, stirring of ULVZ by viscous coupling to overlying mantle flows (Hernlund & Jellinek, 2010) will cyclically dredge ULVZ material into the core, and if metal is able to wet the grain boundaries then metal-silicate interaction could extend a significant distance into the ULVZ. However, if the ULVZs are FeO rich and in direct contact with the stratified layer in the outer core, they can come into chemical equilibrium with the outer core relatively quickly which reduces the chemical flux out of the core over time. The time it takes for the ULVZs to reach chemical equilibration with the stratified layer will largely depend on the age of the ULVZ. If they originate from residual melts during the crystallisation of the BMO, the ULVZs can be as old as the Earth itself. However, this might present another issue if the viscosity of the ULVZs are much lower than the ambient mantle as

this reduces the viscous coupling and hence, the ability for plumes to entrain the core-equilibrated material. In addition, these ULVZs will have to be within close proximity of the hot spot plumes in order to transport material to the surface. Seismic studies have not found and clear relationships between the locations of hot spots and seismically detected ULVZs (Yu & Garnero, 2018).

1.3.5 Upward Sedimentation

Another grain-scale mechanism that could pass on isotopic signatures of the core into the mantle is upward sedimentation of solids from the core that can happen any time throughout Earth's history (Buffett et al., 2000). Metal intrusion at the CMB topographic low and upward sedimentation were originally proposed in order to yield a high electrically conducting layer that could explain core-mantle angular momentum exchange as evidenced by decadal variations in the length of day (e.g. Buffett, 1996; Mound and Buffett, 2006). However, they both share some similarities in that they move from a state in which silicates are immersed in metal to one in which the metal is eventually squeezed out of the sediment and returned to the core by viscous compaction. In either case, this compaction should be very rapid and efficient for grain sizes of $\sim$1 mm or larger (Buffett et al., 2000). In fact, the sedimentation mechanism has been criticised because it requires unusually small grain sizes ($\sim$1 μm or smaller) in order to retain enough metal to attain the requisite electrical conductivity (Kanda & Stevenson, 2006). Should a layer of sediments exists at the top of the outer core, the degree of compaction and efficiency of expelling liquid metal out of the matrix will influence the density, seismic velocity and electrical conductivity of this layer. Reduction in P and S velocities calculated by Buffett et al. (2000) were shown to be as large as deviations from ULVZs, but a reduction in velocity is not unique to the existence of this sediment layer and the region where the greatest seismic velocity reduction occurs is too thin to be resolved ($\sim$1-2 km). Rather than relying on seismic observations alone, the data can be combined with observed discrepancies in the Earth's nutation to better constrain the existence of this mechanism, but this depends on the electrical conductivity of the sediment layer. Estimates of conductivity are usually derived from Archie's Law, but it is uncertain if the exact relationship holds for P-T conditions at the CMB.

Isotopic equilibration between intruded metal and rock proceeds at the grain scale with a a characteristic diffusion time $l_{\mathrm{g}}^2/D_{\mathrm{i}}$, where l_{g} is the grain size and D_{i} is the diffusivity of species i. If l_{g} $\sim$1 cm, then soaking of grains in metallic fluid for mantle convection time scales of $\sim 10^7$ years will yield complete equilibration for every species i having $D_{\mathrm{i}} > 10^{-18}$ m^2/s. Since this is a rather slow diffusivity for the mantle at these conditions (Van Orman & Crispin, 2010), it is expected that most species will achieve a high degree of equilibration.

Even if compaction efficiently drains metal for reasonably modest grain sizes, it may still be possible for some small fraction of metal to remain trapped in the rock if there is a fraction below which it fails to wet the grain boundaries. In other words, if there is a critical wetting fraction ϕ_{wf} below which metal does not form an inter-connected network through which it

may readily flow between grains, then the compaction and removal of metal will cease with $\phi \approx \phi_{\mathrm{wf}}$ amount of metal trapped inside the rock.

Rayleigh-Taylor Instability of Core-Derived Sediments

During the Earth's early history when the primitive core has segregated from the magma ocean, experiments have shown that at the pressure and temperature conditions associated with the base of the magma ocean and core, Si becomes increasingly soluble in liquid metal (Hirose et al., 2017). With the subsequent onset of core cooling, the decreased solubility of Si would have supersaturate the core, resulting in the exsolution of Si. However, since the Si is chemically bonded with dissolved O in the liquid metal, the actual exsolved component is SiO_2. With SiO_2 being less dense than liquid metal, it is expected to rise to the top of the core and accumulate as a layer due to the sharp viscosity contrast with the solid silicate mantle (Helffrich et al., 2018). However, since the density of SiO_2 is still lower than that of seismologically determined values of the present-day mantle (Hirose et al., 2005), the growth of the more buoyant layer at the CMB creates a Rayleigh-Taylor instability with a growth time of τ_{RT} that is proportional to $\mu/\Delta\rho g h$, where $\Delta\rho$ is the density difference between the overlying mantle and SiO_2 layer, and μ and h are the viscosity and thickness of the layer respectively. As the SiO_2 rises into the lower mantle in the form of diapirs, they detach to form blobs with diameters estimated to be the same as the thickness of the Si layer (Helffrich et al., 2018). The blob size determines how fast it ascends in the mantle, at least until it reaches a point of neutral buoyancy that might be somewhere in the middle of the lower mantle (assuming suitable values of the Grüneisen parameter and SiO_2 equation of state). If this velocity is 10-1000 times smaller than mantle convective speeds, it can be expected that the SiO_2 blobs will be entrained by mantle flow instead of rising through it passively (2018). Conditions that favour fast mantle ascent include lower ambient mantle viscosities due to higher temperatures and large core cooling rates. The former acts by directly reducing the viscous drag on the blob, while the latter acts to increase the size of the blob and hence reduce drag. Such conditions were likely to have happened in the early Earth, where cooling with the rapidly convecting magma ocean above might have given rates of 300-2000 K/Gyr (Solomatov & Stevenson, 1993; Lebrun et al., 2013). Although the SiO_2 rich domains can exhibit strong velocity contrasts with the ambient lower mantle to create seismic scattering (Helffrich et al., 2018), these are non-unique features that can be attributed to other heterogeneities in the lower mantle (e.g. Kaneshima, 2016).

1.3.6 Poro-Elastic Entrainment

Petford et al. (2005) suggested a poro-viscoelastic entrainment mechanism in the D" layer, where dilatancy instabilities caused by deviatoric shear stresses drive liquid metal upwellings at the CMB during geologically recent times. Their results showed that in order for this mechanism to transport significant liquid core metal upwards, the D" layer needs to experience strain rates larger than 10^{-12} s^{-1}. However, it remains unclear if such high strain rates are possible in the lower mantle or that the elastic dilatant properties of materials at the D"

allow for such mechanism to occur over geologic time. This mechanism can also produce an electrically conductive layer at the CMB on the mantle side which can, in theory, create variations in the length-of-day. However, there are also other mechanisms mentioned in this chapter that can create such a conductive layer without resorting to high strain rates at the CMB.

1.3.7 Thermodiffusion

Another proposed mechanism for core-mantle exchange is the thermodiffusion of iron isotopes at the CMB that can occur any time throughout Earth's history. Lesher et al. (2020) recently investigated the fractionation of ^{56,57}Fe in pure Fe and FeNi alloy liquids over steep thermal gradients at 2 GPa, as they believed that this mechanism can explain the iron enrichment of ULVZs and possibly lead to high ^{56,57}Fe/^{54}Fe ratios in OIBs. Even though the experimental conditions were far from CMB pressure and temperature conditions, they used the Chapman-Enskog kinetic theory of thermodiffusion to estimate the magnitude of isotope fractionation α_0 in core liquids and extrapolated it to the relevant conditions. They subsequently modelled the enrichment of ^{57}Fe within a basal thermal boundary layer using the extrapolated fractionation factor which then allows heavy iron isotopes to be entrained in upwelling plumes, thereby carrying the unique isotopic signal into upper mantle and beyond. Based on their estimates, they believed that the asthenosphere can inherit a positive ^{57}Fe anomaly by as much as 0.05‰ over geologic time.

However, as seen from the data collected from different OIBs (Konter et al., 2016; McCoy-West et al., 2018; Soderman et al., 2021), a number of samples have $\delta^{56,57}$Fe values that are significantly higher than 0.05‰, indicating that this mechanism might not be very effective in imparting heavy $\delta^{56,57}$Fe to mantle rocks. Instead, some other processes occurring in the mantle might be affecting the $\delta^{56,57}$Fe values of OIB magmas prior to their eruption such that the lavas have $\delta^{56,57}\text{Fe} \geq 0.05‰$. This is further supported by the unobserved correlation between $\delta^{56,57}$Fe and other geochemical tracers such as ^{3}He/^{4}He and μ^{182}W (McCoy-West et al., 2018; Soderman et al., 2021).

An important point to note about this mechanism is that there is no indication of the process of liquid iron infiltrating into the lowermost mantle in order for iron isotopes fractionation across a basal thermal boundary above the CMB. In addition, the amount and type of light elements in the core fluid might have an influence on the magnitude of isotope fractionation since it has been suggested that light alloying elements can accumulate at the top of the outer core to create a gravitationally stratified layer (Fearn & Loper, 1981).

Their models also assume that the metal remains inter-connected in the silicate matrix of the mantle. In such a state, large pressure gradient differences arise between the liquid metal and mantle solids, which would lead to compaction/closure of the pore spaces. This would severely limit the maximum column height of metal that can be supported in the mantle as shown in the calculations of Poirier and le Mouël (1992). Detection of this mechanism using

other means would be rather challenging since iron isotope fractionation will not significantly alter the physical properties of the whole rock.

1.3.8 Morphological Instabilities and Surface Tension

One of earliest mechanism proposed for core-mantle exchange was via capillary action (Poirier & le Mouël, 1992), where liquid metal infiltrates and wets the grain boundaries while dissolving the adjacent silicate material. This mechanism can occur as long as penetration of liquid iron along silicate grain boundaries is energetically favourable. Based on their estimates, the liquid is only able to penetrate up to a height of at most 100 m that is far smaller than the lengthscales of low velocity patches in the D" (Williams & Garnero, 1996).

In a more recent study, high pressure and temperature experiments were conducted to investigate the penetration of liquid iron into (Mg,Fe)O caused by morphological instabilities (Otsuka & Karato, 2012; Yoshino, 2019). The instabilities are a result of a gradient in FeO concentration, where FeO content increases with distance from an interface between (Mg,Fe)O and an iron-rich melt. The wavelength grows as a function of both capillary length and FeO gradient concentration and, with some extrapolation, it was predicted that an iron-enriched layer could grow up to 100 km after 4 billion years. Even though this mechanism seems to provide a chemically (and possibly isotopically) altered layer that is significantly thicker, it has to be emphasised that the mineralogy of the lower mantle is largely dominated by bridgmanite and post-perovskite (Irifune & Tsuchiya, 2015) and that iron diffusion in these minerals are much slower (Holzapfel et al., 2005). Hence, if morphological instability is the dominant mechanism for iron enrichment near the CMB, the extent of the thickness will be largely dominated by the volume fraction of (Mg,Fe)O.

The plausibility of liquid iron infiltration via morphological instabilities can also be analysed simply from energy considerations. For simplicity, we assume that the metal drops are spherical with diameter r_0 and changes in chemical potential energy across the interface can be used to do the following work : (1) increasing the gravitational potential energy, and (2) increasing the surface energy of the drop.

The change in gravitational potential energy ΔU to raise a drop by height Δh is given by $\Delta U = \Delta\rho V g \Delta h$ where $\Delta\rho$ is the density contrast between the liquid metal and solid silicate, V is the volume of a drop, and g is the acceleration due to gravity. For a spherical drop, $V \propto r_0^3$ and if Δh is recast as cr_0 where c is a constant, substituting these two values back into ΔU will show that $\Delta U \propto r_0^4$. This means that with increasing drop size, the energy required to do work against gravity becomes disproportionately larger, specifically with a 4th power.

Similarly, the change in surface energy ΔS related to increasing (or decreasing) the surface area of a single drop $\Delta\sigma$ is given by $\Delta S = \gamma\Delta\sigma$ where γ is the surface tension, which is also sometimes known as the interfacial energy or grain boundary energy, and is usually assumed to be constant within a certain range of P-T conditions. The change in surface area can be approximated to scale according r_0^2 (i.e. $\Delta\sigma \propto r_0^2$) which also implies that the

energy required to change the surface area does not scale linearly as well. It is important to note that while changing the surface area does not necessitate a simultaneous change in volume, for a given volume of metal drop, there is a fundamental limit to which how much the surface area can decrease to. Since the most compact 3D shape is a sphere, where the sphere has the smallest surface area-to-volume ratio, for a given volume V the minimum surface area a metal blob can take is $\sqrt[3]{36\pi V^2}$.

Hence, if we are to consider that there is a much larger number of liquid metal drops rising above from the outer core into the ferropericalse component of the mantle (like what is shown in Otsuka and Karato, 2012), there must be significant chemical disequilibrium between the mantle and outer core to provide the energy cost to not just work against gravity but as well as creating discrete pockets of metal blobs of different surface topologies. Moreover, as more metal blobs react with the ferropericalse matrix and rise against gravity, there will be lesser amounts of chemical potential energy left for the remaining metal blobs to do work with. This mechanism may become less effective over time to a point where the ferropericlase becomes completely chemically equilibriated with no available chemical potential energy available left in the system.

Finally, it must be emphasised that geochemistry constraints require highly efficient compaction of rock and expulsion of almost all metal back to the core, and the only way for this to work is if the wetting fraction of metal in the rock is very small. This means that the drops in the mantle from the morphological instability would have to be at a concentration lower than permitted by the geochemistry such that no excess siderophiles can be detected in the rocks (e.g. Ireland et al., 2009; Ireland et al., 2011; Mundl-Petermeier et al., 2017).

Core-Mantle Interaction Mechanisms					
	Diffusion across CMB	Chemical Exchange with BMO	Liquid Metal Intrusion	Isostatic Protrusion	Upward Sedimentation
Timing of interaction	After magma ocean solidification	During the first billion years	Recent	Ancient	Recent
Mantle volume	About 1%	As much as 25%	About 1%	About 1%	About 1%
$^{3}He/^{4}He$	Small He concentration in the core	U+Th enrichment in residual melts can suppress signal	Small He concentration in the core	Small He concentration in the core	Small He concentration in the core
$\mu^{182}W$	Small volumes	Depends on original Hf/W in BMO	Small volumes	Small volumes	Small volumes
D/H	S-L fractionation	L-L fractionation	S-L fractionation	S-L fractionation	S-L fractionation
Os isotopes	Small volumes and S-L fractionation	Depends on original Pt/Os and Re/Os in BMO and core	Small volumes and S-L fractionation	Small volumes and S-L fractionation	Small volumes and S-L fractionation
Excess siderophile elements	Very little	None expected	Depends on compaction	Depends on compaction	Depends on compaction
Advantages	Can transfer core signals if mantle is undersaturated and/or core is saturated	Higher diffusivities can occur in magma ocean	Isotope ratios from core can be transferred without excess siderophiles	Material might become chemically equilibrated if remain undisturbed	Can possibly account for variations in length-of-day
Disadvantages	Very inefficient in silicates. Highly dependent on grain boundary volumes	Secondary fractionation effects can occur during freezing of BMO	Residence time of mantle material at CMB unconstrained	ULVZs not detected at every OIB location. Unconstrained plume entrainment efficiency	Mixing of exsolved SiO_2-rich domains from the core will dilute isotope signals

Core-Mantle Interaction Mechanisms				
	Poroelastic Entrainment	Thermodiffusion	Morphological Instabilities	Surface Tension
Timing of interaction	Recent	Any time	Any time	Any time
Mantle volume	About 1%	About 1%	About 1%	Less than 1%
^{3}He/^{4}He	Small He concentration in the core			
μ^{182}W	Small volumes			
D/H	S-L fractionation			
Os isotopes	Small volumes and S-L fractionation			
Excess siderophile elements	Somewhat significant, depends on compaction	Depends on liquid iron entrainment process into lower mantle	Significant	Significant
Advantages	Can possibly account for unique isotope and chemical ratios found in OIBs	Iron isotope fractionation can be potential signal from the core	Can possibly account for unique isotope and chemical ratios found in OIBs	Can possibly account for unique isotope and chemical ratios found in OIBs
Disadvantages	Requires high strain rates at the CMB. Physical entrainment of core liquid	Iron isotope fractionation does not correlate with other isotope tracers	Energetically unfeasible. Physical entrainment of core liquid	Very inefficient. Physical entrainment of core liquid

TABLE 1.1: A table that compares and summarises the key aspects of each core-mantle interaction mechanism that has been discussed in existing literature and the associated uncertainties of each isotope tracer. S-L: Solid-liquid. L-L: Liquid-liquid.

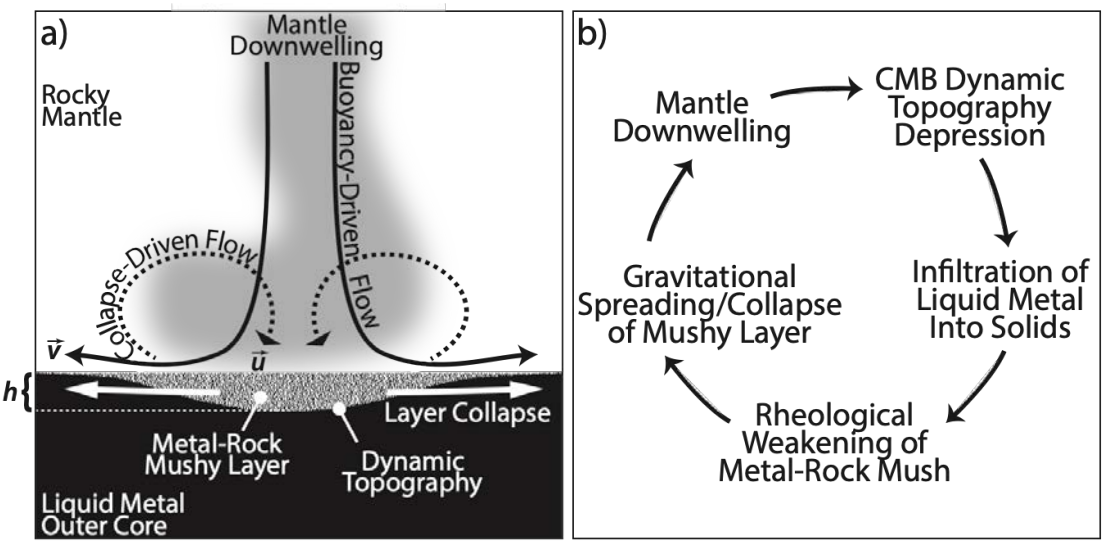

FIGURE 1.7: (a) Schematic illustration of the hybrid mechanism. h represents the thickness of the mushy layer, which is similar to the amplitude of dynamic topography. Black arrows illustrate downwelling mantle flow that induces dynamic topography. (b) Flow chart of the soft CMB mechanism explicitly showing the feedback loop.

1.4 New Hybrid Mechanisms for Core-Mantle Chemical Exchange

While it is useful to consider isolated mechanisms for core-mantle exchange, in reality there may be a large suite of mechanisms that are operating in parallel. This is how natural processes often work, and one of the intriguing possibilities is that different mechanisms may combine to produce emergent behaviors owing to feedbacks between different parallel processes. Such emergent behavior is a common theme in planet science, ranging from composite processes like sand ripples, mantle convection, the geodynamo, plate tectonics, and life. In any case, we see that nature may find additional degrees of freedom, or new ways of operating, when multiple degrees of freedom and mechanisms become available.

1.4.1 Gravitational Collapse of Metal-Silicate Mush

In the vicinity of mantle downwelling flows, the CMB is depressed into the core as a consequence of deviatoric stresses derived from buoyancy-driven mantle convection. The expected dynamic topography at the CMB is of order $\sim$1 km (Olson et al., 1987). At CMB pressure-temperature conditions, a liquid iron-alloy is expected to "wet" solid grain boundaries and intrude between the grains to form an inter-connected network (Takafuji et al., 2004; Mann et al., 2008). Combined with the excess fluid pressure head induced in topographic lows, this drives intrusion of metal upward into submerged basal mantle rock (Kanda & Stevenson, 2006). The amount of metal that may be ingested into the mushy region is limited to the disaggregation fraction since solids must maintain a continuous touching network in order to transmit a contrasting pressure gradient relative to liquid metal, and may only penetrate into the mantle by an amount similar to the magnitude of CMB topography (i.e., $\sim$1 km).

A metal mush mixture formed in CMB topographic lows will be buoyant with respect to the underlying core, and may become rheologically weakened, thus raising the possibility of gravitational collapse. Lateral spreading of metal mush draws more mantle down from above to maintain the dynamic topography dictated by large scale mantle convection (fig 1.7a). By creating a non-linear feedback in the system, such collapse enhances circulation of mantle rock into and through the mushy layer (fig 1.7b). The combined effects result in a "softening" of the lower boundary condition for mantle convection in downwelling regions. As the metal mush spreads laterally and migrates away from mantle downwellings, the layer undergoes viscous compaction, squeezing liquid metal out from pore spaces that subsequently drains back into the liquid outer core. Efficient compaction in principle allows for rocks with core-like isotopic signatures to be transported to the surface without bearing excess siderophile elements (Puchtel et al., 2005; Ireland et al., 2011).

The "soft CMB" mechanism considered here is based on the action of dynamic topography, and may operate continuously throughout Earth's history. However, dense (e.g., iron oxide-enriched) structures in the deep mantle may also depress into the core as the CMB analogue of "isostatic" topography (Hernlund & Tackley, 2007; Lassak et al., 2010; Hernlund & McNamara, 2015). Infiltration of metal and interaction in these kinds of dense rocky structures is also possible, and such materials may be sequestered over geologically long time scales prior to upward entrainment by mantle convection into the shallow mantle. Dense chemical structures may be stirred by viscous coupling to larger scale mantle convection flows (Hernlund & Jellinek, 2010), leading to extensive mixing between metals and rocks over time. The situation may be even more complex, as deeply subducted lithospheric rocks that have chemically reacted with liquid metal in dynamic topography lows may become denser as a consequence, and as a result accumulate beneath upwelling regions. Other possibilities can include being entrained into other compositionally dense structures whose origin is distinct from core-mantle interaction. Even though the range of possibilities is very broad, such diversity may help explain the range of core-mantle interaction ages suggested by geochemical studies (Brandon et al., 2007; Mundl-Petermeier et al., 2019; Mundl-Petermeier et al., 2020). Just like flowchart that is shown in figure 1.5, the transfer process associated with this mechanism from the original heterogeneity to the basalt product is shown in figure 1.8. Apart from the processes that occur prior to and after the interaction as discussed in section 1.3.1, additional factors that can affect the isotopic ratios in the reacted rock include the degree of metal intrusion in the mushy layer, the flux of rock reacting with the core liquid, and the compaction efficiency once the reacted rock leaves the mushy zone. The uncertainties in the data that can arise from these processes have to be taken into account when considering whether the isotope data has been generated via this interaction mechanism. To better understand the physics of this mechanism, a basic illustrative model with an isovisocus and temperature dependent rheology will be described and discussed in Chapter 2 and Chapter 3 respectively. This will be followed by a thermochemical model in Chapter 4 where buoyancy effects associated with compositional changes are studied.

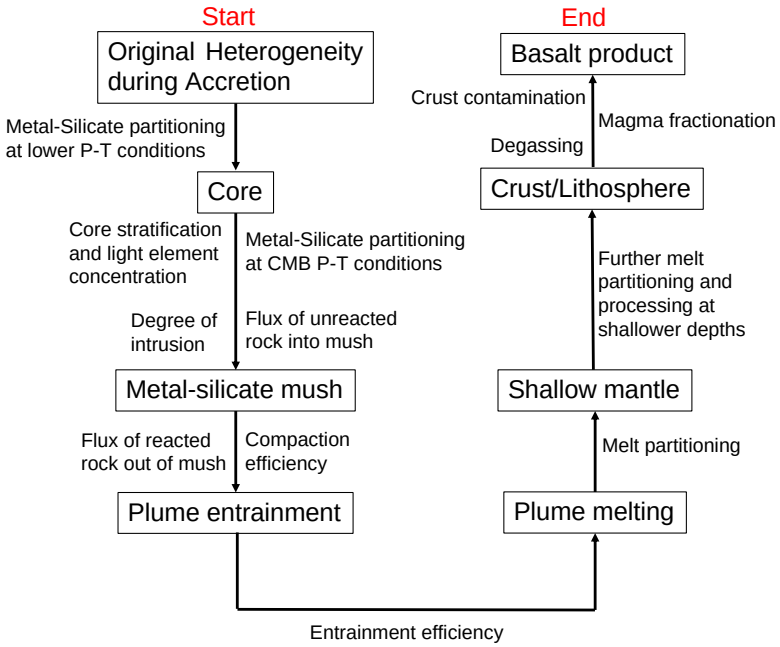

FIGURE 1.8: A flowchart describing the transfer process of the original heterogeneity to the final basalt product that appears on the surface of the Earth and the various events occurring in between that can affect the final measurement for the new hybrid mechanism involving the gravitational collapse of a metal-silicate mush.

1.5 Summary

This chapter has provided a summary of the present geochemical evidence and mineral physics constraints on core-mantle interaction, a review of existing interaction mechanisms that have been proposed in the literature, as well as the motivation for understanding the processes happening at the CMB. In light of how different natural mechanisms and processes can operate in parallel, a new emergent mechanism for core-mantle interaction is proposed. This new hybrid mechanism is termed “soft CMB" and will be investigated using different mantle convection models to study the effects on mantle and chemical dynamics in the lower mantle. Chapter 2 will introduce a basic model using isoviscous and isochemical mantle convection, followed by the additional complexity of temperature-dependent viscosity in Chapter 3. Chapter 4 then studies the effects of this mechanism in the context of thermochemical convection, and Chapter 5 will reiterate the limitations of this mechanism and future research directions.

2 | The Hybrid Mechanism in an Isoviscous Mantle

2.1 Basic Illustrative Model

Although the dynamics of mantle convection can be highly complex, this chapter is focused on building a basic illustrative model by assuming isoviscous mantle convection of an incompressible Boussinesq fluid in a Cartesian geometry. At the limit of infinite Prandtl number, the governing equations of motions in Cartesian coordinates are as follows (e.g. Schubert et al., 2001):

$$\eta_0 \nabla^2 \vec{v} - \nabla P_v = \rho_0 [1 - \alpha (T - T_0)] g \hat{z} \tag{2.1}$$

$$\nabla \cdot \vec{v} = 0 \tag{2.2}$$

where η_0 is the mantle dynamic viscosity, $\vec{v}$ is the velocity field, P_v is the pressure, ρ_0 is the reference density, α is the thermal expansivity (which is assumed constant), g is the acceleration due to gravity, T is temperature, and T_0 is the reference temperature.

Normal stresses σ_{zz} exerted by the convective flows $\vec{v}$ on the CMB raise a dynamic topography h given by,

$$h(x,y) = \frac{\sigma_{zz}(x,y,z=0)}{\Delta \rho g} \tag{2.3}$$

The density contrast $\Delta\rho$ is defined as:

$$\Delta\rho = \begin{cases} \rho_m - \rho_{mix} = (1-\phi)(\rho_m - \rho_r) & \text{if } \sigma_{zz} < 0 \\ \rho_m - \rho_r & \text{if } \sigma_{zz} \geq 0 \end{cases} \tag{2.4}$$

where ϕ is the volume fraction of liquid metal (assumed to be constant) intruded into the submerged portions of the metal-rock mush (i.e., where $h < 0$), and ρ_m and ρ_r are the densities of liquid metal (≈ 9900 kg m^{-3}) and mantle rock (≈ 5500 kg m^{-3}), respectively. The quantity ρ_{mix} is the density of the mushy metal-rock mixture and for a given ϕ is defined as $\rho_{mix} = \phi\rho_m + (1-\phi)\rho_r$. It is assumed that only large-scale buoyancy forces from mantle convection are responsible for creating dynamic topography at the CMB and assuming that

the mantle follows a Newtonian rheology, the vertical stress is

$$\sigma_{zz} = 2\eta_0 \frac{\partial v_z}{\partial z} \tag{2.5}$$

Since only the dynamic topography that intrudes into the core is of concern (i.e. when $h < 0$), the positive values of σ_{zz} at the CMB are ignored and by combining equations (2.4) and (2.5) with (2.3), the dynamic topography can be re-expressed as

$$h(x,y) = \frac{2\eta_0}{(1-\phi)(\rho_m - \rho_r)g} \left.\frac{\partial v_z}{\partial z}\right|_{z=0} \tag{2.6}$$

It is assumed that decompaction and infiltration of metal into submerged rock occurs on time scales much shorter than the residence time of mantle rocks at the CMB. In other words, the vertical component of the Darcy velocity for upward metal percolation is assumed to be large enough to keep up with the rate of mantle material being drawn down into the mushy region such that the depth of the dynamic topography h is equivalent to the thickness of the mushy layer. This assumption can be written as,

$$u_z^D(z=0) + v_z(z=0) = 0 \tag{2.7}$$

where u_z^D is the Darcy velocity and v_z is the mantle flow velocity just above the mushy layer.

In addition, the reverse process of compaction and expulsion of metal back to the core as the mush moves laterally away from depressions occurs on similarly short time scales. Variations in the mushy layer are expected to occur over lateral length scales L that are much larger in comparison to h. In other words, since $h/L \ll 1$, the “thin-layer approximation" from lubrication theory can be applied to describe gravitational collapse of the mushy layer (Reynolds, 1886; Hier-Majumder & Revenaugh, 2010; Hernlund & Bonati, 2019). Gravitational collapse of the mushy layer can be approximated as a diffusion process with

$$\frac{\partial h}{\partial t} = \frac{\Delta\rho g}{12\mu} \nabla_H^2 h^4 \tag{2.8}$$

where t is time, μ is the (assumed constant) viscosity of the mushy layer, and ∇_H^2 is the horizontal Laplacian operator ($\nabla_H^2 = \partial^2/\partial x^2 + \partial^2/\partial y^2$).

Mantle viscous forces are assumed to maintain the equilibrium dynamic topography described by equation (2.3), keeping h constant for a given buoyancy-driven convection flow. Therefore, the effect of lateral spreading in the layer is to draw down solid mantle from above to maintain the topography h that is dictated by the large-scale buoyancy-driven flow. Since the rate of change of the mushy-layer thickness $\partial h/\partial t$ has contributions from both the silicate and metallic components, the combined vertical velocity of both components at the mantle-mushy layer interface can be expressed as $\bar{U}_z(x,y)$ such that

$$\frac{\partial h}{\partial t} = \bar{U}_z \tag{2.9}$$

However, with only the silicate component being exchanged across this interface, the metallic component has to be subtracted from the total velocity to obtain the induced draw-down velocity of silicate solids from above at the top of the mushy layer, which is called u_{z+}. As a result,

$$u_{z+} = (1-\phi)\bar{U}_z \tag{2.10}$$

where the factor $(1-\phi)$ accounts for the solid flux into the mushy region that is a mixture of both solids and metals. By combining equations (2.8), (2.9) and (2.10) together, an equation relating the induced draw-down velocity with the gravitational collapse of the mushy layer is obtained:

$$u_{z+} = \frac{\Delta\rho g(1-\phi)}{12\mu}\nabla_H^2 h^4 \tag{2.11}$$

A secondary collapse-driven flow $\vec{u}$ thus develops in the mantle that is coupled to gravitational spreading of the mushy layer described by equation (2.11) at the lower boundary. With the assumption of a linear rheology, the collapse-driven flow $\vec{u}$ can be solved separately from buoyancy-driven convection $\vec{v}$ at each time step by solving the following Stokes' and continuity equations:

$$\eta_0\nabla^2\vec{u} - \nabla P_u = \rho_0 g\hat{z} \tag{2.12}$$

$$\nabla\cdot\vec{u} = 0 \tag{2.13}$$

where P_u is the pressure field arising from the flow of $\vec{u}$. These two equations have to be solved with the the inhomogeneous boundary condition given by equation (2.11) at each time step. $\vec{u}$ is then combined with $\vec{u}$ obtain a total effective velocity $\vec{v}_{\text{eff}} = \vec{v} + \vec{u}$ that is used to advect temperature in the mantle according to the following equation:

$$\frac{\partial T}{\partial t} + \vec{v}_{\text{eff}}\cdot\nabla T = \kappa\nabla^2 T \tag{2.14}$$

where κ is the thermal diffusivity.

Small variations in boundary topography are neglected when solving for $\vec{v}$, for which free-slip (i.e., tangential stress-free) and impenetrable (i.e., $v_z(x,y,z=0)=0$) boundary conditions at the CMB are assumed. However, an estimate of the vertical velocity due to buoyancy-driven flow by itself (independently of collapse-driven flow) at the top of the layer is still needed. To do this, $v_z(x,y,z)$ is approximated about the point $z=0$ using the Maclaurin series

$$v_z(x,y,z) \approx v_z(x,y,0) + \left.\frac{\partial v_z}{\partial z}\right|_{z=0} z + \left.\frac{\partial^2 v_z}{\partial z^2}\right|_{z=0}\frac{z^2}{2!} + \dots \tag{2.15}$$

Since the boundaries are said to be impenetrable, the first term on the right side disappears. Ignoring the terms z^2 and larger, the vertical velocity at h can be approximated as

$$\bar{V}_z(x,y) \approx \left.\frac{\partial v_z}{\partial z}\right|_{z=0} h \tag{2.16}$$

where $\bar{V}_z(x,y) = v_z(x,y,z=h)$. Since $\bar{V}_z$ contains contributions from both silicate and metallic components as well, the latter has to be subtracted from $\bar{V}_z$ to obtain the velocity of

the silicate component v_{z+}. Hence,

$$v_{z+} \approx (1-\phi)\left.\frac{\partial v_z}{\partial z}\right|_{z=0} h \tag{2.17}$$

where the same $\partial v_z/\partial z$ is used to compute h in equation (2.3). This will be used to measure the relative contributions of solid flux through the metal-rock mush due to buoyancy-driven convection in order to compare it to collapse-driven flux.

The above assumptions are made in the context of considering the onset of small-scale collapse-driven flow as the viscosity of the mushy layer is reduced from ambient mantle values. However, these assumptions may not be suitable for the more general case in which the viscosity of the mush is even smaller, a topic that will be re-visited in the discussion.

2.2 Methods

Although the equations in the preceding section describe a 3D Cartesian geometry, they are equally applicable in 2D. A variety of numerical methods and tools are widely available to solve the Stokes' equations in 2D, but this section will describe the main method that is used in this study.

Equations (2.1) and (2.2) are firstly discretized using the finite difference approximation. The velocity fields $\vec{v}$ and pressure P_v from buoyancy-driven flows are subsequently obtained by solving the equations iteratively using the SIMPLE (Semi-Implicit Method for Pressure-Linked Equation) method (Patankar, 2018) which further mathematical details can be found in Ismail-Zadeh and Tackley (2010). The dynamic topography h at the CMB is evaluated from v_z using equation (2.6), which is then used to calculate u_{z+} in equation (2.10). This becomes the lower boundary condition in equation (2.12) which is solved with equation (2.13) using the same SIMPLE method to obtain the velocity fields $\vec{u}$ and pressure P_u associated with the collpase-driven flows. Lastly, $\vec{v}$ and $\vec{u}$ are summed together to obtain an effective velocity v_{eff} to advect the temperature field as in equation (2.14). This concludes one timestep and the process repeats again. To minimise numerical diffusion when solving the temperature equation (2.14), a flux conservation scheme is used with superbee (Roe, 1986) as the slope limiter function of choice.

To ensure that the initial conditions have no significant impact on the final behaviour of the system, the model is initiated from a quasi-steady convection solution with a downwelling in the middle of the domain and upwellings at the edges.

2.3 Results

We solved for mantle convection flow in 2D Cartesian geometry over a domain measuring 2000 km by 1000 km (length by width) and grid resolution of 81 by 41 with a Rayleigh number

$$Ra = \frac{\rho_r g \alpha \Delta T H^3}{\eta_0 \kappa}, \tag{2.18}$$

Parameter	Value	Unit
ρ_r	5500	kg m^{-3}
ρ_m	9900	kg m^{-3}
ϕ	0.2	–
α	2.5×10^{-5}	K^{-1}
T_0	2500	K
g	10	m s^{-2}
κ	10^{-6}	m^2 s^{-1}
η_0	$1.375 \times 10^{21} - 1.375 \times 10^{23}$	Pa s
$\xi \left(= \frac{\mu}{\eta_0}\right)$	$10^{-6} - 10^{-5}$	–

TABLE 2.1: List of parameters and values used in the numerical calculations.

for $Ra = 10^4 - 10^6$, where ΔT is the super-adiabatic temperature change across the mantle, and H is the mantle thickness. Ra is varied by changing η_0 while holding other quantities constant. The values used for the parameters are described in Table 2.1. Two different viscosity contrasts $\xi = \mu/\eta_0$ are considered here: 10^{-5} and 10^{-6}. The top and bottom boundaries are free slip and are kept at 2500 K and 3500 K respectively, while the vertical sides are periodic. Larger values (i.e., higher mushy layer viscosities) do not yield any significant collapse-driven flow. These ratios capture the behavior at the point where collapse-driven flux through the mushy layer becomes comparable in magnitude to buoyancy driven-flux due to large-scale convection.

The temperature field, mushy layer thickness, and streamlines for both buoyancy-driven flow Ψ_v and flow due to the gravitational collapse of the mushy layer Ψ_u for $Ra = 10^4$ and $\xi = 10^{-6}$ are shown in Figures 2.1a, 2.1b, 2.1c, and 2.1d, respectively. The buoyancy-driven flow follows typical convective flow patterns, whereas for the collapse-driven flow, a secondary circulation pattern is observed in the vicinity of the downwelling just above the CMB. The secondary circulation arises from gravitational collapse of the mushy layer and it can be seen from the streamlines (Fig. 2.1d) that downwelling flows are indeed enhanced, especially close to the CMB.

The pattern of $\vec{u}$ and $\vec{v}$ (Fig. 2.1c-d) do not change significantly over the parameter ranges considered here. However, their amplitudes are sensitive to the input parameters. This leads to an enhancement of solid flux through the mushy layer that can be quantified as a "gain" G defined as:

$$G = \frac{F_{cd}}{F_{bd}} = \frac{\int_S \frac{\rho_r}{2}(|u_{z+}| - u_{z+})dS}{\int_S \frac{\rho_r}{2}(|v_{z+}| - v_{z+})dS} \tag{2.19}$$

where F_{cd} and F_{bd} are the mass fluxes due to the collapse-driven and buoyancy-driven flows respectively, and S is the mantle-mushy layer interface. The fluxes in equation (2.19) is written with a "rectified" velocity because the flux into the layer is only non-zero when v_{z+} and u_{z+} is less than 0. A plot of G as a function of Ra for two viscosity ratios are shown in Figure 2.2. The gain decreases moderately as Ra increases, while an order of magnitude decrease in ξ leads to an order of magnitude increase in G.

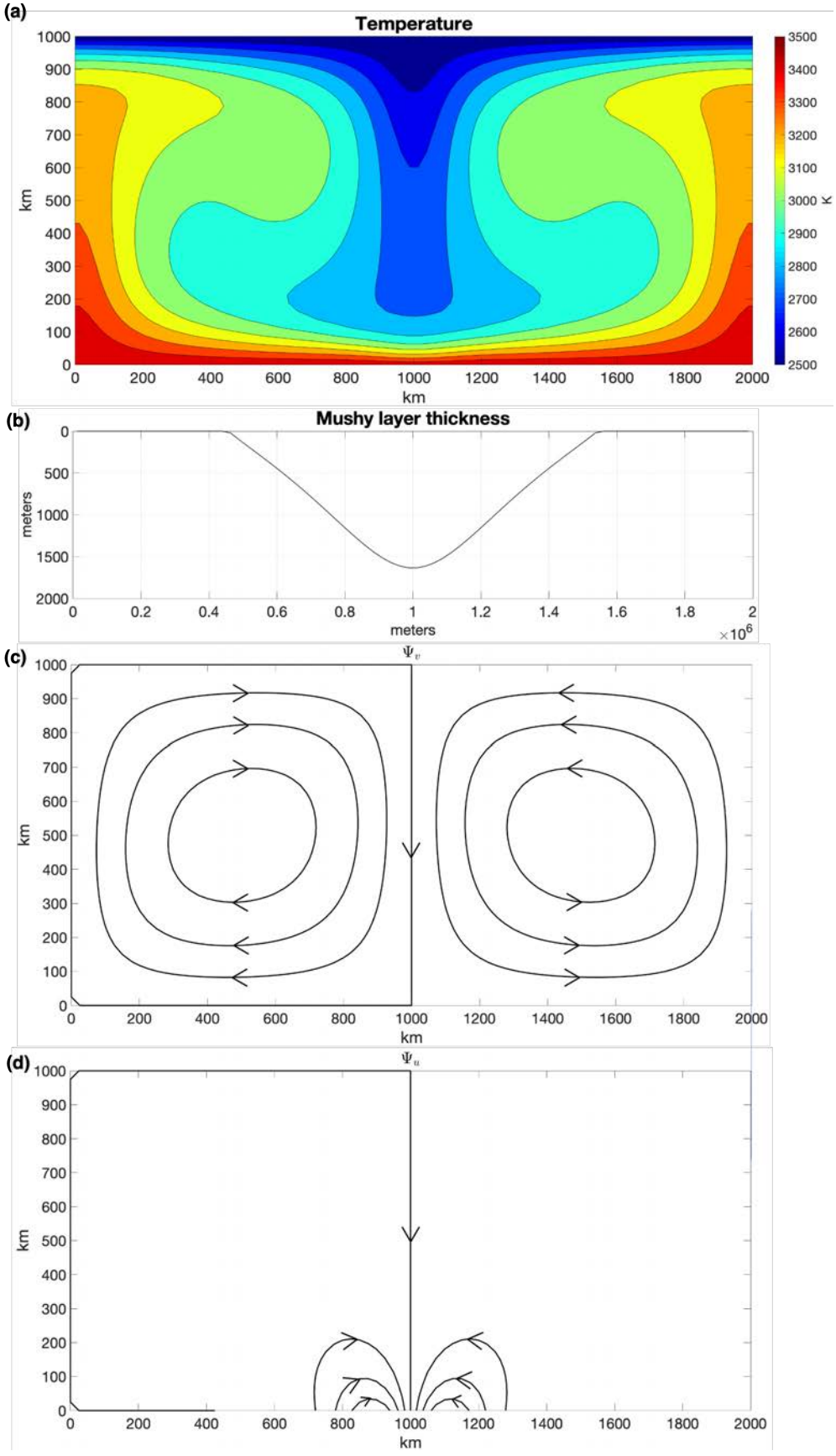

FIGURE 2.1: Results for $Ra = 10^4$ and $\xi = 10^{-6}$ at steady state. (a) Temperature field. (b) Mushy layer profile and thickness induced by deviatoric stresses at the CMB. (c) Streamlines of buoyancy-driven flow with black arrows indicating the direction of the flow. (d) Streamlines of collapse-driven flow at the CMB with black arrows indicating the direction of the flow.

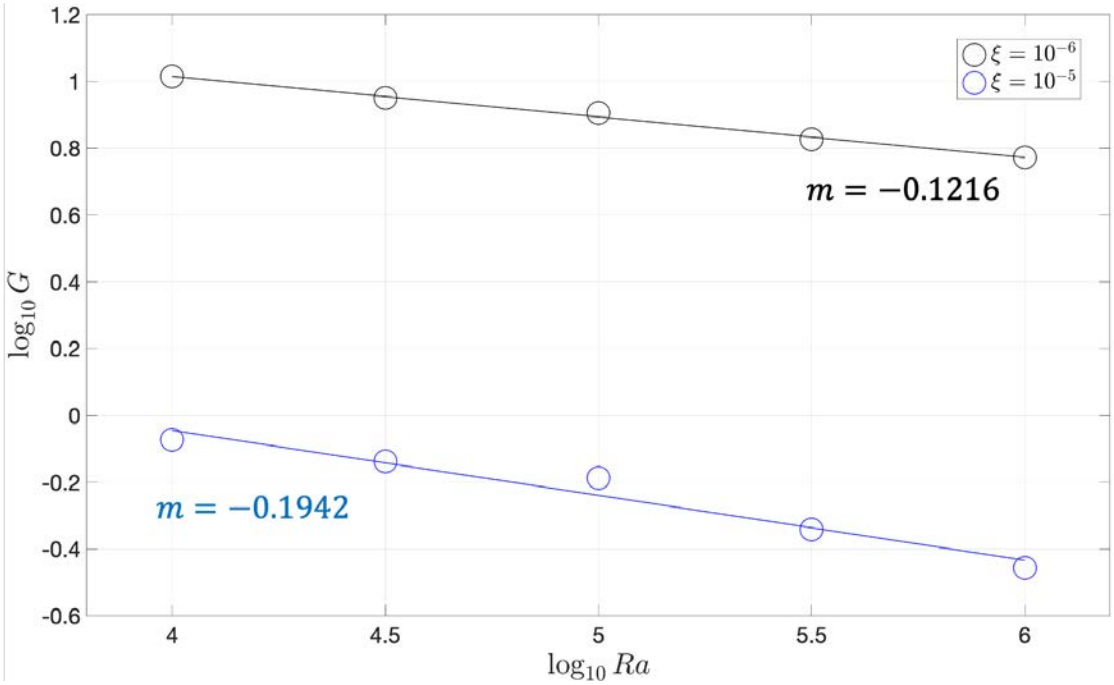

FIGURE 2.2: Plot of G against Ra in log scale. Lines show the least squares linear fit of $\log_{10} G$ with $\log_{10} Ra$. The slope m represents the exponent in the following expression $G \propto Ra^m$. Black circles and blue circles correspond to $\xi = 10^{-6}$ and $\xi = 10^{-5}$ respectively.

2.4 Discussion

The models show that collapse-driven flux reaches parity with buoyancy-driven flux through the mushy layer for $\xi \sim 10^{-5}$. As shown in Figure 2.2, there is a modest decrease in G with increasing Ra, such that this basic conclusion is unlikely to change significantly (at the order of magnitude level) even allowing for broad uncertainties in lowermost mantle properties. G decreases with Ra because mantle viscosity (η_0) is used as the control variable for convective vigor, thus a reduction in viscosity (increase in Ra) decreases the magnitude of deviatoric stresses acting on the CMB topography more so than flow velocities increase with Ra ($v \propto Ra^{2/3}$) (Fig. 2.3a). This reduction in topography has a strong effect on gravitational collapse due to the non-linear dependence upon h^4 in the diffusion operator of Equation (2.8). The value of ξ is also an important variable that determines which type of flow dominates the system. The mass flux of each flow-type according to the velocities near the CMB can be scaled as such: $u \sim \Delta\rho g h^4/(\mu L^2)$ and $v \sim \delta\rho g H h/\eta$ where $\delta\rho$ is the density variation caused by buoyancy forces inside the mantle. Comparing the two velocities gives

$$G \propto \frac{u}{v} \sim \left(\frac{\Delta\rho}{\delta\rho}\right)\left(\frac{h^3}{HL^2}\right)\left(\frac{1}{\xi}\right) \tag{2.20}$$

From Equation (2.3), a scaling for h according to the densities is obtained as follows: $h/H \sim \delta\rho/\Delta\rho$. This is plugged back into Equation (2.20) to eliminate the density ratio and H which

finally gives the following scaling for G

$$G \sim \left(\frac{h}{L}\right)^2 \left(\frac{1}{\xi}\right) \tag{2.21}$$

Equation (2.21) tells us that the gain depends largely on the aspect ratio of the mushy layer and the viscosity contrast between the two domains. A preliminary estimate can be made to determine at which value of ξ the collapse-driven flow becomes dominant (i.e., $u/v \geq 1$) by estimating the order of magnitude for each term. Previously h was estimated to be $\sim 10^3$ m, while in the numerical models, $L \sim 10^6$ m. Combining these values together, it can be see that flow due to the collapse of the mushy layer becomes dominant when $\xi \leq\sim 10^{-6}$, in good agreement with the results. This implies that once the mushy layer becomes rheologically weak past a certain threshold, the positive feedback on the downwellings begins to dominate flows in the CMB region.

Figure 2.2 shows a clear negative trend between $\log_{10} G$ and $\log_{10} Ra$ that indicates a reduced enhancement of flow into the mushy layer with increasing convective strength of the mantle. In the calculations, the half-width at half the maximum amplitude of the layer was used to approximate the horizontal length scale L. From the numerical models, the mushy layer becomes smaller and narrower with increasing Ra. The following relations describing the dimensions of the mushy layer with Ra were obtained: $h \sim HRa^{-0.2325}$ and $L \sim HRa^{-0.1750}$ (Fig 2.3a and 2.3d). Plugging these values into Equation (2.21) shows that for a constant ξ, $G \sim Ra^{-0.1150}$. This exponent is similar, though slightly larger, than what is obtained in the numerical models (Fig. 2.2). The numerical models also show that a wider mushy layer seems to correlate with weaker collpase-driven flows (Fig. 2.3c).

The efficacy of the soft CMB mechanism as measured by G dominantly depends on the viscosity ratio ξ between the metal mush and the solid mantle. The viscosity of the mush mixture is expected to decrease as metal fraction increases and drops to values similar to liquid metal above the disaggregation limit (when grains are no longer forming a continuous skeletal touching network). However, the ability for metal to intrude into the pore spaces depends on the existence of a grain-touching network and therefore this limit is never reached under the present assumptions. The key factor is the decrease in mixture viscosity μ corresponding to the maximum infiltration capacity for the mush, at the point where it is no longer able to draw in additional metal. While a ξ of order 10^{-5} or smaller is certainly plausible in this scenario, the grain scale dynamics of this process and the effects on mixture viscosity are complex and difficult to constrain, even within several orders of magnitude.

The model presented here is relatively simple and is intended to introduce the basic idea of the soft CMB mechanism. The assumptions behind the hybrid model may break down as the liquid fraction approaches the disaggregation limit and/or the viscosity of the mushy layer becomes very low (on the same order of magnitude as the liquid metal) or the liquid fraction in the mushy layer is greater than or equal to the disaggregation limit. These can affect the model in two ways: (1) stresses from the gravitational collapse of the mushy layer become significant at the CMB, and (2) the Darcy velocity in the layer is unable to keep up

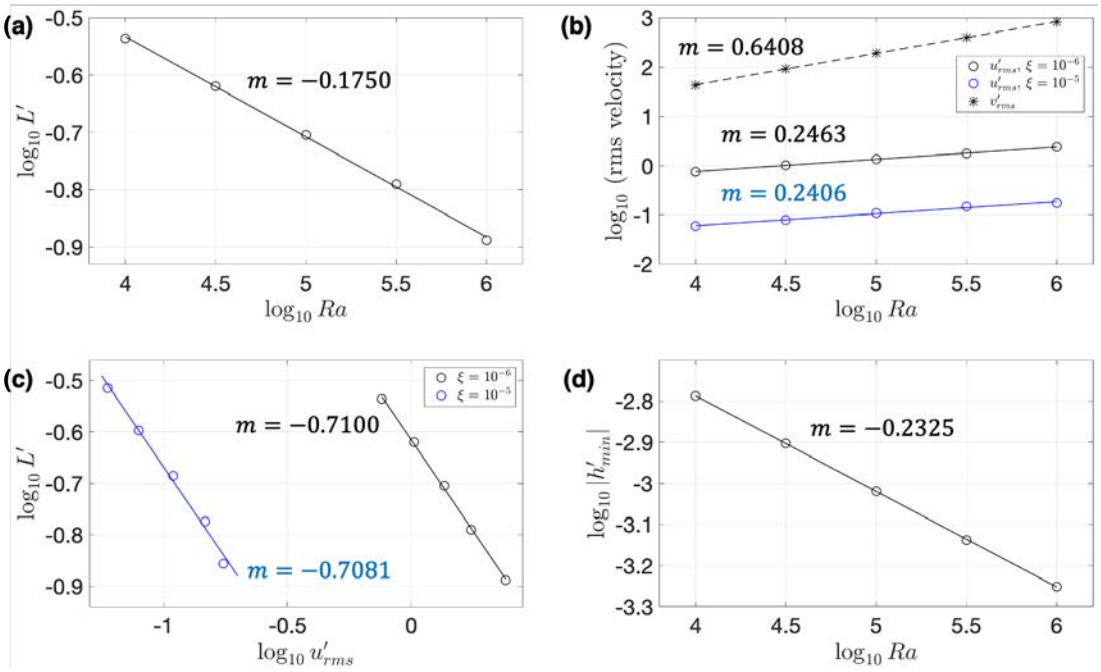

FIGURE 2.3: In the numerical calculations, the topographic depressions produced by buoyancy forces in the mantle are symmetric about the mid-point. L is used to quantify the value of the half width at half the minimum amplitude of the topography. Prime notation indicates nondimensional variables. (a) A plot of $\log_{10} L'$ against $\log_{10} Ra$ where $L' = L/H$. The results indicate that $L' \propto Ra^{-0.1750}$. (b) Plot of the logarithmic root-mean-square (rms) velocities against $\log_{10} Ra$. The velocities are multiplied with a normalization factor H/κ. The best-fit line for $\log_{10} v'_{rms}$ has a slope close to 2/3 which agrees with boundary layer theory. The slope of $\log_{10} u'_{rms}$ against $\log_{10} Ra$ is gentler and does not seems to vary significantly with different ξ. (c) Plot showing the relationship between the width of the topography with the collapse-driven flow. (d) Plot of maximum amplitude of dynamic topography with Ra. The amplitude is normalized by H.

with the rate of mantle material being replenished by downwellings. When the viscosity of the mushy layer is greatly reduced compared to the overlying mantle, secondary flows due to the gravitational collapse of the mushy layer can become comparable or even greater than large scale buoyancy-driven flows in the mantle, especially at the CMB. This implies that the vertical stresses creating dynamic topography will contain significant contributions from the collapse-driven component which was ignored in equation (2.3).

As mushy layer viscosity decreases below values considered in this study, the assumption of equation (2.7) may no longer be appropriate because upward liquid metal percolation needs to increase in proportion to the collapse-driven flow speed. The Darcy velocity of metal u_z^D may saturate at a maximum limiting value $u_{z,lim}^D$, and as a consequence liquid metal in the pore spaces will no longer be able to rise up quickly enough to match the downward flux of solid rock from above. In this situation it is expected that the top surface (i.e., $z = 0$) of the mushy layer will fall and the collapse-driven flow will weaken as the mushy layer becomes thinner. A new equilibrium may be reached if mantle downwelling decreases to

$|v_z| \approx |u^D_{z,lim}|$, in which case the mushy layer will assume a new thickness given by:

$$h_{lim} \approx \left(\frac{\Delta \rho g}{3 \mu L^2 u^D_{z,lim}} \right)^{1/4} \tag{2.22}$$

The details of the mushy layer dynamics at low viscosity and higher rates are likely to be more complex than considered here, and the scenario of a constant limiting Darcy velocity should be considered approximate.

Numerous other complications are expected to influence the efficacy of this mechanism. Variable viscosity, particularly temperature dependence, can have a strong influence on the lower boundary layer for mantle convection and needs to be considered in future studies. Furthermore, chemical reactions between rock and metal following exchange in a mush can change their densities and lead to enhanced convection and/or accumulation of layers on either side of the CMB, depending on whether reactions decrease or increase their densities. Finally, the long time evolution with these and other effects also needs to be studied in greater detail, rather than simply considering a snapshot.

Seismological detection of metal-rock mushy regions caused by dynamic topography alone is challenging owing to the small ($\sim$1 km) thickness expected in this scenario. The mushy layer itself is not straightforwardly compatible with other kinds of features in the CMB region such as ultralow-velocity zones (ULVZ) or large low shear velocity provinces (LLSVP), which are one and two orders of magnitude thicker (respectively) than features considered in this scenario (Hernlund & McNamara, 2015). Use of high frequency peaceful nuclear explosion data to profile the CMB has revealed a thin slow layer that is compatible with the kind of mushy layer considered here (Ross et al., 2004), although this interpretation is not unique.

In summary, the soft CMB mechanism, whereby chemical interaction in a metal-rock mushy layer induced by CMB dynamic topography is enhanced by gravitational collapse, appears to be a viable mechanism for increasing core-mantle chemical exchange. Further study of this mechanism may generate new predictions that can be tested against seismological and other observations. The possibility that hybrid processes like these, which are produced by collaboration of simpler processes occurring across a broad range of scales, additionally serves to illustrate the capacity for nature to find degrees of freedom that often escape our attention.

3 | The Hybrid Mechanism in a Variable Viscosity Mantle

3.1 Introduction

From the scaling law that was obtained in equation (2.21) of Chapter 2, the geometry of the dynamic topography at the CMB, and as such the mushy layer, shows that it exerts a strong influence on the enhancement of material fluxing into the dynamic topography. The CMB dynamic topography is important in geophysics as it has important implications on phenomena such as mechanical core-mantle coupling (e.g. Jault and Le Mouël, 1990; Hide et al., 1993; Asari et al., 2006), outer core stratification (e.g. Braginsky, 1999; Glane and Buffett, 2018), secular variations of the magnetic field (e.g. Bloxham and Gubbins, 1985; Kuang and Bloxham, 1997; Kuang and Chao, 2001), heterogeneities in the lower mantle (e.g. Yoshida, 2008; Lassak et al., 2010; Heyn et al., 2020), and variations in both the Earth's gravity field and geoid (e.g. Hager et al., 1985; Hager and Richards, 1989). Obtaining accurate measurements of CMB topography have been quite a challenge in seismology due to trade offs with mantle structures and, possibly, the outer core (Deschamps & Li, 2019). Nonetheless, several estimates have been obtained using a variety of methods (e.g. Morelli and Dziewonski, 1987; Sze and van der Hilst, 2003; Tanaka, 2010; Koelemeijer et al., 2012; Colombi et al., 2014; Schlaphorst et al., 2016) and a majority of these models show amplitudes on order of ~ 1 km.

It is well established that large-scale mantle flows can induce topography at the CMB and thus, properties in the deep mantle can have direct effects on the amplitudes. Since the properties important to mantle flow include viscosity, density and their distributions, the topography is also sensitive to the same properties and variations that can arise from temperature and compositional changes. Hence, it is possible for CMB topography to bring about some constraints on the structures in the deep mantle in conjunction with seismic data. While several numerical modelling studies have looked at how different compositions, rheology, and convective vigor of the mantle affects CMB topography in the context of LLSVPs and plumes in the lower mantle (Lassak et al., 2007; Lassak et al., 2010; Deschamps et al., 2018; Deschamps & Li, 2019; Heyn et al., 2020), not much work has been done

to define scaling laws for the CMB dynamic topography amplitude at the moment. Hence, this chapter has two main goals: (1) to look at how does the hybrid mechanism changes in a mantle with variable viscosity, and (2) to provide a preliminary scaling law for the CMB dynamic topography.

3.2 Numerical Model

In this chapter, the mantle will have a viscosity η that varies with temperature T that is given by:

$$\eta(T) = \eta_0 \exp\left(\frac{E}{RT} - \frac{E}{RT_0}\right) \tag{3.1}$$

where η_0 is the reference viscosity taken at the reference temperature T_0, E is the activation energy in kJ/mol and R is the molar gas constant. To quantify the strength of the temperature dependence, we introduce a new quantity β such that the viscosity becomes β times larger than the reference viscosity η_0 at temperature T_β i.e. $\eta(T_\beta) = \eta_0 \cdot \beta$. If this condition is plugged into equation (3.1), the following equation is obtained:

$$E' = \frac{\ln \beta}{\frac{1}{T_\beta} - \frac{1}{T_0}} \tag{3.2}$$

where $E' = E/R$. It is possible to re-express the viscosity with just T, β, and η_0 by plugging equation (3.2) into equation (3.1):

$$\eta(T) = \eta_0 \cdot \beta^{f(T)} \tag{3.3}$$

where

$$f(T) = \left(\frac{T_0 - T}{T}\right)\left(\frac{T_\beta}{T_0 - T_\beta}\right) \tag{3.4}$$

With η varying throughout the domain, the equation describing the conservation of momentum for $\vec{v}$ becomes

$$\nabla \cdot \left[\eta\left(\nabla\vec{v} + [\nabla\vec{v}]^{\mathbf{T}}\right)\right] - \nabla P_v = \rho_0[1 - \alpha(T - T_0)]g\hat{z} \tag{3.5}$$

where superscript $\mathbf{T}$ denotes transpose. Similarly, the equation describing the conservation of momentum for $\vec{u}$ is

$$\nabla \cdot \left[\eta\left(\nabla\vec{u} + [\nabla\vec{u}]^{\mathbf{T}}\right)\right] - \nabla P_u = \rho_0 g\hat{z} \tag{3.6}$$

The other equations such as the conservation of mass, gravitational collapse of the mushy layer, temperature advection-diffusion, and gain remain the same.

When viscosity begins to depend on temperature and the maximum viscosity contrast across the mantle becomes > 3000 (Solomatov, 1995), laboratory experiments (e.g. Booker and Stengel, 1978; Nataf and Richter, 1982; Richter et al., 1983; Davaille and Jaupart, 1993) and numerical models (e.g. Christensen, 1984; Ogawa et al., 1991; Moresi and Solomatov, 1995; Solomatov, 1995; Trompert and Hansen, 1998) have shown that a cold and

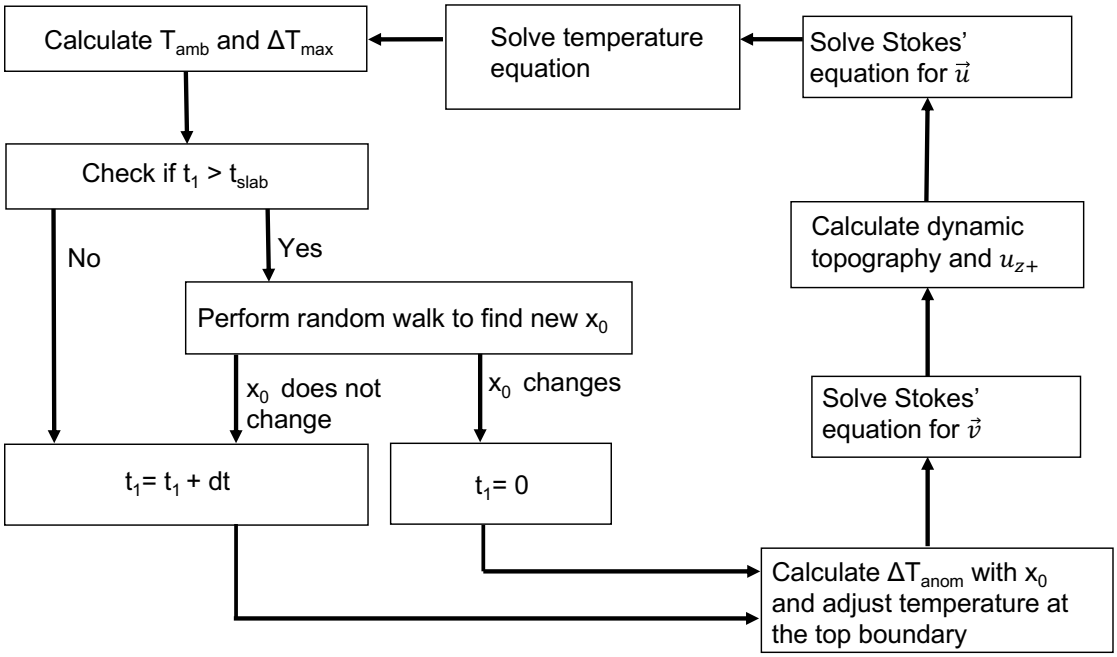

FIGURE 3.1: Flow chart of the computation that is carried out during one time step.

rigid stagnant lid forms at the surface that only transfers heat by conduction, while an active convecting layer is present underneath this lid. This convection regime is commonly referred to as the stagnant-lid regime where convection in the active layer is driven by a rheological temperature difference scale T_{rh} instead of the temperature drop across the entire fluid layer (e.g. Morris, 1982; Morris and Canright, 1984; Davaille and Jaupart, 1993; Moresi and Solomatov, 1995). For a fluid that is heated from the base, there will be two thermal boundary layers present, one at the bottom of the convecting region and the other below the stagnant lid. The upper thermal boundary layer exerts a stronger influence on the mantle thermal evolution (e.g. Schubert et al., 2001) and since only the dynamics of the deep mantle are of interest at the moment, the additional effects that can arise from the presence of the stagnant lid is removed by adjusting the boundary condition on top. This is accomplished by keeping the top boundary of the model permeable to flow and introducing a cold downwelling “slab" from the top. This boundary will be kept permeable to allow the “slab" and upwelling plumes to enter the and escape the domain respectively.

3.2.1 Boundary Conditions

The boundaries on the vertical sides of the model domain are set to be periodic, while the bottom boundary is kept at the reference temperature T_0 and free slip. The top boundary is insulating and permeable, but a Gaussian temperature anomaly ΔT_{anom} is imposed at the top of the domain. In a 2D Cartesian geometry, the equation is:

$$\Delta T_{\text{anom}}(x) = \begin{cases} -\Delta T_{\text{max}} \exp\left[-\frac{(x-x_0)^2}{2\sigma^2}\right] & , \quad |x - x_0| \leq w \\ 0 & , \quad |x - x_0| > w \end{cases} \tag{3.7}$$

Parameter	Value	Unit
ρ_r	5500	kg m^{-3}
ρ_m	9900	kg m^{-3}
ϕ	0.2	–
α	2.5×10^{-5}	K^{-1}
T_0	4000	K
T_β	3000	K
g	10	m s^{-2}
κ	10^{-6}	m^2 s^{-1}
σ	42466.1	m
w	100	km

TABLE 3.1: List of parameters that are kept constant in the numerical calculations.

where ΔT_{max} is the temperature difference between the ambient temperature at the top boundary T_{amb} and the coldest portion of the anomaly that is set at T_β (i.e. $\Delta T_{\text{max}} = T_{\text{amb}} - T_\beta$), x_0 is the position of the coldest portion of the anomaly, σ is the standard deviation of the Gaussian curve that also determines the half-width of the thermal anomaly, and w is the total width of the "slab". In the calculations, T_{amb} is obtained from the median temperature at the top of the domain and once $\Delta T_{\text{anom}}(x)$ is calculated, it is superimposed on to the horizontal temperature profile at the top.

To imitate the randomness of downwellings in the lowermost mantle, the location of the coldest portion of the downwelling x_0 is made to execute a random walk with a shift of δx in either the positive or negative x-direction with equal likelihood of staying or moving. However, the random walk is only performed once the total time elapsed from the previous walk exceeds a certain threshold t_{slab}. Figure 3.1 shows a flow chart of the structure of the code with the implementation of the temperature anomaly at the top boundary. The constants that are used in the numerical model are shown in Table 3.1.

3.3 Results

The equations of momentum conservation and temperature are discretised over a rectangular domain measuring 4000 km (width) by 1000 km (height) that is divided into 101$\times$51 grid points. The parameters varied during the calculations are η_0, β, and ξ with the range of values for each parameter shown in Table 3.2. Note that when $\beta = 1$, the mantle is essentially isovsicous. The velocity fields $\vec{v}$, $\vec{u}$ and pressure P_v, P_u from both buoyancy-driven and collapse-driven flows are obtained by solving the mass and momentum conservation equations (2.1, 2.2 , 2.12, and 2.13) iteratively using the SIMPLE method (Patankar, 2018).

For convection involving variable viscosity, the proper definition of the Rayleigh number can be somewhat arbitrary in comparison to isoviscous convection. In this study, two different definitions of Rayleigh number will be used, Ra_0 and $Ra_{\langle T \rangle}$, which are defined as follows

$$Ra_0 = \frac{\rho_r g \alpha \Delta T H^3}{\eta_0 \kappa} \tag{3.8}$$

Parameter	Value	Unit
β	1, 10, 100, 1000	–
η_0	10^{20}, 10^{21}, $10^{21.5}$, 10^{22}, $10^{22.5}$, 10^{23}	Pa s
ξ	10^{-6}, 10^{-5}	–

TABLE 3.2: List of parameters that are varied in the numerical calculations.

$$Ra_{\langle T \rangle} = \frac{\rho_r g \alpha \Delta T H^3}{\eta\left(T_{\text{rms}}\right)\kappa} \tag{3.9}$$

Ra_0 is the Rayleigh number that is calculated from the reference viscosity η_0 while $Ra_{\langle T \rangle}$ is calculated using viscosity that is defined from the root mean square temperature T_{rms}. The numerical calculations are run until a steady state is observed to have been reached by the models. The temperature field, viscosity field, mushy layer thickness and streamlines for both buoyancy-driven flow Ψ_v and flow due to the gravitational collapse of the mushy layer Ψ_u for $\eta_0 = 10^{21}$, $\beta = 100$ and $\xi = 10^{-6}$ are shown in Figures 3.2a, 3.2b, 3.2c, 3.2d, and 3.2e respectively. Similar to the results observed in the isoviscous study, the streamlines representing buoyancy-driven flows follow the typical convective pattern, whereas the streamlines representing collapse-driven flows show more than one smaller-scale circulation patterns interacting with the CMB (figure 3.2e). The arrows indicate that there is material flowing in and out of the mushy layer close to the base of the “slab". The viscosity plot in figure 3.2b shows the “slab" as a trail of high viscosity material on the left side of the domain that is coming from above. Comparing with the horizontal profile of the mushy layer in figure 3.2c, the maximum thickness corresponds to where the high viscosity material is thickest and closest to the CMB.

To calculate the G due to the collpase-driven flows, the mass fluxes associated with the different flows are computed and plugged into the same equation (2.19). Figure 3.3 shows G against $Ra_{\langle T \rangle}$ for all 48 cases and it can be seen that the factors that contribute to larger values of G (and thus flow enhancement) are lower $Ra_{\langle T \rangle}$, β and ξ values. The plots show that the dependence of G on $Ra_{\langle T \rangle}$ does not seem to change drastically with different ξ. In addition, only cases with low $Ra_{\langle T \rangle}$, $\xi = 10^{-6}$ and $\beta = 1$ seem to favour $G > 1$ (which indicates the mass flux into the mushy layer due to the gravitational collapse exceeds that of flows driven by large scale buoyancy forces in the mantle). It can also be seen that the effect of increasing β while keeping the other parameters constant reduces G, suggesting that stronger temperature dependence does not favour the enhancement of core-mantle interaction.

3.4 Discussion

To understand how variable viscosity affects the enhancement of downwellings, we can use the scaling equations (2.20) and (2.21) as a starting point. Equation (2.21) shows that G largely depend on three variables: h, L and ξ. Figure 3.4a and 3.4b show the plots of the nondimensionalised quantities h' and L' against $Ra_{\langle T \rangle}$ respectively, with H as the representative length scale. Both parameters show a decreasing trend with increasing

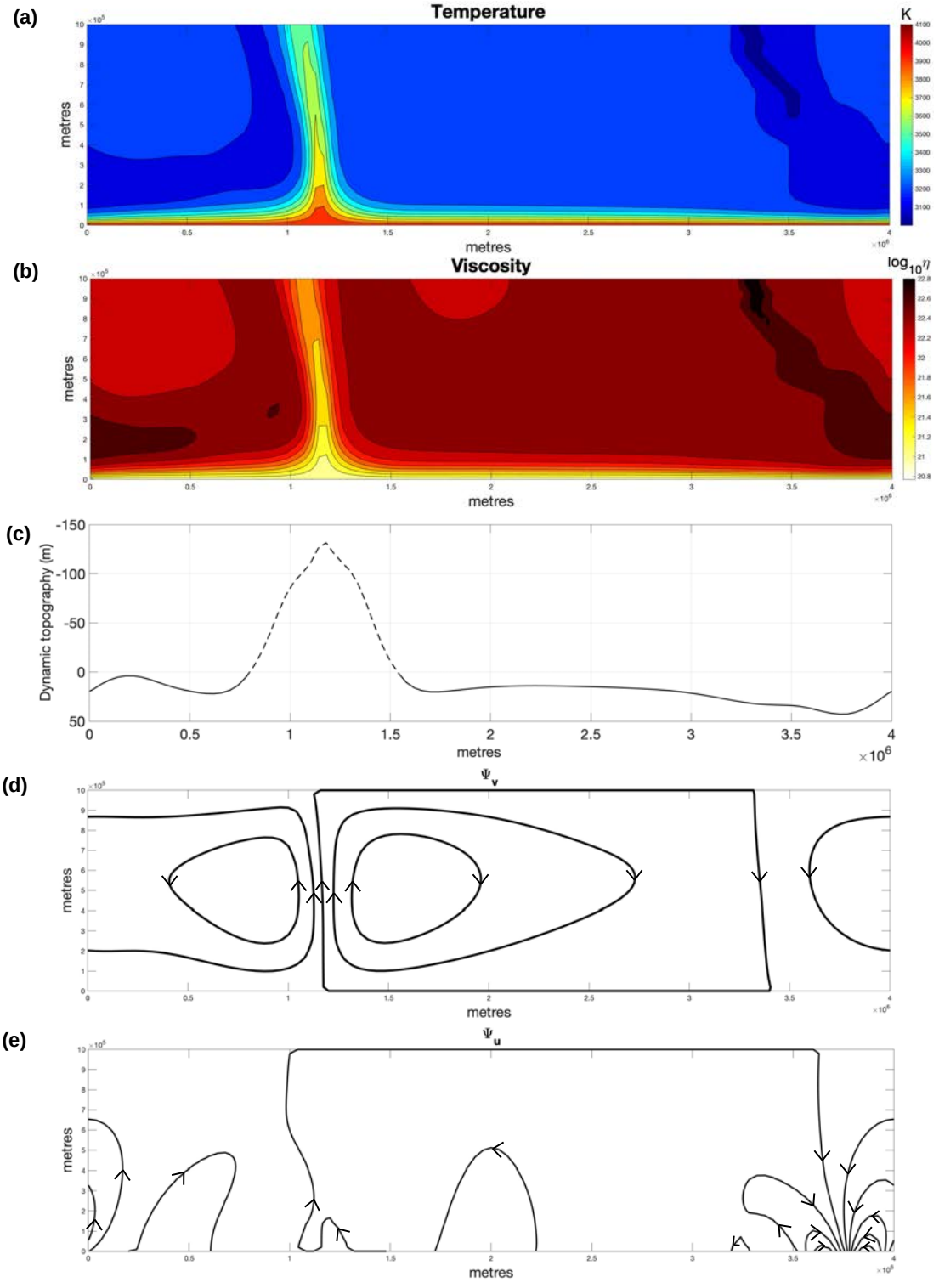

FIGURE 3.2: Results for $\eta_0 = 10^{21}$, $\beta = 100$, $\xi = 10^{-6}$. (a) Temperature field. (b) Viscosity field. (3) Horizontal profile of the dynamic topography induced by deviatoric stresses at the CMB. Solid lines and dashed lines indicate topography created by downwellings and upwellings respectively. Positive values indicate topography towards the core. (d) Streamlines of buoyancy-driven flow with black arrows indicating the direction of flow. (e) Streamlines of collpase-driven flow with black arrows indicating the direction of flow.

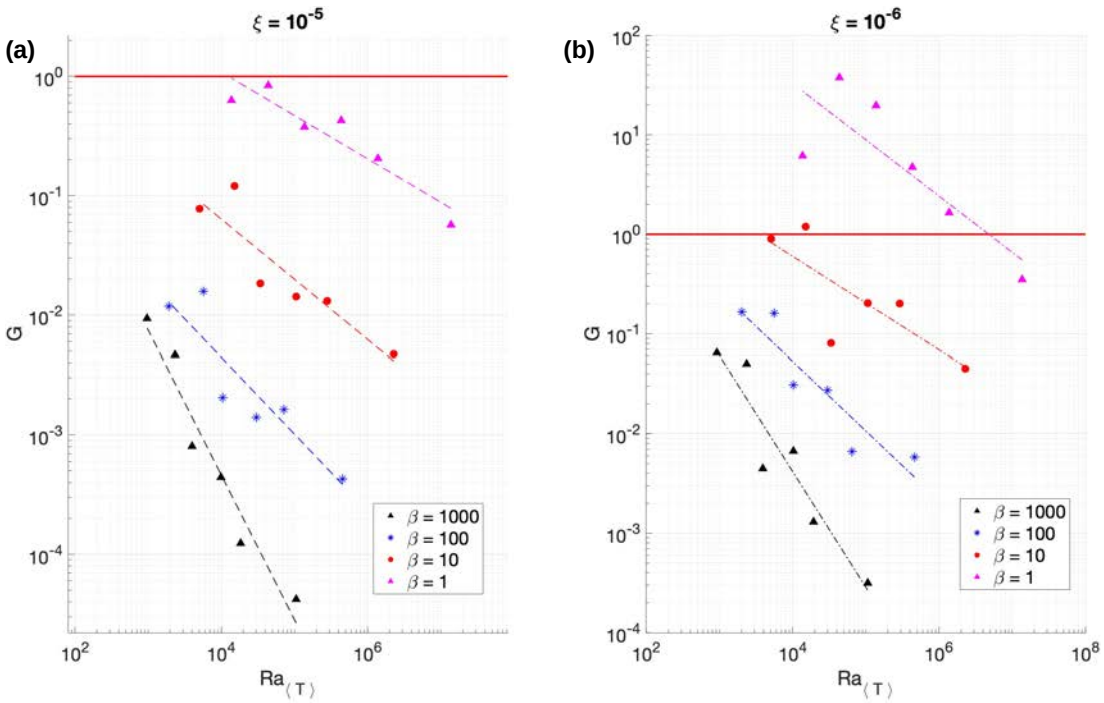

FIGURE 3.3: (a) Plot of G against $Ra_{\langle T \rangle}$ for $\xi = 10^{-5}$. Slopes of the black, blue, red and pink best fit lines are -1.2124, -0.6416, -0.5036 and -0.3635 respectively. (b) Similar plot for $\xi = 10^{-6}$. Slopes of the black, blue, red and pink best fit lines are -1.1635, -0.6975, -0.4686 and -0.5655 respectively. Red lines on both plots indicates where $G = 1$.

convective strength of the mantle, but figure 3.4a shows the effect for β much clearer where distinct trends can be identified. If the role of larger β values is to decrease the thickness of the mushy layer, equation (2.3) implies that stronger temperature dependence acts to decrease vertical stresses and thus, vertical strain at the CMB. This is clearly shown in figure 3.5 where a change in β by 3 orders of magnitude reduces $\partial v_z/\partial z$ by approximately an order of magnitude. This likely because increasing the temperature dependence of viscosity acts to increase the overall viscosity of the domain, as seen from figure 3.6a where the average viscosity normalised to η_0 increases with larger β, thus reducing the magnitude of the velocity gradients. This is despite the fact that the the viscosity of the downwelling "slabs" become significantly larger with increasing β, but since the coldest and most viscous portion of the "slab" takes a significantly longer time to travel towards the CMB, it would have gained sufficient heat from the ambient mantle in that time and reduced its viscosity (figure 3.7).

It is possible to characterise the magnitude of the local deviation of strain rates, independent of the coordinate system, in the domain by calculating the second invariant of the strain rate tensor $\dot{\varepsilon}_{II}$ that is defined as

$$\dot{\varepsilon}_{II} = \sqrt{\dot{\varepsilon}_{xx}^2 + \dot{\varepsilon}_{xz}^2} \tag{3.10}$$

where $\dot{\varepsilon}_{xx}$ and $\dot{\varepsilon}_{xz}$ are the normal strain rate and shear strain rate respectively. Figure 3.7 shows the temperature field and $\dot{\varepsilon}_{II}$ contour plots for a group of runs with $\eta_0 = 10^{21.5}$ and $\xi = 10^{-5}$. It is apparent in all the contour plots that the largest strain rates within the domain

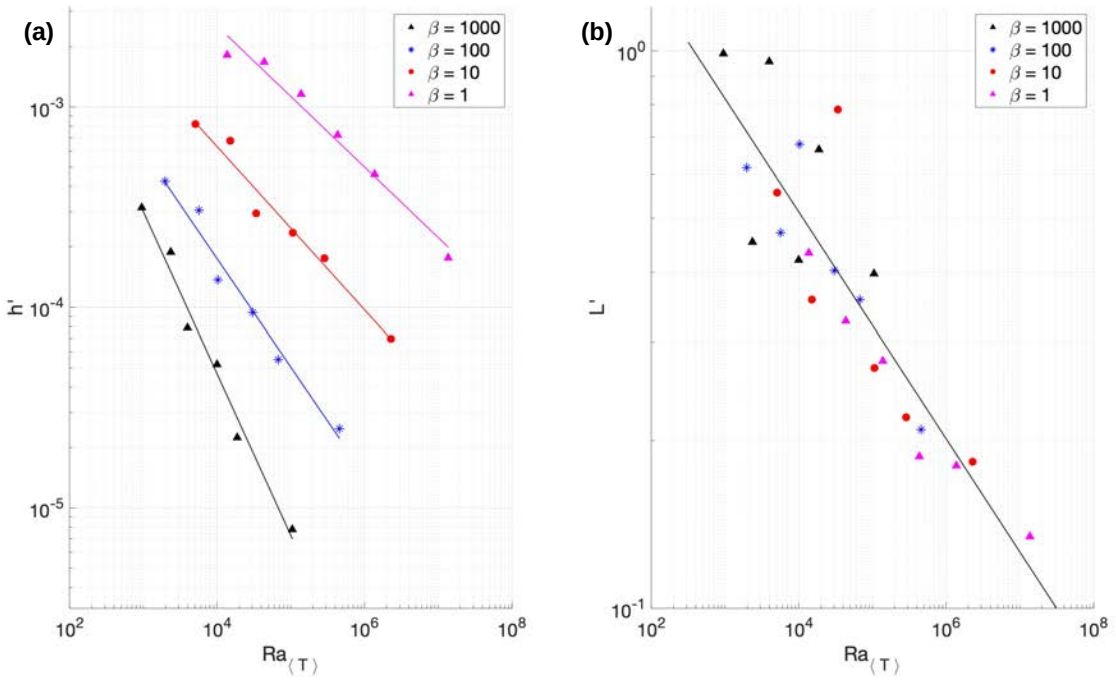

FIGURE 3.4: (a) Plot of h' against $Ra_{\langle T\rangle}$. The slopes of the pink, red, blue, and black lines are -0.3523, -0.4069, -0.5389, and -0.8061 respectively. (b) Plot of L' against $Ra_{\langle T\rangle}$. The width of the mushy layer does not seem to depend on β, but shows a decrease with $Ra_{\langle T\rangle}$. The slope of the best fit line in black is -0.2033.

are found close to where the hot upwellings are, whereas for downwellings the strain rates becomes much weaker relative to where the upwellings are. The plots also show that the lower boundary layer increases in thickness with larger β, which might also be contributing to the smaller strain rates at the CMB.

We can attempt to quantify the effect of β on the effect of flow enhancement at the CMB by looking at the scaling law and the parameters involved. In this case, the same numerical definition of L is used as in Chapter 2 where the full length at half maximum at the thickest portion of the mushy layer is the representative horizontal length. Figure 3.8 compares the calculated values with the estimations and they seem to be in rather good agreement, which shows that the scaling law is rather accurate at predicting G for both isoviscous and variable viscosity scenarios. However, figure 3.3 also shows G varying significantly with β which is not shown explicitly in the scaling equation. This might be because the β dependence is "hidden" in either h or L, or both at the same time. To identify what kind of dependence h and L have on β, a plot of h' and L' against $Ra_{\langle T\rangle}$ is shown in figure 3.4. h' and L' are the nondimesionalised versions of h and L respectively using height of the model domain H as the lengthscale. Figure 3.4a shows h' decreases in amplitude with increasing $Ra_{\langle T\rangle}$ and β implying that the thickness of the mushy layer decreases with increasing convection vigor and temperature dependence of viscosity. Meanwhile, figure 3.4b also shows L' generally decreasing with increasing $Ra_{\langle T\rangle}$ but no clear dependence can be seen with β. Hence, we shall assume for now that G depends on β only through h and attempt to express the relationship explicitly.

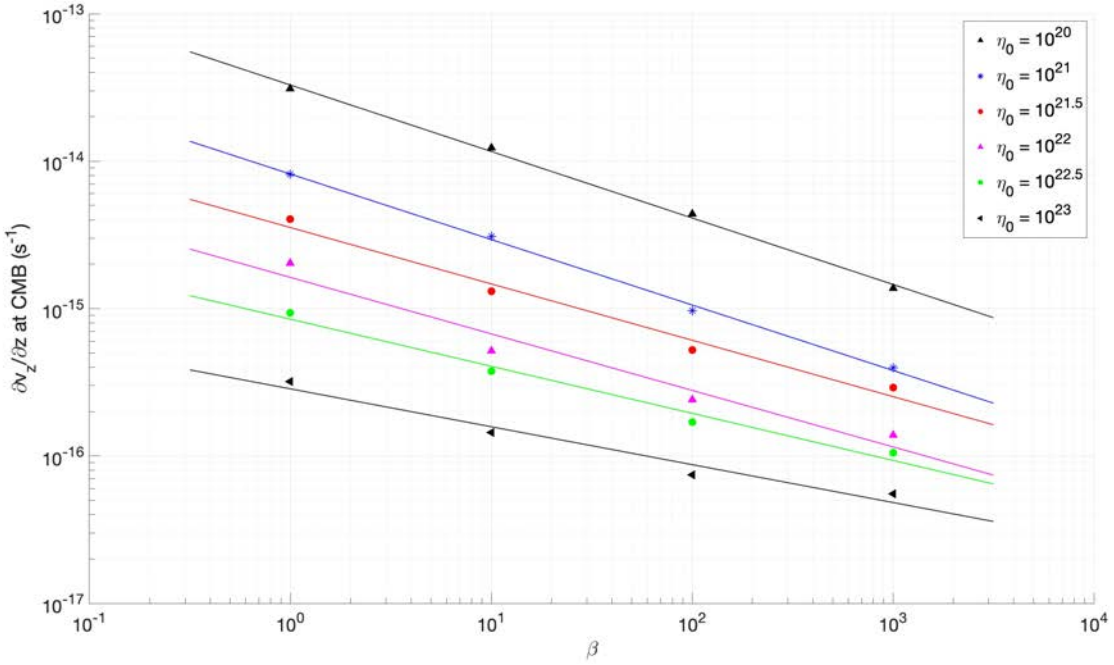

FIGURE 3.5: Plot of the vertical strain rate $\partial v_z / \partial z$ at the CMB against β for different η_0.

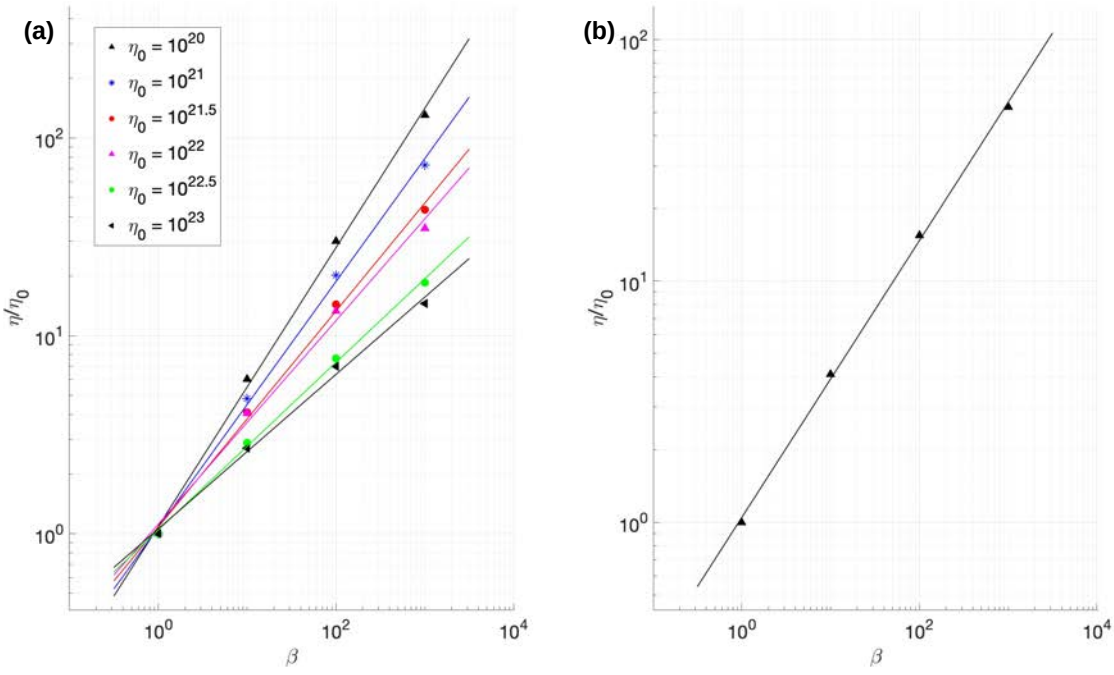

FIGURE 3.6: (a) Plot of normalised viscosity η / η_0 against β. The normalised viscosity increases with larger β, suggesting that increasing temperature dependence of viscosity increases the overall viscosity of the domain. (b) Points on the plot are average values that plot on the same β on the left graph. The slope of the best fit line in black is 0.5735.

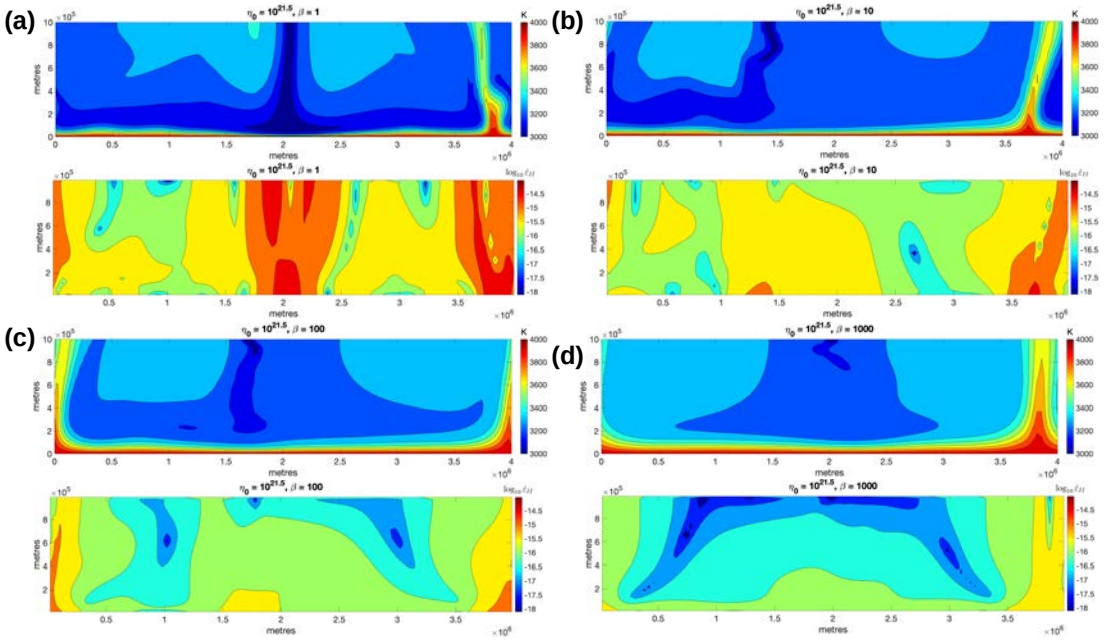

FIGURE 3.7: Plot of temperature field and second invariant of strain rate $\dot{\varepsilon}_{II}$ for $\eta_0 = 10^{21.5}$ and $\xi = 10^{-5}$. (a) $\beta = 1$, (b) $\beta = 10$, (c) $\beta = 100$, (d) $\beta = 1000$.

The equation for the the mushy layer thickness is given by equation (2.3) and if $\partial v_z/\partial z$ is assumed to scale as follows

$$\frac{\partial v_z}{\partial z} \sim \frac{\delta\rho g H}{\eta_0}, \tag{3.11}$$

This can be plugged into equation (2.3) to obtain a scaling for h such that

$$h \sim \frac{\delta\rho}{\Delta\rho} H \tag{3.12}$$

This scaling implies that h depends on the ratio of the buyoancy-induced density difference to the density jump between the core and mushy layer, and it does not depend on viscosity. Figure 3.4a shows that the latter is not true as h decreases with increasing Rayleigh number and because mantle viscosity is used as the control variable for convective vigor in the calculations, the data implies that h increases with increasing η. This suggests that either the scaling used in equation (3.11) is wrong or it is not applicable at the CMB and a different scaling should be used. Suppose that $v \sim \eta^{-m}$ where is a constant. The nondimenisonal scaling of v thus follows as

$$v' \sim \left(\frac{\delta\rho g H^3}{\eta\kappa}\right)^m \tag{3.13}$$

and if we let $v = v' \frac{\kappa}{H}$, the dimensional scaling for v will be

$$v \sim \left(\frac{\delta\rho g}{\eta}\right)^m \frac{H^{3m-1}}{\kappa^{m-1}} \tag{3.14}$$

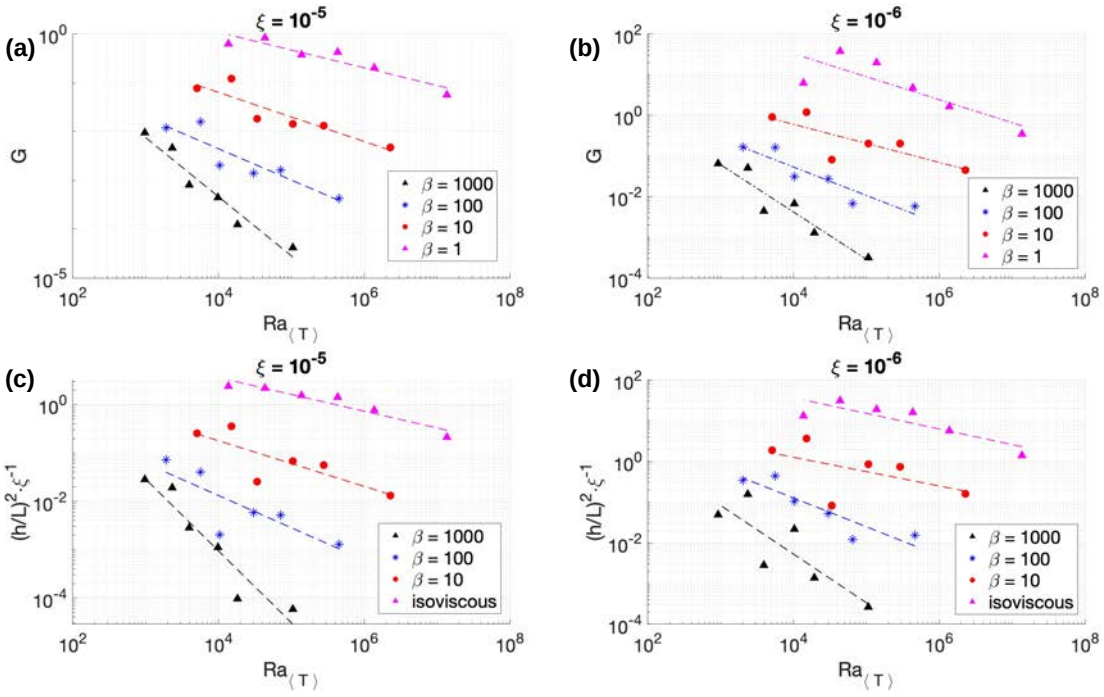

FIGURE 3.8: A comparison between G calculated from mass fluxes and estimations using the scaling law. (a) and (b) shows G calculated from mass fluxes using equation (2.19). (c) and (d) shows G estimated from the scaling law in equation (2.21).

and the vertical strain rate at the CMB is

$$\frac{\partial v}{\partial z} \sim \left(\frac{\delta\rho g}{\eta}\right)^m \frac{H^{3m-2}}{\kappa^{m-1}} \tag{3.15}$$

A scaling for h is then obtained by plugging equation (3.15) into equation (2.3)

$$h \sim \frac{(\delta\rho g)^m}{\Delta\rho g} \frac{H^{3m-2}}{\kappa^{m-1}} \frac{\eta_0}{\eta^m} \tag{3.16}$$

Considering the isoviscous case, this means $\eta = \eta_0$ and if equation (3.16) is divided by H, we get

$$h' \sim \frac{(\delta\rho g)^m H^{3m-3}}{\Delta\rho g \left(\eta_0 \kappa\right)^{m-1}} = \frac{\delta\rho}{\Delta\rho} Ra_0^{m-1} \tag{3.17}$$

From equation (3.17), it is possible to place some constraints on what values m can possibly take. Figure 3.4a shows that h' decreases with increasing Ra and thus $m - 1 < 0$. We also know that the flow velocities increase with convection vigor and thus from equation (3.13), we can conclude that m has to be positive. These combined constraints tell us that $0 < m < 1$.

According to boundary layer theory, m is calculated to be around 2/3 (e.g. Turcotte and Schubert, 2002). If this value is plugged into equation (3.17), this means that theoretically

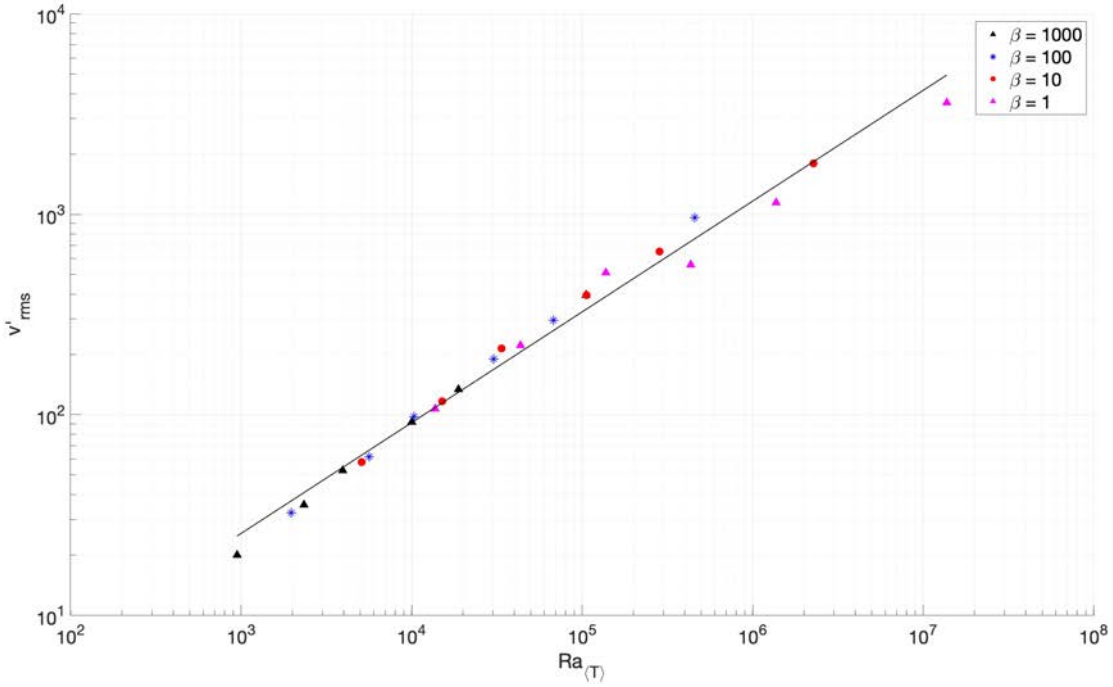

FIGURE 3.9: Plot of v'_{rms} against $Ra_{\langle T \rangle}$. Each data point is an average of runs with different ξ values but the same η_0 and β values. The black line shows the best-fit line through the data points with a slope of 0.5525.

h should go as $Ra_0^{-1/3}$ which agrees with numerical calculations that show dynamic topography decreasing with increasing convective strength. Figure 3.9 shows the nondimensionalised rms velocity of the buoyancy-driven flows from the numerical models. Interestingly, the plot shows that β does not have a significant effect on v. The slope of the best-fit line is calculated to be 0.5525 and if this value is taken to be m, according to equation (3.17) $h' \sim Ra_0^{-0.4475}$. This value is slightly larger in magnitude that the isoviscous slope in figure 3.4a. To account for the effects of temperature dependent viscosity, we can refer to equation (3.3) and presume that

$$\eta = \eta_0 \cdot \beta^q \tag{3.18}$$

where q is a constant to be determined and η is some average viscosity value that represents the whole domain. This can be plugged into equation (3.17) to get

$$h \sim \frac{(\delta\rho g)^m}{\Delta\rho g} \frac{H^{3m-2}}{(\eta_0 \kappa)^{m-1}} \beta^{-mq} \tag{3.19}$$

and after dividing both sides by H,

$$h' \sim \frac{\delta\rho}{\Delta\rho} Ra_0^{m-1} \beta^{-mq} \tag{3.20}$$

From equation (3.18), it can be seen that

$$\log_{10} \frac{\eta}{\eta_0} = q \log_{10} \beta \tag{3.21}$$

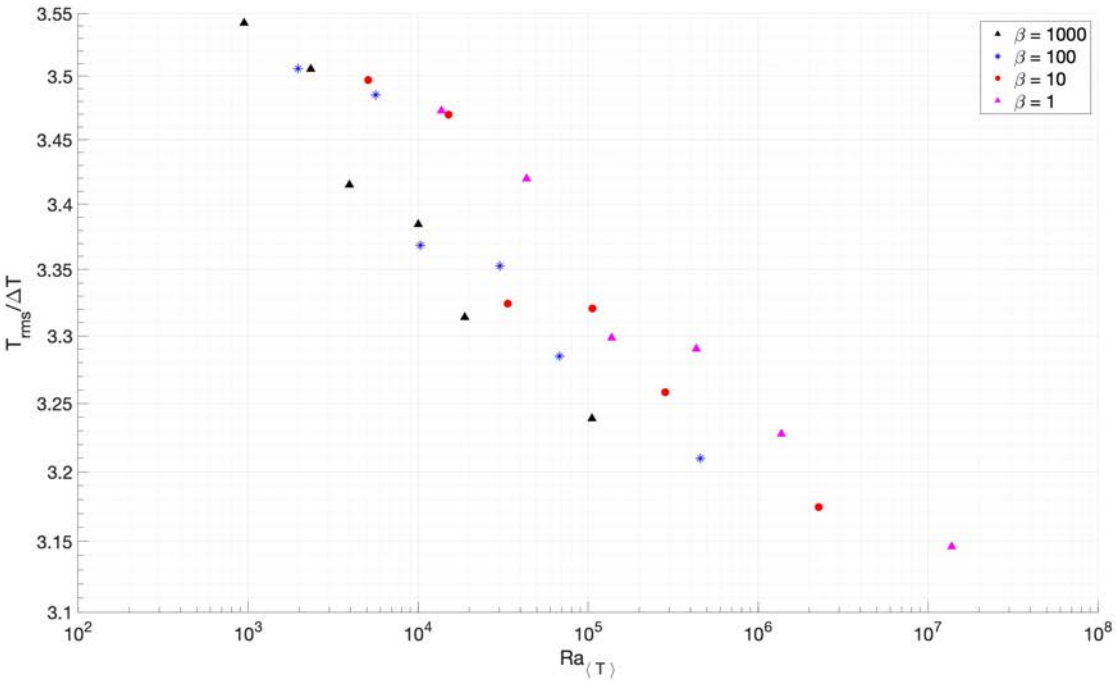

FIGURE 3.10: Plot of T_{rms} normalised with the maximum temperature difference across the domain ΔT against $Ra_{\langle T \rangle}$.

and by plotting $\log_{10} \eta/\eta_0$ against $\log_{10} \beta$, q can be obtained by measuring the slope of the best fit line. Theoretically, equation (3.21) shows once the mantle viscosity is normalised by the reference viscosity, they should all converge on the same value for the same β. This plot is shown in figure 3.6a where η is obtained from using the rms temperature T_{rms} of the entire domain. Contrary to the theoretical predictions, the plot shows the normalised viscosity diverging with increasing β. This might be because for q to be constant, it would imply that T_{rms} is constant regardless of η/η_0 which is not true as T_{rms} depends on η_0. This is further evidenced by figure 3.10 where the average temperature in the domain seems to drop with increasing convection vigor which is controlled by viscosity. However, figure 3.6a shows that increasing β generally increases η/η_0 and for the sake of argument, we presume that q can be calculated by taking the average value of each group of β points and calculating the slope from this average. The result is shown in figure 3.6b and the slope gives $q = 0.5735$. Now with $m = 0.5525$, the scaling law for h' which takes into account temperature dependent viscosity is

$$h' \sim \frac{\delta\rho}{\Delta\rho} Ra_0^{-0.4475} \beta^{-0.3169} \tag{3.22}$$

Equation (3.22) can be converted to the dimensional form by multiplying both sides by H and if the result is substituted back into equation (2.20), a new scaling for G with Ra is obtained

$$G \sim \left(\frac{\delta\rho}{\Delta\rho}\frac{H}{L}\right)^2 \left(\frac{1}{\xi}\right) \cdot Ra_0^{-0.8950} \cdot \beta^{-0.6338} \tag{3.23}$$

It has to be noted that this is still not the true scaling relation as figure 3.4b shows that

L decreases with increasing Rayleigh number. The best fit line gives the following scaling relation for the horizontal length scale of the mushy layer: $L/H \sim (Ra_0 \cdot \beta)^{-0.2033}$ and suppose this is somewhat true, plugging this back into equation (3.23) gives us the actual scaling of G with Ra_0 and β:

$$G \sim \left(\frac{\delta\rho}{\Delta\rho}\right)^2 \left(\frac{1}{\xi}\right) \cdot Ra_0^{-1.3016} \cdot \beta^{-1.0404} \tag{3.24}$$

Comparing with figure 3.3 however, we see that the scaling law predicts a much stronger relationship with Rayleigh number.

One reason for the uncertainty of L in the results of this study is because of the purposeful removal of the top boundary layer from the models. Although this gets rid of the influence of the stagnant lid from the dynamics, the self-consistency of the downwelling “slab" is affected as well which is why the downwelling is actively imposed in the models. Hence, the width of this downwelling is also a parameter that could be varied that has a direct influence on the CMB dynamic topography and L too. Future studies might be required to take into account this parameter as well.

When considering the implications of these results on Earth, since more vigorous convection reduces core-mantle interaction via the “soft CMB” mechanism, flows driven by the gravitational collapse of mushy layer is most likely to have been very weak during the early Earth when temperatures in the mantle were much higher, resulting in lower viscosities and thus high convective vigour (e.g. Karki and Stixrude, 2010; Solomatov, 2015). Hence, it is only very likely that once the mantle begins to further cool and viscosity in the lower mantle starts to increase, the “soft CMB” mechanism will begin to become more effective since larger amounts of stresses can be supported in the mantle to create larger amplitudes of CMB dynamic topography. Another point of consideration is that during the crystallisation of the magma ocean in the early Earth, residual melts in the basal magma ocean will be enriched in incompatible elements and further cooling will lead to fractional crystallisation of increasingly Fe-enriched solids (Labrosse et al., 2007). These can be deposited on the mantle side of the CMB and create dense melts which might exert their own influence on the CMB topography.

Lastly, one of the most difficult parameters to constrain in the model is the rheology of the lower mantle. To begin with, obtaining a realistic value for β is rather challenging, and it might be even possible for the activation energy E to vary with depth (e.g. Karato, 2008; Matyska et al., 2011). In this study, the lower mantle is assumed to be a Newtonian fluid, but experimental studies have suggested that at regions with high strain rates, the viscosity will be largely dominated by ferropericlase because it is rheogologically the weakest lower mantle phase (Yamazaki & Karato, 2001). This increases the likelihood of forming an interconnected network of weak layers (Yamazaki et al., 2009; Thielmann et al., 2020) which might result in a lower mantle with strain dependent rheology. The weakened layers will create regions of localised strain and potentially decouple the lower boundary layer from the lower mantle, thereby reducing the dynamic topography further.

3.5 Summary

This chapter builds on the preceding chapter by investigating the effects of the “soft CMB" mechanism on mantle convection where viscosity is temperature dependent. The main aim is to understand how this change in rheology affects the enhancement of downwelling flows in the lower mantle and to derive a preliminary scaling law for the CMB dynamic topography. Using numerical models, the results have shown that increasing the strength of temperature dependent viscosity reduces the dynamic topography and collapse-driven flows, which means the efficacy of the “soft CMB" mechanism is reduced as well. The final scaling law that was derived indicates that the CMB dynamic topography depends on three parameters: (1) the ratio of the density difference due to buoyancy effects $\delta\rho$ in the mantle to the density contrast between the outer core and mushy layer $\Delta\rho$, (2) the Rayleigh number, and (3) the strength of temperature dependent viscosity in the mantle, of which increasing the latter two reduces the topography. Despite the unconstrained rheology of the real mantle, the basic models here serve to build an intuition of the mechanism so that an understanding of different processes occurring can be slowly developed with increasing complexity. The next chapter will add on another layer of complexity by considering the effects of composition on the mechanism.

4 | Tracking Composition

4.1 Introduction

After examining the “soft CMB" mechanism operating under different mantle rheologies, understanding the behaviour of chemically distinct material that emerge from the mushy layer is equally important as well. Up until now, chemical variations have been neglected in the numerical models but since it is an important aspect in corroborating with geochemical evidence, this chapter aims to introduce a basic thermochemical model where chemical variations can give rise to buoyancy forces as well.

Modelling thermal convection for a mantle with heterogeneous composition has been of great interest as it provides valuable insights into chemical and thermochemical anomalies that potentially reside in the lower mantle (e.g. Lenardic and Kaula, 1993; Tackley, 1998; Davaille, 1999a; Kellogg et al., 1999; Zhong, 2006; Lassak et al., 2007). Several techniques have been developed to represent compositional fields as accurately as possible. This is largely because compositional diffusivity in the mantle is assumed to be negligible and as a result, numerical methods that are implemented have to reduce numerical diffusion as much as possible to ensure accurate results from long time integrations. Numerical methods that have been used include: continuum field techniques (e.g. Ten et al., 1997; Ogawa, 2000), marker chain method (e.g. Christensen and Yuen, 1985; Van Keken et al., 1997; Zhong and Hager, 2003), and particle tracer methods (e.g. Weinberg and Schmeling, 1992; Gerya and Yuen, 2003; Tackley and King, 2003; McNamara and Zhong, 2004), most of which have been reviewed by Van Keken et al. (1997). In this study, tracer particles will be used to track the composition of the chemically reacted material. The reacted material can represent a whole host of unique isotope ratios such as the high ^{3}He/^{4}He ratios, low μ^{182}W, noble gases like Ne or even FeO-rich material. In addition, depending on the degree of chemical disequilibrium, P-T conditions and the chemical species involved in the chemical reaction, the buoyancy of the reacted rock can be negative, positive or neutral compared to the ambient material at the lower mantle. For instance, the following equation proposed by Knittle and Jeanloz (1991) transfers Fe from perovskite (Pv) to metal (M):

$$(\mathrm{Mg,Fe})\mathrm{SiO_3}^{\mathrm{Pv}} + \mathrm{Fe}^{\mathrm{M}} \longrightarrow \mathrm{FeO}^{\mathrm{M}} + \mathrm{FeSi}^{\mathrm{M}} + \mathrm{MgSiO_3}^{\mathrm{Pv}} \tag{4.1}$$

Since the Fe component is removed from the silicate, this potentially creates a positively buoyant perovskite product. However, it is also possible to have reactions that create a negatively buoyant silicate product through the addition of Fe from the core. One potential reaction could be the exchange of Si and Fe as such (Ricolleau et al., 2011):

$$\mathrm{SiO_2}^{\mathrm{Sil}} + 2\,\mathrm{Fe}^{\mathrm{M}} \rightleftharpoons \mathrm{Si}^{\mathrm{M}} + 2\,\mathrm{FeO}^{\mathrm{Sil}} \tag{4.2}$$

where Sil refers to the silicate and the forward reaction increases the Fe content of the silicate. Similarly, it is also possible for Fe and O to be transferred between the core and ferropericlase (Fp) as follows (e.g. Frost et al., 2010):

$$\mathrm{Fe}^{\mathrm{M}} + \mathrm{O}^{\mathrm{M}} \rightleftharpoons \mathrm{FeO}^{\mathrm{Fp}} \tag{4.3}$$

to create a Fe-enriched ferropericalse. Similar to how ULVZs might be iron-enriched domains (e.g. Knittle, 1998; McNamara and Zhong, 2004; Muir and Brodholt, 2020), increasing the Fe content of the silicates in the lower mantle will increase the overall density of the rock. Finally, if there is no exchange in major elements between the silicate and metal and instead just the trace elements, we can expect for the reacted rock to have a neutral buoyancy.

4.2 Method

With the inclusion of a compositional field, the mass conservation equation (eq. 2.2) for buoyancy-driven flows $\vec{v}$ does not change, but the momentum conservation equation now becomes:

$$\nabla \cdot \left[\eta \left(\nabla \vec{v} + [\nabla \vec{v}]^{\mathbf{T}}\right)\right] - \nabla P_v = \rho_0[1 - \alpha(T - T_0) + \gamma C]g\hat{z} \tag{4.4}$$

where C is composition and γ is the expansion coefficient due to composition effects. With two scalar fields that are subject to advection, an additional equation similar to equation (2.14) is required to describe the evolution C:

$$\frac{\partial C}{\partial t} + \vec{v}_{\mathrm{eff}} \cdot \nabla C = 0 \tag{4.5}$$

From equation (4.4), it can be seen that if $\gamma > 0$, any chemical stratification that occur will be stabilised by the density difference while thermal density differences does the opposite by destabilising the stratification. The competition between these two buoyancy forces can be characterised using a nondimensional number known as the chemical buoyancy ratio B (e.g. Hansen and Yuen, 1988; Davaille, 1999a):

$$B = \frac{\gamma \Delta C}{\alpha \Delta T} \tag{4.6}$$

where ΔC is the maximum compositional difference in the domain. The boundary conditions in this model are identical to the variable viscosity model in Chapter 3 i.e. horizontally periodic, permeable on top, free-slip and isothermal at the bottom.

Parameter	Value	Unit
β	$1, 10$	–
η_0	$10^{22}, 10^{22.5}, 10^{23}$	Pa s
ξ	$10^{-6}, 10^{-5}$	–
γ	$1.1, 0, -0.25$	–

TABLE 4.1: List of parameters that are varied in the numerical calculations for thermo-chemical convection.

4.2.1 Tracer Advection

The tracers are advected using a 4th order Runga-Kutta scheme. To ensure that no artificial local convergence or divergence of tracers and that the continuity equation is well respected at all times, a continuity-based higher order velocity interpolation scheme is adopted (e.g. Jenny et al., 2001; Meyer and Jenny, 2004; Pusok et al., 2017; Gerya, 2019). Since the top boundary is permeable, any tracer that is advected out of the domain, regardless of its composition, will be artificially moved to a downwelling zone on top of the domain with an ambient mantle composition to ensure that no tracers are lost during the time integration. This means that if any material is advected out of the domain via upwellings, they are assumed to proceed to the shallower mantle and thus to balance this loss of material, “fresh" ambient mantle material will replenish the model at downwellings. Similarly, the bottom boundary is only permeable at where the mushy layer is present. Hence, any tracer that is advected into the mushy layer will have its composition changed, while also artificially moved back into the domain close to the CMB but away from the mushy layer. This is to ensure that additional complications that may arise from the effects of compositional density difference on the dynamic topography are avoided. Although the artificial placement of tracers back into the domain is rather crude, it ensures that no tracers are lost during the numerical simulations.

4.2.2 Obtaining C from Tracer Distributions

With the compositional field C now needed, in addition to T, to compute the velocity and pressure fields associated with the buoyancy-driven flows, the composition of every tracer has to be interpolated to the appropriate grid points. In this model, C is defined at the centre of the cells just like T and P_v. To calculate C, the ratio method is adopted (Tackley & King, 2003), where in a given cell measuring δx by δz, C is proportional to the ratio of chemically altered tracers to the total number of tracers in the cell:

$$C_i = \frac{X_i^{\text{diff}}}{X_i^{\text{diff}} + X_i^{\text{same}}} \tag{4.7}$$

X_i^{diff} and X_i^{same} are the number of chemically altered tracers and non-chemically altered tracers respectively inside cell i. This ensures that $0 \leq C \leq 1$ and hence, $\Delta C = 1$ in equation (4.6).

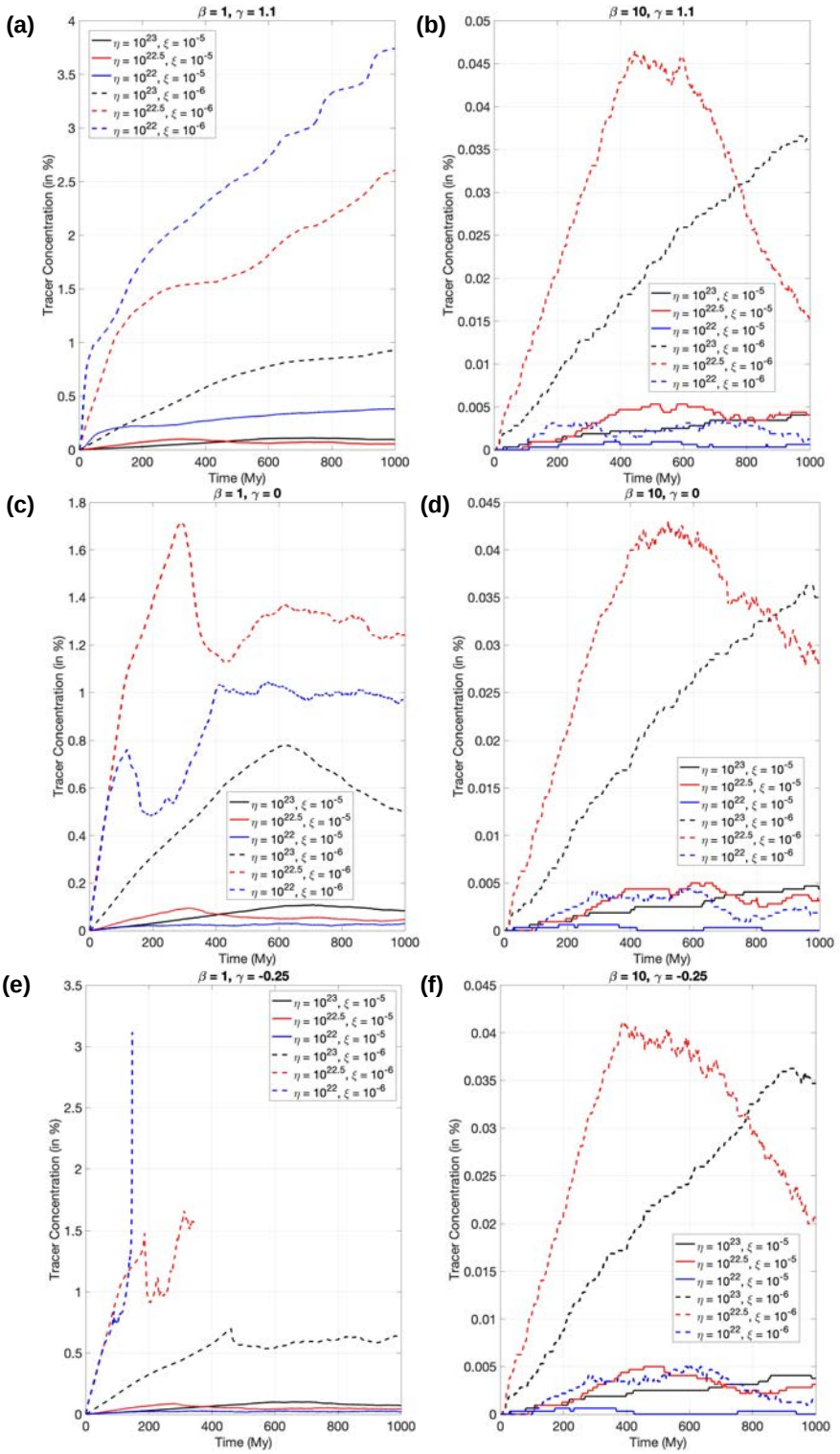

FIGURE 4.1: Plots of tracer concentration evolution through time until 1 Gyr grouped according the pairs of β and γ values. β determines the strength of temperature-dependent viscosity while γ is the expansion coefficient due to composition effects.

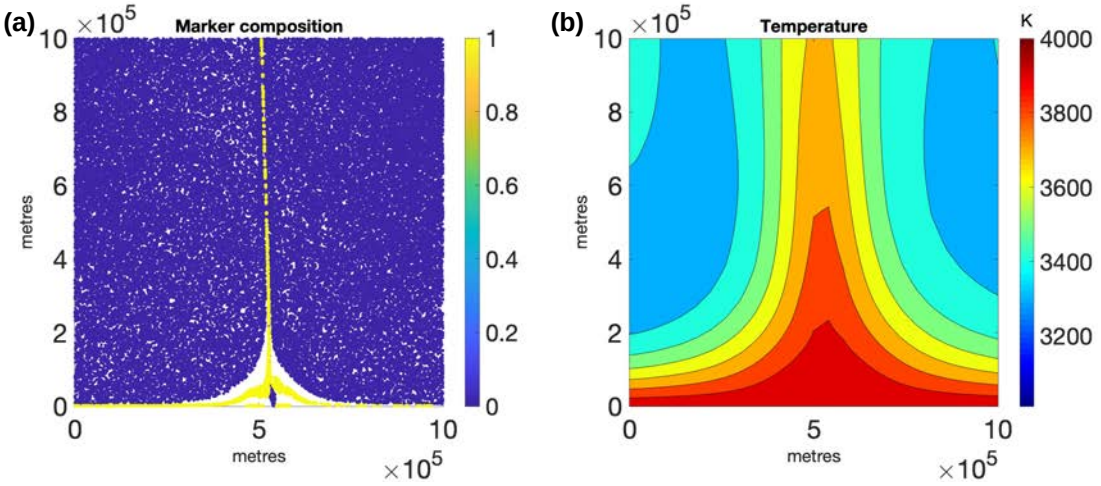

FIGURE 4.2: (a) Distribution of tracers and (b) temperature field around the upwelling plume for the case where $\eta_0 = 10^{23}$, $\beta = 1$, $\xi = 10^{-6}$, and $\gamma = 1.1$. Yellow tracers represent the chemically altered material while blue tracers represent ambient mantle material. The chemcially alter tracers are shown to leave the domain via plume entrainment.

4.3 Results

Numerical calculations for thermochemical mantle convection were performed in both isoviscous and temperature dependent viscosity domains for the parameters shown in Table 4.1. The equations of momentum conservation and temperature are discretised over a rectangular domain measuring 4000 km (width) by 1000 km (height) that is divided into 101×51 grid points. Meanwhile, the boundary conditions are kept the same as what has been described in Chapter 3. The parameters that are kept constant in the calculations are the same as those listed in Table 3.1. The value if γ determines the strength of the chemical buoyancy, and whether it enhances or counteracts the thermally-induced buoyancy in the system. A total of three γ values - 1.1, 0, and -0.25 - are tested in this model to investigate the effects of negative, neutral and positive chemical buoyancy respectively. Although $\gamma = 1.1$ is rather large, it approximates the expected density anomaly of ULVZs (Rost et al., 2006). The different values of γ enables us to study how different buoyancy effects of the reacted rock the study of the entrainment characteristics of the plume as well as the change in concentration of the reacted material in the modelling domain. The total number of tracers in the numerical modelling domain is 3.2×10^5.

The numerical calculations were run until 1 Gyr and figure 4.1 shows the evolution of tracer concentration in the domain for both isoviscous and temperature dependent viscosity models. It can be seen from figure 4.1a, c, and e that for cases with smaller ξ values, the concentration of chemically distinct tracers tends to become larger over a given time period for an isoviscous lower mantle. However, the trend is not as clear in figure 4.1b, d, and f where the tracer concentrations for variable viscosity cases are depicted. In the case of an isoviscous mantle with positive chemical buoyancy (fig 4.1), the numerical models with lower reference viscosities ($\eta_0 = 10^{22}, 10^{22.5}$) become increasingly difficult to proceed in time as

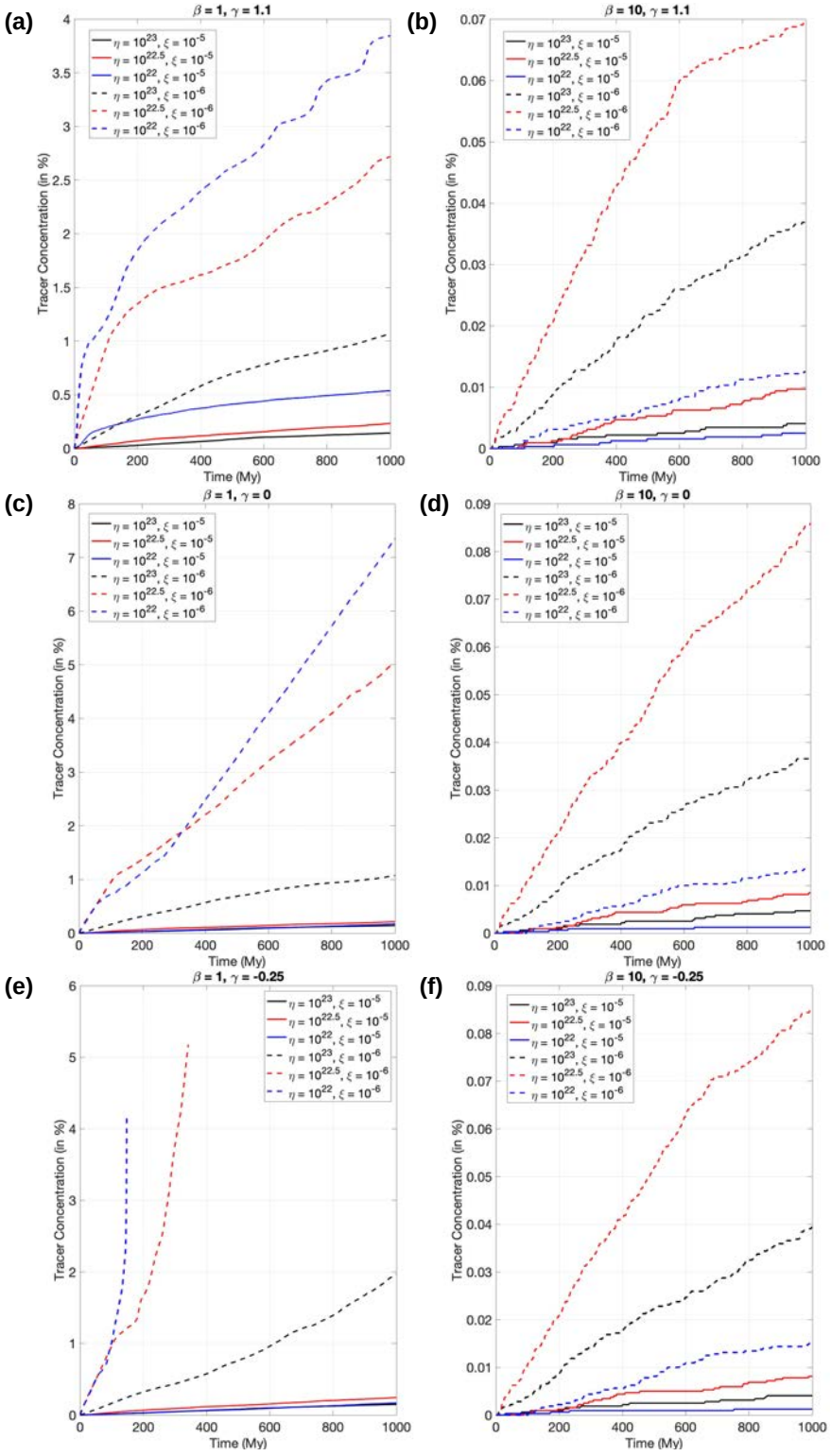

FIGURE 4.3: Plots of the cumulative amount of chemically distinct tracers expressed as a percentage of the total number of tracers in the modelling domain. Models with smaller ξ values (dashed lines) process more tracers through the mushy layer than those with larger ξ values (solid lines), agreeing with previous isochemical modelling results.

the accumulation of positively buoyant material at the CMB amplifies the instabilities arising from temperature deviations. The concentration curve for a number of cases show a peak in concentration followed by a dip (e.g. fig 4.1b, c, d, f). This is because on top of the addition of tracers that emerge from the mushy layer, the tracer concentration is also affected by tracers leaving the domain via the permeable boundary above. This has the overall effect of reducing the tracer concentration within the domain. Since the tracers can only leave the domain through plume entrainment, an example of this is illustrated in figure 4.2a where yellow particles represent the chemically distinct tracers that have reacted with the core fluid in the mushy layer. The yellow particles are observed to have accumulated in a specific region, followed by a trail that reaches the top of the modelling domain. When compared with the temperature field in the same region (figure 4.2b), we see an upwelling plume at exactly where the chemically distinct material are accumulating and the plume of compositionally distinct material is much thinner than the thermal plume. This shows that a portion of such tracers are being entrained out of the modelling domain via the plume. Therefore, to accurately gauge the degree of material exchange between the core and mantle via the mushy layer, looking at the cumulative number of chemically distinct tracers over time is a more reliable indicator instead.

Figure 4.3 shows the cumulative amount of chemically distinct tracers expressed as a percentage of the total number of tracers in the domain over time. The figure shows that the isoviscous cases produce more chemically distinct tracers than the variable viscosity ones, agreeing with the results obtained from previous isochemical studies (figure 3.3). Moreover, lower ξ values have a higher cumulative number which is expected based on previous studies as well. On the contrary, the effect of different reference viscosity is somewhat different from what is expected, and this might be because the models have not reached a steady state yet.

Figures 4.1 and 4.3 show that tracers leaving the domain via upwellings can significantly change the concentration present in the domain at any given time. Indeed, figure 4.4 shows the cumulative amount of chemically distinct tracers entrained out of the domain, expressed as a percentage of the total number of tracers in the domain over time, and it can be seen that the for the same η_0 and β values, tracers leave the domain earlier if ξ is smaller. Furthermore, figure 4.4a shows that for some models, the rate of chemically distinct tracers leaving can change significantly. For the case where $\eta_0 = 10^{22}$, $\beta = 1$, $\xi = 10^{-6}$, $\gamma = 1.1$, it can be seen that this rate is initially fast, but soon becomes zero after ~ 350 Myrs, indicating that the amount of chemically distinct tracers leaving the domain is close to zero. This suggests that these tracers are actually accumulating in the domain instead and the consequences will be discussed in the following section. Figure 4.4 also seems to show that with decreasing γ, both the rate at which the chemically distinct tracers leave the domain and total cumulative amount increase as well. This is quite apparent when comparing the results of the isoviscous cases.

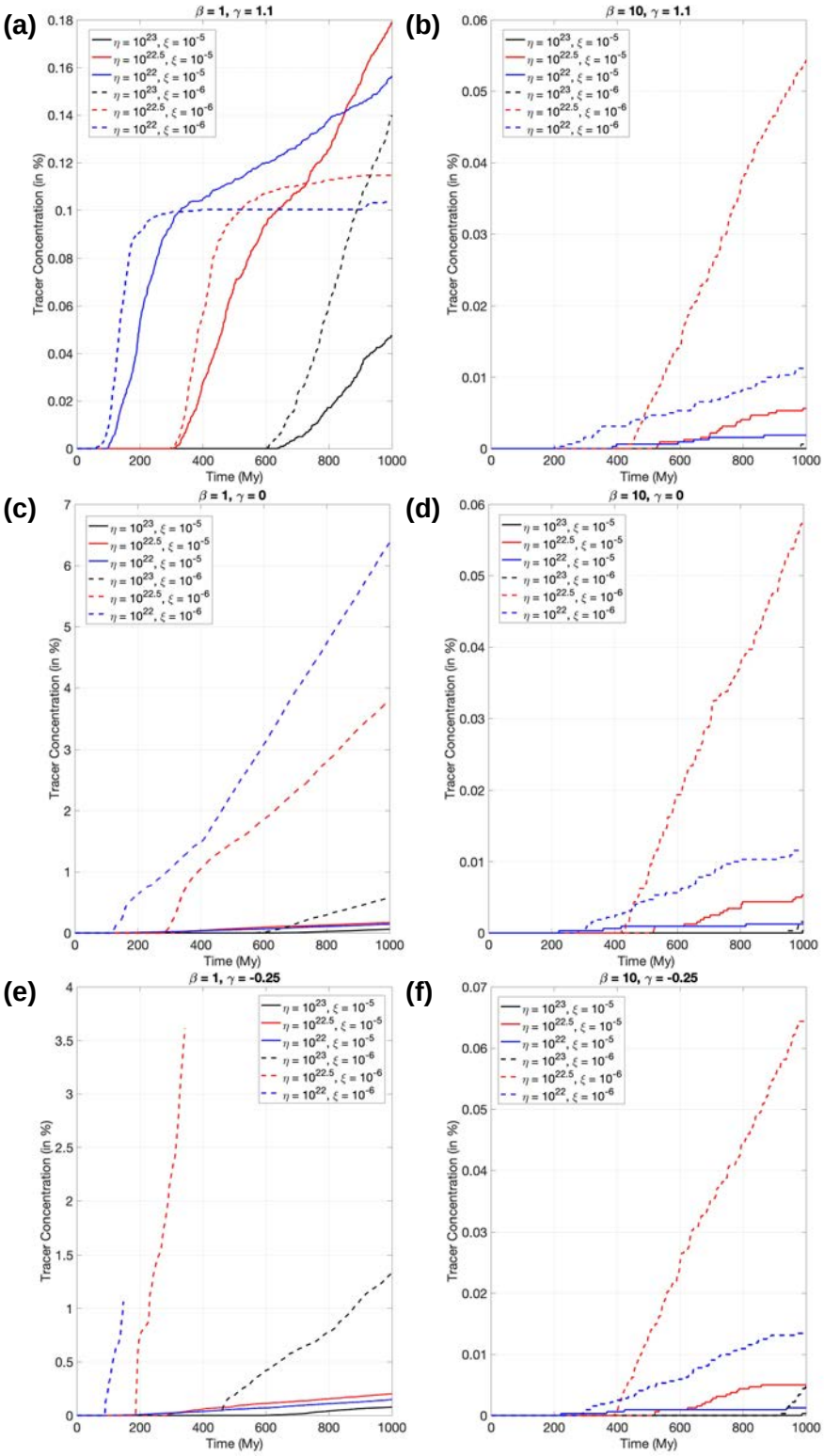

FIGURE 4.4: Plots showing the cumulative amount of chemically distinct tracers leaving the domain via plume entrainment expressed as a percentage of the total number of tracers in the modelling domain.

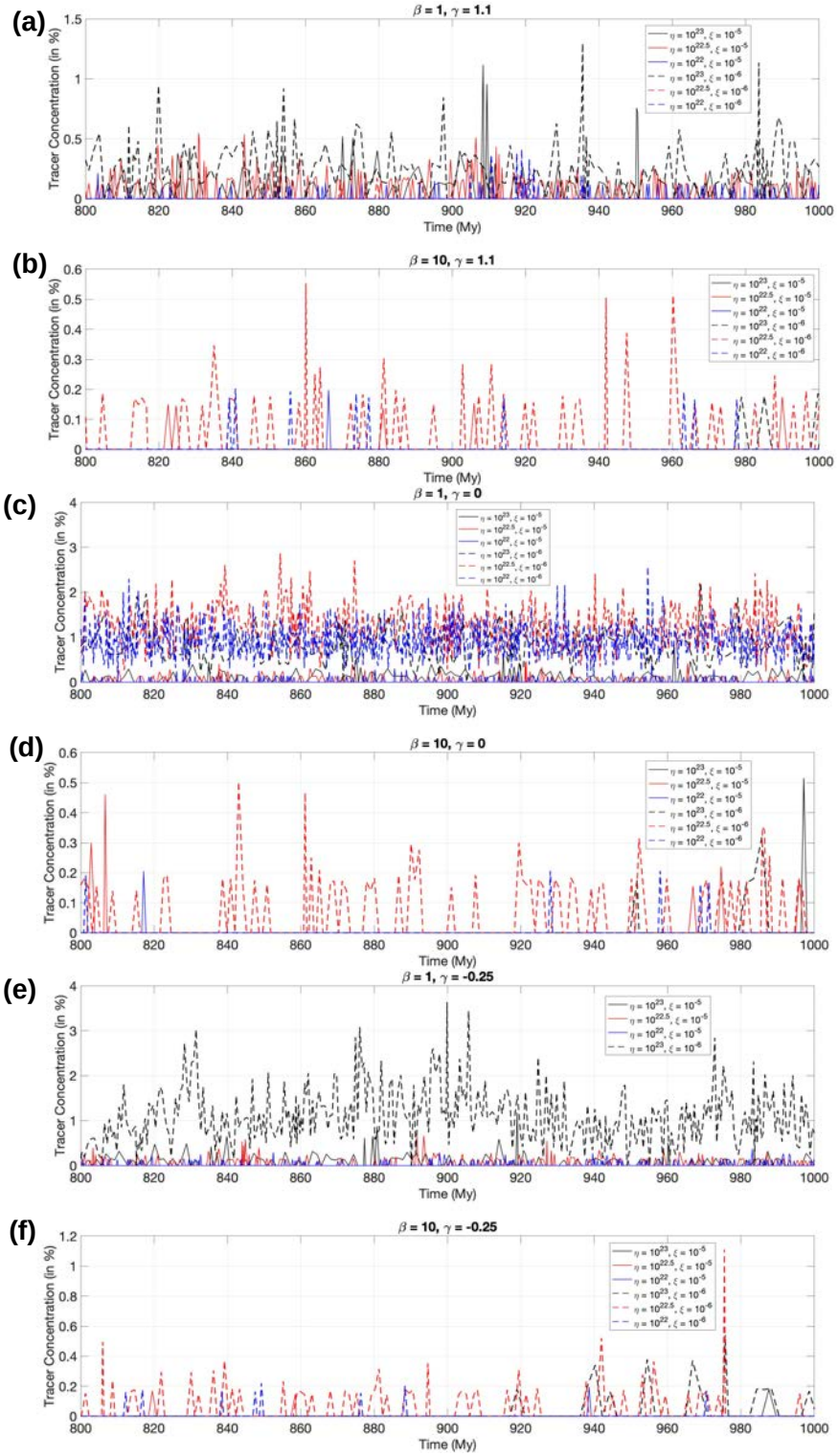

FIGURE 4.5: Concentration of chemically distinct tracers that are transported into the upper mantle within the last 200 Myrs.

4.4 Discussion

Although the numerical models only run up to 1 Gyr in time, studying the influence of the chemically reacted material on mantle dynamics and the rate of changes in concentration can lend some insight into the interesting behaviours that may arise from the “soft CMB" mechanism in the lower mantle. One of which is the accumulation of chemically distinct material at the CMB.

In the previous section, we have seen how the chemically reacted tracers travelling along the CMB towards upwelling plumes and accumulate into a pile-like structure for $\gamma = 1.1$. For the models with tracers that are denser than ambient material, these “piles" act to increase the local density which can subsequently affect the buoyancy-driven flows in the mantle. Figure 4.6 illustrates this phenomenon where in figure 4.6a, the accumulation of the chemically distinct material leads to a pile-like structure at the CMB. Referencing this with temperature field in figure 4.6b indicates that this dense “pile" is situated at the base of the upwelling plume and is presumably very warm. This is similar to the modelled behaviour of ULVZs in a study by Hernlund and Bonati (2019) where they were observed to gather beneath long-lived plumes. The velocity plots from figures 4.6c and 4.6d seem to show different flow patterns compared to the large scale mantle flows at where the pile is located. Since the viscosity of the chemically distinct material is the same as the ambient mantle in the numerical models, there will be viscous coupling of large scale flows from the mantle with internal flows within the denser material, very much similar to stirring motions mentioned in Hernlund and Jellinek (2010). The composition field (figure 4.6a) also shows the composition of the “core" of the pile is slightly depleted compared to the surrounding, and this is because ambient mantle material has been entrained within the pile while the chemically distinct material began to accumulate around the base of the plume. Future studies might look into the compositional gradients within such structures and its influence on the chemical dynamics at the CMB. Moreover, if the dense piles are to remain at the CMB for extended periods of time, they can gradually become chemically equilibrated with the outer core, especially if the material is in direct contact with the stratified layer on top of the outer core. This can for instance reduce the uptake of tungsten isotopes and result in a weakened μ^{182}W signature. In addition, it would be expected that as γ decreases from positive to negative, the increasing buoyancy of the chemically distinct material makes it more susceptible to being entrained in upwelling plumes. Figure 4.7 shows the effect of γ on the temperature and composition fields for models with the same η_0, β and ξ, and it can be seen that the composition plume is more pronounced and continuous with decreasing γ. Interestingly, the width of the thermal plume becomes thinner as well. This might be attributed to the larger buoyancy forces experienced by the plume as the reacted rock is being entrained, which also allows a larger flux of reacted material to be brought to shallower depths of the mantle. We can track the concentration of reacted rock in the plume as it exits the modelling domain, and Figure 4.8a shows how the the concentration changes within the last 200 Myrs for the same models shown in Figure 4.8. If the average value over this time period is computed, figure 4.8b shows that lower γ values tend to have a higher average concentration of reacted

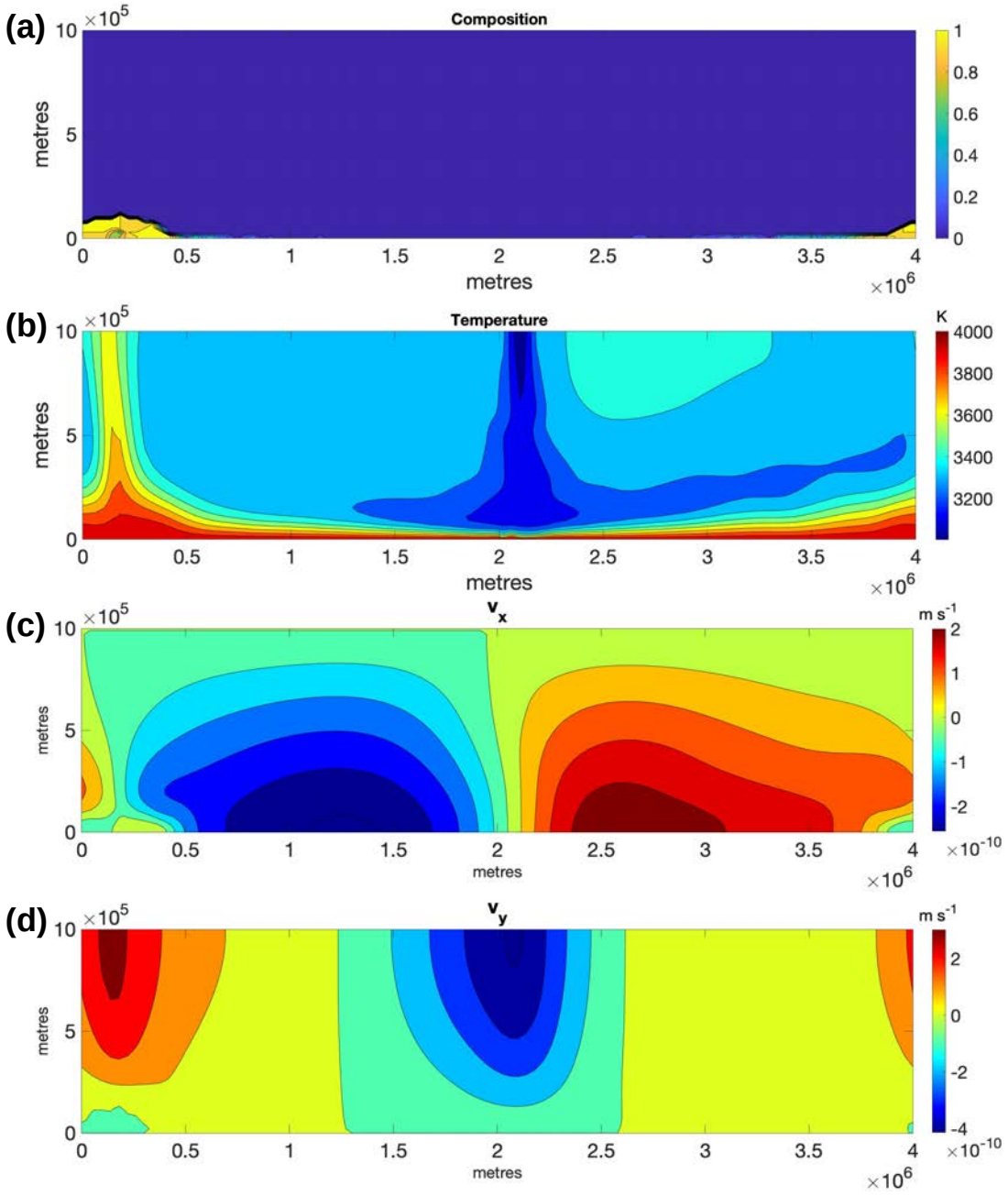

FIGURE 4.6: (a) Composition field, (b) temperature field, (c) v_x, and (d) v_y associated with buoyancy-driven flows for the case $\beta = 1$, $\eta_0 = 10^{22.5}$, $\xi = 10^{-6}$ and $\gamma = 1.1$. Accumulation of compositionally distinct material creates a pile-like structure at the CMB at the base of plumes. Internal flows are also possible due to stirring motion from the overlying mantle flows.

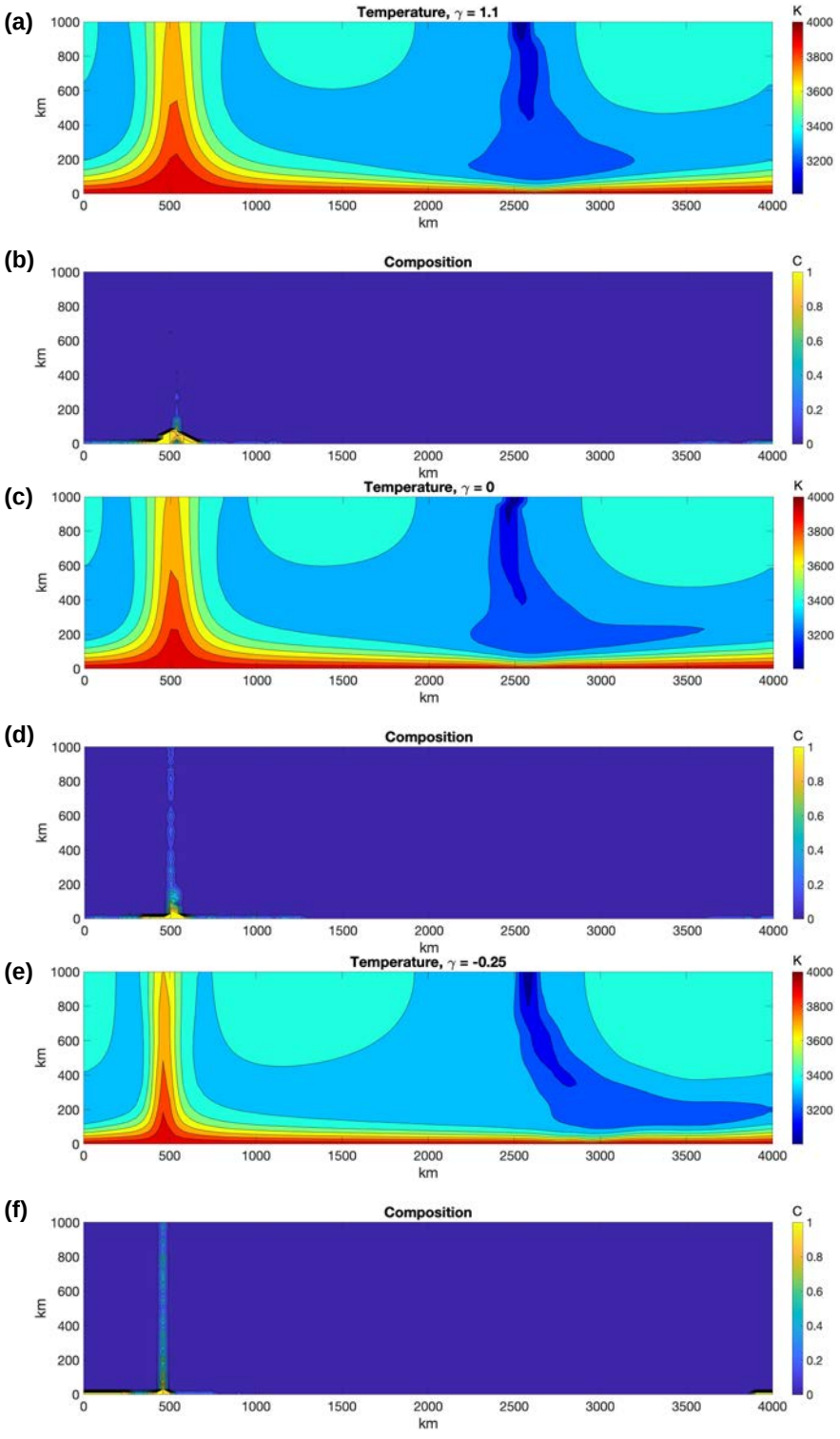

FIGURE 4.7: Contour plots of temperature and composition for $\eta_0 = 10^{23}$, $\beta = 1$ and $\xi = 10^{-6}$. The influence of different γ values are shown in these plots.

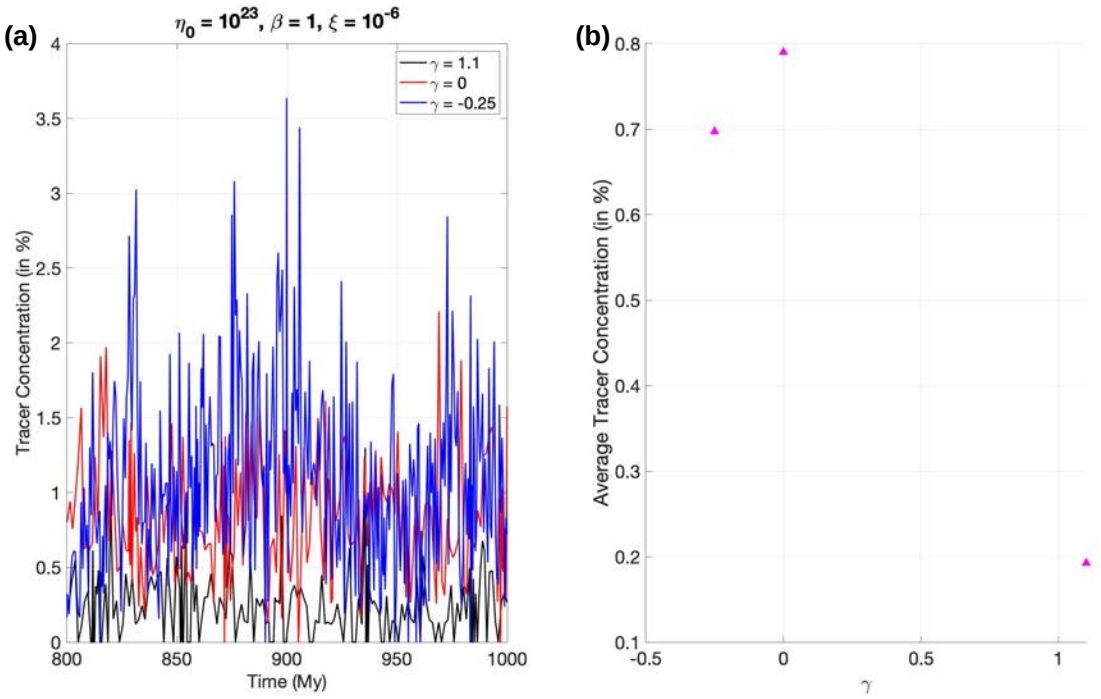

FIGURE 4.8: (a) Concentration of chemically distinct tracers that are transported into the upper mantle within the last 200 Myrs. (b) Average tracer concentration within the last 200 Myrs for different γ.

material in the plume.

To a first approximation, it can be assumed that each individual tracer represents the same mass regardless of composition since the total mass of the system has to be conserved. As such, the tracer concentrations in the previous section can be interpreted to be roughly equivalent to weight percentages of the lower mantle. Going along with this assumption, results have show that after 1 Gyr, the amount of chemically distinct material can be as much as 3.7 wt % (fig 4.5). If this material is assumed to be compositionally similar to LLSVPs, it might be possible for the total concentration to reach similar estimates obtained from seismology (Cottaar & Lekic, 2016) if the “soft CMB" mechanism operated for a significant period of time.

The numerical models here assume that the tracers that are entrained in the upwelling plumes are transported to the upper mantle and do not mix back into the lower mantle. However, if these plumes were to hypothetically extend all the way to the crust and erupt to the surface in the form of hotspot volcanism, these chemically distinct tracers can be a proxy for chemical signatures detected in OIBs originating from the deep Earth. These chemically distinct tracers that are transported out will be mixed with tracers of regular composition, and we can obtain a sense of the expected concentrations based on the tracer proportions. When we track the concentration of the reacted material that is leaving through the top of the domain over the last 200 Myrs for all cases (as was done in fig 4.8), we can see from fig 4.5 that the concentration values tend to oscillate significantly over time to produce a rather

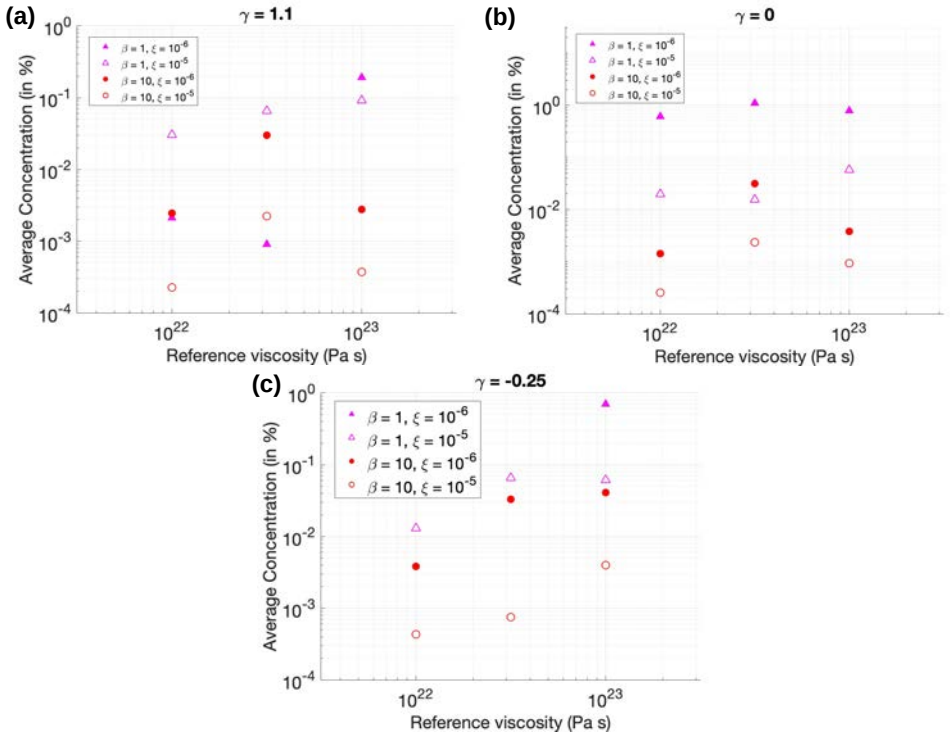

FIGURE 4.9: Concentration of chemically distinct tracers averaged over the last 200 Myrs against reference viscosity for (a) $\gamma = 1.1$, (b) $\gamma = 0$, and $\gamma = -0.25$.

"spiky" temporal profile, indicating that the flux into the upper mantle is not consistent. This might be attributed to the oscillating strength of the plumes caused by the accumulation of hot, chemically distinct material at the base and the effects on the lower thermal boundary layer. If the chemically distinct material is dense ($\gamma = 1.1$) and accumulates at the CMB faster than the rate it is being entrained away, a thermally stratified layer that is gravitationally stable can form at the CMB that acts like a "blanket" on the outer core. This can effectively reduce the heat flux out of the core and significantly reduce the power to the geodynamo. However, if the material is neutrally buoyant ($\gamma = 0$), the difference in composition will not affect the buoyancy field and if it accumulates at the CMB, a layer of compositionally stratified layer will not have any influence on the buoyancy-driven flows. Finally, if the material is positively buoyant ($\gamma = -0.25$), any accumulation into a layer at the CMB will enhance the Rayleigh-Taylor instability due to the combined effects of thermal- and composition-induced buoyancy. This might promote the upwelling of compositionally distinct material from the lower mantle towards the shallow Earth. If we calculate the average concentration for all cases over the last 200 Myrs, fig 4.9 shows that the concentration can range from more than 10^{-4} wt % to slightly more than 1 wt %, essentially spanning over 4 orders of magnitude. However these concentration values are not final and will be subject to multiple changes as the rock encounters additional process such as melting and contamination as described in Chapter 1. It is difficult to understand the extent to which these processes can affect the final concentration of the reacted rock, nevertheless these numerical models can provide some relative bounds of the expected concentration values.

5 | Conclusion and Future Steps

5.1 Summary

Amongst many outstanding questions regarding the Earth's interior, one of which that has intrigued scientists since the last century has been whether reservoirs containing primordial material exist inside the Earth and if so, how and where? Despite numerous discussions on this topic have stemming from different perspectives such as numerical modelling, laboratory experiments, seismic tomography and field evidence from basalts of different origins, there is still no conclusive answer to this question at the moment. Information about these hidden reservoirs is crucial in understanding issues such as the circumstance around Earth's formation and the origin of Earth's volatiles, but to physically travel into the deep Earth for the purpose of collecting rocky evidence is an impossible feat. Therefore, with the recent detection of anomalous isotope signatures from OIBs at different locations on Earth, there has been renewed interest in whether this primordial reservoir could actually be the core itself. However, in order for signatures from the core to manifest on the Earth's surface, there has to be some mechanism(s) that enable some sort of interaction between the core and mantle, followed by transport over a distance of ~ 3000 km that encompasses significant contrasts in temperature, viscosity, and composition. Several mechanisms for interaction between the core and mantle have been proposed over the years that are built on the basic principles of physics and chemistry, and although they provide interesting perspectives on core-mantle interaction individually, it is more likely for multiple mechanisms operating in parallel to facilitate the transfer of chemical signatures from the core to the mantle.

The closest we can probably get to visualise the processes and scales involved in core-mantle interaction is through studying stony-iron meteorites such as pallasites. These meteorites originate from larger asteroids that have underwent similar processes of interior differentiation much like the Earth during the early solar system, but they tend to occur on much smaller length and timescales since these bodies are usually much smaller than the present Earth. Nevertheless, stony-iron meteorites still offer a glimpse into the processes happening in the deep interior of the Earth (and possibly other terrestrial planets). The most abundant group of stony-iron meteorites are pallasites and are composed of approximately equal amounts of silicate (usually olivine), metal, and troilite. When olivine is found together with Fe/Ni metal in these pallasites, this assemblage is usually expected to occur at the

CMB of asteroidal bodies and might potentially contain some signs of chemical interaction between these two components.

In Chapter 1, an overview of the present geochemical evidence, mineral physics constraints, and existing core-mantle interaction mechanisms from the literature is given, followed by the introduction of the new hybrid mechanism. One of the key elements of this hybrid mechanism is the creation of a thin metal-rock mushy layer at the CMB that can induce secondary flows in the mantle via gravitational collapse. Chapter 2 provides a more in depth description and introduces a basic illustrative model with the help of equations to provide some mathematical rigour in explaining the operation of the mechanism. The mechanism was then implemented in an isovisocus and isochemical convection model to study how much downwellings are enhanced based on different mantle viscosities and viscosity contrast between the mushy layer. A simple scaling law that estimates the enhanced material flux into the mushy layer is derived (eq. 2.20), and it was concluded that induced mantle circulation due to the gravitational collapse of the mushy layer becomes comparable to buoyancy-driven mantle flow when the layer's viscosity is reduced to values $\sim 10^5$ times smaller than the overlying mantle.

In Chapter 3, the basic illustrative model is extended by implementing the “soft CMB" mechanism in the mantle with variable viscosity, more specifically a viscosity that is temperature dependent. The results have shown that with increasing convective vigour of the mantle and temperature dependent viscosity, the induced mantle circulation from the gravitational collapse of the mushy layer becomes weaker. This is found to be largely due to the reduction vertical stresses at the CMB with increasing temperature dependent viscosity, which in turns reduces the CMB dynamic topography and hence, the mushy layer thickness. Lastly, in Chapter 4, thermochemical mantle convection calculations were performed with the tracking of compositionally distinct particles that emerge from the mushy layer after going through chemical reactions with the outer core fluid. The chemically distinct material is modelled with positive, negative and neutral buoyancy to investigate the entrainment behaviour of the material. Interesting dynamical behaviours may also arise when the reacted material negatively buoyant and accumulate into pile-like structures around upwelling plumes, mimicking predicted behaviours of ULVZs.

The objective of this dissertation is to study a new core-mantle interaction mechanism that combines existing ideas and knowledge of the subject area. This process attempts to mimic the way natural processes work whereby a number of smaller scale processes are combined to create a single process that can operate on a larger scale with an output larger than the sum of the individual inputs. Hence, the “soft CMB" mechanism was created with this idea in mind that can hopefully offer fresh insights into core-mantle interaction while taking into consideration existing geochemical constraints. This new mechanism has a few main advantages over some of the existing mechanisms: Firstly, the viscous compaction of the silicate rock as it leaves mushy layer guarantees significant expulsion of liquid metal back into the core which ensures the absence of siderophile enhancement in the bulk rock. Although this feature is not unique, it is still an important geochemical constraint that has to be

fulfilled. Secondly, the non-linearity of the process arising from the gravitational collapse of the metal-silicate mush provides a positive feedback on mantle downwellings that amplifies the flux of silicate rock reacting with the liquid outer core. This allows more silicate rock to be chemically processed than other mechanisms occurring in the modern day and depending on the residence time of these rocks at the lower mantle, this mechanism can provide a way to explain the wide range of data observed (Mundl-Petermeier et al., 2020). Moreover, should these reacted rocks become dense and seismically slower than the ambient lower mantle due to their change in composition, their accumulation into relatively thin layers can provide an alternative explanation to the origins of ULVZs (e.g. Brown et al., 2015).

5.1.1 Limitations

It has to be emphasised that this newly proposed mechanism does not claim to be the only way for the core and mantle to interact at the CMB, partly because as of yet there is no conclusive evidence of the existence of mushy zones beneath descending slabs at the CMB, but mostly because of the assumptions made in order for the model to work. Hence, it is worthwhile to reiterate some of these assumptions and uncertainties that exist in the model so that potential studies in the future can address them and improve on the existing model.

One of the biggest uncertainties in the model is with regards to the viscosity of the metal-rock mushy mixture μ. As highlighted in Chapter 2, ξ is an important parameter that controls the efficacy of the mechanism which in turn depends μ. It is expected that as liquid metal begins to intrude in between the silicate pore spaces, the overall viscosity of the mixture will decrease until it is approximately on the same order of magnitude of the liquid metal when the mixture is above the disaggregation limit. Constraining the viscosity of the outer core is incredibly difficult as seen from the estimates spanning over 14 orders of magnitude (Secco, 1995), partly due to the different techniques used to obtain them, and it is also not entirely clear how the mixture viscosity varies with liquid fraction. Some recent estimates have suggested that the outer core viscosity is $\sim 10^{-2}$ Pa s (e.g. Mathews and Guo, 2005; Deleplace and Cardin, 2006; Mound and Buffett, 2007) and if the lower mantle's viscosity is $\sim 10^{21}$ Pa s (Yuen et al., 1982), ξ can span over 23 orders of magnitude. This viscosity contrast makes it extremely challenging to study using numerical models. Hence, any future work that can constrain the viscosity of the mushy mixture would definitely provide better estimates on the flow enhancement via the “soft CMB" mechanism.

In this study, it has been mainly assumed that the mushy layer thickness is equivalent to the dynamic topography created by large scale deviatoric stresses, and this is because decompaction and infiltration of metal into submerged rock has been assumed to occur on time scales much shorter than the residence time of mantle rocks at the CMB. However, if the residence time of the mantle rocks become significantly shorter than the rate of infiltration and decompaction instead, the liquid metal can only percolate up to a shallower height where the condition dictated by equation (2.7) is fulfilled at $h < z < 0$. This means that the amount of rocky material that is able to interact with the outer core liquid is greatly reduced

but at the same time, the amount of chemical exchange that occurs will also depend on the reaction time scales in comparison to the residence time of the mantle rocks. Should the reaction time scale be much longer than the residence time, very little chemical exchange can occur before the submerged rocks flow back into the mantle. Another factor that can influence the percolation height of the liquid metal is the viscosity of the mushy layer. As we have seen in Chapter 2, if this viscosity continues to decrease relative to the mantle viscosity, it is predicted that with decreasing ξ the velocity from collapse-driven flows will be so great that the rate of mantle material going through the mushy layer becomes too large for the infiltration rate to keep up. Hence, determining how much metal infiltration can occur in the layer stresses the importance of constraining the layer viscosity.

Finally, it is important to reiterate the additional processes that can affect the final chemical and isotopic composition of the rock during its journey from the CMB to the surface of the Earth. As discussed in Chapter 1, multiple melting and crystallisation events at different P-T conditions along the way, as well as magma degassing and crustal contamination can give rise to significant fractionation of isotopes and new partitioning of elements, thereby obscuring the rock's original chemical signal from the interaction at the CMB. Although accounting for all these addition effects can be highly complicated, it is still crucial to at least account for relevant processes that can provide the significant sources of uncertainty in the final measurement so that more reliable interpretations of the data can be obtained. A summary of the key points of this new hybrid mechanism in comparison with the other existing mechanisms are shown in Table 5.1.

Core-Mantle Interaction Mechanisms					
	Diffusion across CMB	Chemical Exchange with BMO	Liquid Metal Intrusion	Isostatic Protrusion	Upward Sedimentation
Timing of interaction	After magma ocean solidification	During the first billion years	Recent	Ancient	Recent
Mantle volume	About 1%	As much as 25%	About 1%	About 1%	About 1%
$^{3}He/^{4}He$	Small He concentration in the core	U+Th enrichment in residual melts can suppress signal	Small He concentration in the core	Small He concentration in the core	Small He concentration in the core
$\mu^{182}W$	Small volumes	Depends on original Hf/W in BMO	Small volumes	Small volumes	Small volumes
D/H	S-L fractionation	L-L fractionation	S-L fractionation	S-L fractionation	S-L fractionation
Os isotopes	Small volumes	Depends on original Pt/Os and Re/Os in BMO and core	Small volumes	Small volumes	Small volumes
Excess siderophile elements	Very little	None expected	Depends on compaction	Depends on compaction	Depends on compaction
Advantages	Can transfer core signals if mantle is undersaturated and/or core is saturated	Higher diffusivities can occur in magma ocean	Isotope ratios from core can be transferred without excess siderophiles	Material might become chemically equilibrated if remain undisturbed	Can possibly account for variations in length-of-day
Disadvantages	Very inefficient in silicates. Highly dependent on grain boundary volumes	Secondary fractionation effects can occur during freezing of BMO	Residence time of mantle material at CMB unconstrained	ULVZs not detected at every OIB location. Unconstrained plume entrainment efficiency	Mixing of exsolved SiO_2-rich domains from the core will dilute isotope signals

Core-Mantle Interaction Mechanisms					
	Poroelastic Entrainment	Thermodiffusion	Morphological Instabilities	Surface Tension	Gravitational Collapse of Metal-Silicate Mush
Timing of interaction	Recent	Any time	Any time	Any time	Recent
Mantle volume	About 1%	About 1%	About 1%	Less than 1%	More than 1%
$^{3}He/^{4}He$	Small He concentration in the core				
$\mu^{182}W$	Small volumes				
D/H	S-L fractionation				
Os isotopes	Small volumes and S-L fractionation				
Excess siderophile elements	Somewhat significant, depends on compaction	Depends on liquid iron entrainment process into lower mantle	Significant	Significant	Depends on compaction
Advantages	Can possibly account for unique isotope and chemical ratios found in OIBs	Iron isotope fractionation can be potential signal from the core	Can possibly account for unique isotope and chemical ratios found in OIBs	Can possibly account for unique isotope and chemical ratios found in OIBs	Can possibly account for unique isotope and chemical ratios found in OIBs and enhance metal-silicate interaction
Disadvantages	Requires high strain rates at the CMB. Physical entrainment of core liquid	Iron isotope fractionation does not correlate with other isotope tracers	Energetically unfeasible. Physical entrainment of core liquid	Very inefficient. Physical entrainment of core liquid	Viscosity of mushy layer unconstrained. Depends on metal intrusion height

TABLE 5.1: A table that compares and summarises the key aspects of each core-mantle interaction mechanism including the new hybrid mechanism proposed in this thesis and the associated uncertainties of each isotope tracer. S-L: Solid-liquid. L-L: Liquid-liquid.

5.2 Future Outlook

In light of renewed interest on core-mantle interaction and its implications on phenomena in the deep mantle such as the existence of primordial reservoirs and seismically detected structures, possible ideas that extend from the “soft CMB" mechanism are described below.

5.2.1 Two-phase Flows within the Mushy Zone

The mushy layer in this model is treated as a single phase due to the large scale flows that operate in the overlying mantle in comparison with the small scale flows that are expected to occur within the layer. However, this approximation neglects the physical and chemical dynamics that can happen between the core liquid and silicate rocks which have important effects to be considered as well. Modelling the two-phase flows within the mushy layer can provide useful constraints on percolation and compaction timescales, which can be compared with the timescales of other important processes such as the enhanced downwellings into the layer. Moreover, since chemical exchange is occurring between both phases, additional complexities that arise from chemical buoyancy and chemical disequilibrium can develop reaction-driven convection of core liquid within the mushy layer itself. For instance, if the core liquid is undersaturated in oxygen, FeO can be transferred from the rocky component which can lower the density of the liquid metal and contribute to the stratified layer at the top of the core. The rate and efficiency of chemical exchange would depend very much on several crucial factors including: solid grain sizes, wettability of the solid grain boundaries, the relative diffusivity of the chemical species of interest along grain boundaries and within the liquid, the surface area in contact with the liquid, etc. These parameters can be potentially constrained by experimental and molecular dynamical studies in the future.

5.2.2 Isostatic Topography vs Dynamic Topography

In this study, only the effects of dynamic topography at the CMB are considered but from the thermochemical convection models in Chapter 4, it can be seen that if the reacted rocks are assumed to become denser after undergoing chemical exchange with the core fluid, they can accumulate near upwellings plumes to create dense piles. These dense piles would produce isostatic topography on the CMB, as described in Chapter 1 and can remain at the CMB for extended periods of time if they are resistant to entrainment. It would also be important to consider whether the viscosity of the chemically reacted material would be different from the ambient mantle because the degree of viscous coupling between the piles and surrounding mantle material can determine whether internal flows are produced or not, much like what is described in (Hernlund & Jellinek, 2010). Moreover, should internal flows be present within the dense piles, it might be possible for stresses from these flows to create dynamic topography as well on top of the isostatic topography that already exists. Hence, investigating the relative contributions of isostatic topography and dynamic topography at the CMB, as well as the different interaction mechanisms that can subsequently arise from

them might shed some light on the complicated dynamics that are playing out at the CMB across different scales.

5.2.3 Effects on the Outer Core

This dissertation has mainly discussed and investigated the phenomenon of core-mantle interaction via the perspective of the mantle. However, in order to have a greater understanding on this topic, the perspective of the core has to be included as well. It is well understood that the dynamics of the core are fundamentally different from that of the mantle, since core processes operating on timescales much shorter than mantle dynamics timescales ($\sim$days to 10^3 years) (Olson, 2015) and lateral density variations are predicted to be smaller that 10^{-8} (Stevenson, 1987). Nevertheless, the CMB has been facilitating “communication" between the core and mantle since core formation through the exchange of heat, momentum, mass and charge, with each of these interactions having profound consequences on core evolution and dynamics. Potential future research directions can include investigating how topography at the CMB affects the core magnetic field and its secular variation and acceleration through the influence on fluid flow and stratification at the top of the core. This can be referenced and compared with existing geomagnetic data of the Earth to see whether it is possible to detect topography at the CMB in addition to seismic methods. In addition, it would be interesting to look at the potential effects of core-mantle electromagnetic coupling on length-of-day variations especially since liquid metal percolation can create regions of high electrical conductivity on the mantle side of the CMB. Lastly, it must be emphasised that for any material on the mantle side that is interacting with the outer core at the CMB, the chemical reactions taking place is only with the stratified layer rather than the outer core as a whole. Hence, if the material from the mantle were to come into chemical equilibrium with the stratified layer, there will be less transfer of chemical species such as tungsten across the CMB over time and there will a gradual decrease in the strength of the isotopic signal detected over time. It will be important to consider into how the core accommodates chemical exchange across different parts of the CMB where for instance a descending slab with different oxidation state from the equilibrated material comes into contact and react with the outer core’s stratified layer.

Bibliography

Abe, Y., & Matsui, T. (1985). The formation of an impact-generated H_2O atmosphere and its implications for the early thermal history of the earth. *Journal of Geophysical Research: Solid Earth*, *90*(S02), C545–C559.

Agee, C. B., & Walker, D. (1988). Mass balance and phase density constraints on early differentiation of chondritic mantle. *Earth and planetary science letters*, *90*(2), 144–156.

Agnor, C. B., Canup, R. M., & Levison, H. F. (1999). On the character and consequences of large impacts in the late stage of terrestrial planet formation. *Icarus*, *142*(1), 219–237.

Ahrens, T. J. (1993). Impact erosion of terrestrial planetary atmospheres. *Annual Review of Earth and Planetary Sciences*, *21*(1), 525–555.

Alexander, C. O., Bowden, R., Fogel, M., Howard, K., Herd, C., & Nittler, L. (2012). The provenances of asteroids, and their contributions to the volatile inventories of the terrestrial planets. *Science*, *337*(6095), 721–723.

Alexandrakis, C., & Eaton, D. W. (2010). Precise seismic-wave velocity atop Earth's core: No evidence for outer-core stratification. *Physics of the Earth and Planetary Interiors*, *180*(1-2), 59–65.

Alfè, D., Gillan, M., & Price, G. D. (2002). Composition and temperature of the Earth's core constrained by combining ab initio calculations and seismic data. *Earth and Planetary Science Letters*, *195*(1-2), 91–98.

Allègre, C. J., Staudacher, T., Sarda, P., & Kurz, M. (1983). Constraints on evolution of Earth's mantle from rare gas systematics. *Nature*, *303*(5920), 762–766.

Ammann, M., Brodholt, J., Wookey, J., & Dobson, D. (2010). First-principles constraints on diffusion in lower-mantle minerals and a weak D" layer. *Nature*, *465*(7297), 462–465.

Arevalo Jr, R., McDonough, W. F., & Luong, M. (2009). The K/U ratio of the silicate Earth: Insights into mantle composition, structure and thermal evolution. *Earth and Planetary Science Letters*, *278*(3-4), 361–369.

Armytage, R. M., Jephcoat, A. P., Bouhifd, M. A., & Porcelli, D. (2013). Metal–silicate partitioning of iodine at high pressures and temperatures: Implications for the Earth's core and ^{129*}Xe budgets. *Earth and Planetary Science Letters*, *373*, 140–149.

Asari, S., Shimizu, H., & Utada, H. (2006). Variability of the topographic core-mantle torque calculated from core surface flow models. *Physics of the Earth and Planetary Interiors*, *154*(1), 85–111.

Badro, J., Siebert, J., & Nimmo, F. (2016). An early geodynamo driven by exsolution of mantle components from Earth's core. *Nature*, *536*, 326–328. https://doi.org/10.1038/nature18594

Badro, J., Brodholt, J. P., Piet, H., Siebert, J., & Ryerson, F. J. (2015). Core formation and core composition from coupled geochemical and geophysical constraints. *Proceedings of the National Academy of Sciences*, *112*(40), 12310–12314.

Badro, J., Côté, A. S., & Brodholt, J. P. (2014). A seismologically consistent compositional model of Earth's core. *Proceedings of the National Academy of Sciences*, *111*(21), 7542–7545.

Bagdassarov, N., Golabek, G., Solferino, G., & Schmidt, M. (2009). Constraints on the Fe–S melt connectivity in mantle silicates from electrical impedance measurements. *Physics of the Earth and Planetary Interiors*, *177*(3-4), 139–146.

Baker, J., Bizzarro, M., Wittig, N., Connelly, J., & Haack, H. (2005). Early planetesimal melting from an age of 4.5662 Gyr for differentiated meteorites. *Nature*, *436*(7054), 1127–1131.

Ballhaus, C., & Ellis, D. J. (1996). Mobility of core melts during Earth's accretion. *Earth and Planetary Science Letters*, *143*(1-4), 137–145.

Ballmer, M. D., Houser, C., Hernlund, J. W., Wentzcovitch, R. M., & Hirose, K. (2017). Persistence of strong silica-enriched domains in the Earth's lower mantle. *Nature Geoscience*, *10*(3), 236–240.

Bloxham, J., & Gubbins, D. (1985). The secular variation of earth's magnetic field. *Nature*, *317*(6040), 777–781.

Bloxham, J., & Jackson, A. (1992). Time-dependent mapping of the magnetic field at the core-mantle boundary. *Journal of Geophysical Research: Solid Earth*, *97*(B13), 19537–19563.

Booker, J. R., & Stengel, K. C. (1978). Further thoughts on convective heat transport in a variable-viscosity fluid. *Journal of Fluid Mechanics*, *86*(2), 289–291.

Bouffard, M., Landeau, M., & Goument, A. (2020). Convective erosion of a primordial stratification atop Earth's core. *Geophysical Research Letters*, *47*(14), e2020GL087109.

Bouhifd, M. A., Andrault, D., Bolfan-Casanova, N., Hammouda, T., & Devidal, J.-L. (2013). Metal–silicate partitioning of Pb and U: Effects of metal composition and oxygen fugacity. *Geochimica et Cosmochimica Acta*, *114*, 13–28.

Bouhifd, M. A., Jephcoat, A., Porcelli, D., Kelley, S., & Marty, B. (2020). Potential of Earth's core as a reservoir for noble gases: Case for helium and neon. *Geochemical Perspectives Letters*, 15–18.

Boyet, M., Blichert-Toft, J., Rosing, M., Storey, M., Télouk, P., & Albarède, F. (2003). ^{142}Nd evidence for early Earth differentiation. *Earth and Planetary Science Letters*, *214*(3-4), 427–442.

Boyet, M., & Carlson, R. W. (2005). ^{142}Nd evidence for early (> 4.53 Ga) global differentiation of the silicate Earth. *Science*, *309*(5734), 576–581.

Boyet, M., & Carlson, R. W. (2006). A new geochemical model for the Earth's mantle inferred from ^{146}Sm–^{142}Nd systematics. *Earth and Planetary Science Letters*, *250*(1-2), 254–268.

Braginsky, S. I. (1993). MAC-Oscillations of the Hidden Ocean of the Core. *Journal of geomagnetism and geoelectricity*, *45*(11-12), 1517–1538.

Braginsky, S. I. (1999). Dynamics of the stably stratified ocean at the top of the core. *Physics of the earth and planetary interiors*, *111*(1-2), 21–34.

Brandon, A. D., Graham, D. W., Waight, T., & Gautason, B. (2007). ^{186}Os and ^{187}Os enrichments and high-^{3}He/^{4}He sources in the Earth's mantle: evidence from Icelandic picrites. *Geochimica et Cosmochimica Acta*, *71*(18), 4570–4591.

Brandon, A. D., Norman, M. D., Walker, R. J., & Morgan, J. W. (1999). ^{186}Os–^{187}Os systematics of Hawaiian picrites. *Earth and Planetary Science Letters*, *174*(1-2), 25–42.

Brandon, A. D., & Walker, R. J. (2005). The debate over core–mantle interaction. *Earth and Planetary Science Letters*, *232*(3-4), 211–225.

Brandon, A. D., Walker, R. J., Puchtel, I. S., Becker, H., Humayun, M., & Revillon, S. (2003). ^{186}Os–^{187}Os systematics of Gorgona Island komatiites: implications for early growth of the inner core. *Earth and Planetary Science Letters*, *206*(3-4), 411–426.

Brodholt, J., & Badro, J. (2017). Composition of the low seismic velocity E' layer at the top of Earth's core. *Geophysical Research Letters*, *44*(16), 8303–8310.

Brown, S. P., Thorne, M. S., Miyagi, L., & Rost, S. (2015). A compositional origin to ultralow-velocity zones. *Geophysical Research Letters*, *42*(4), 1039–1045.

Buffett, B. (2014). Geomagnetic fluctuations reveal stable stratification at the top of the Earth's core. *Nature*, *507*(7493), 484–487.

Buffett, B., Knezek, N., & Holme, R. (2016). Evidence for MAC waves at the top of Earth's core and implications for variations in length of day. *Geophysical Journal International*, *204*(3), 1789–1800.

Buffett, B. A. (1992). Constraints on magnetic energy and mantle conductivity from the forced nutations of the Earth. *Journal of Geophysical Research: Solid Earth*, *97*(B13), 19581–19597.

Buffett, B. A. (1996). Gravitational oscillations in the length of day. *Geophysical Research Letters*, *23*(17), 2279–2282.

Buffett, B. A., Garnero, E. J., & Jeanloz, R. (2000). Sediments at the top of Earth's core. *Science*, *290*(5495), 1338–1342.

Buffett, B. A., & Seagle, C. T. (2010). Stratification of the top of the core due to chemical interactions with the mantle. *Journal of Geophysical Research: Solid Earth*, *115*(B4).

Burton, K. W., Schiano, P., Birck, J.-L., & Allègre, C. J. (1999). Osmium isotope disequilibrium between mantle minerals in a spinel-lherzolite. *Earth and Planetary Science Letters*, *172*(3-4), 311–322.

Caldwell, W. A., Nguyen, J. H., Pfrommer, B. G., Mauri, F., Louie, S. G., & Jeanloz, R. (1997). Structure, bonding, and geochemistry of xenon at high pressures. *Science*, *277*(5328), 930–933.

Cameron, A. G. (1983). Origin of the atmospheres of the terrestrial planets. *Icarus*, *56*(2), 195–201.

Canil, D., O'Neill, H. S. C., Pearson, D., Rudnick, R. L., McDonough, W. F., & Carswell, D. (1994). Ferric iron in peridotites and mantle oxidation states. *Earth and Planetary Science Letters*, *123*(1-3), 205–220.

Canup, R. M. (2012). Forming a Moon with an Earth-like composition via a giant impact. *Science*, *338*(6110), 1052–1055.

Canup, R. M., & Asphaug, E. (2001). Origin of the Moon in a giant impact near the end of the Earth's formation. *Nature*, *412*(6848), 708–712.

Carlson, R. W., & Boyet, M. (2008). Composition of the Earth's interior: The importance of early events. *Philosophical Transactions of the Royal Society A: Mathematical, Physical and Engineering Sciences*, *366*(1883), 4077–4103.

Caro, G., Bourdon, B., Birck, J.-L., & Moorbath, S. (2003). ^{146}Sm–^{142}Nd evidence from Isua metamorphosed sediments for early differentiation of the Earth's mantle. *Nature*, *423*(6938), 428–432.

Caro, G., Bourdon, B., Birck, J.-L., & Moorbath, S. (2006). High-precision ^{142}Nd/^{144}Nd measurements in terrestrial rocks: Constraints on the early differentiation of the Earth's mantle. *Geochimica et Cosmochimica Acta*, *70*(1), 164–191.

Chambers, J. E. (2004). Planetary accretion in the inner Solar System. *Earth and Planetary Science Letters*, *223*(3-4), 241–252.

Christensen, U. R. (1984). Heat transport by variable viscosity convection and implications for the Earth's thermal evolution. *Physics of the Earth and planetary interiors*, *35*(4), 264–282.

Christensen, U. R., & Aubert, J. (2006). Scaling properties of convection-driven dynamos in rotating spherical shells and application to planetary magnetic fields. *Geophysical Journal International*, *166*(1), 97–114.

Christensen, U. R., & Yuen, D. A. (1985). Layered convection induced by phase transitions. *Journal of Geophysical Research: Solid Earth*, *90*(B12), 10291–10300.

Clarke, W. B., Beg, M., & Craig, H. (1969). Excess ^{3}He in the sea: Evidence for terrestrial primodal helium. *Earth and Planetary Science Letters*, *6*(3), 213–220.

Clesi, V., Bouhifd, M. A., Bolfan-Casanova, N., Manthilake, G., Schiavi, F., Raepsaet, C., Bureau, H., Khodja, H., & Andrault, D. (2018). Low hydrogen contents in the cores of terrestrial planets. *Science advances*, *4*(3), e1701876.

Colombi, A., Nissen-Meyer, T., Boschi, L., & Giardini, D. (2014). Seismic waveform inversion for core–mantle boundary topography. *Geophysical Journal International*, *198*(1), 55–71.

Cook, D., Walker, R., Horan, M., Wasson, J., & Morgan, J. (2004). Pt-Re-Os systematics of group IIAB and IIIAB iron meteorites. *Geochimica et Cosmochimica Acta*, *68*(6), 1413–1431.

Corgne, A., Liebske, C., Wood, B. J., Rubie, D. C., & Frost, D. J. (2005). Silicate perovskite-melt partitioning of trace elements and geochemical signature of a deep perovskitic reservoir. *Geochimica et Cosmochimica Acta*, *69*(2), 485–496.

Corgne, A., & Wood, B. J. (2002). $CaSiO_3$ and $CaTiO_3$ perovskite-melt partitioning of trace elements: Implications for gross mantle differentiation. *Geophysical Research Letters*, *29*(19), 39–1.

Cottaar, S., & Lekic, V. (2016). Morphology of seismically slow lower-mantle structures. *Geophysical Supplements to the Monthly Notices of the Royal Astronomical Society*, *207*(2), 1122–1136.

Creager, K. C., & Jordan, T. H. (1986). Slab penetration into the lower mantle beneath the Mariana and other island arcs of the northwest Pacific. *Journal of Geophysical Research: Solid Earth*, *91*(B3), 3573–3589.

Crocket, J. H. (2000). PGE in fresh basalt, hydrothermal alteration products, and volcanic incrustations of Kilauea volcano, Hawaii. *Geochimica et Cosmochimica Acta*, *64*(10), 1791–1807.

Ćuk, M., & Stewart, S. T. (2012). Making the Moon from a fast-spinning Earth: A giant impact followed by resonant despinning. *science*, *338*(6110), 1047–1052.

Dahl, T. W., & Stevenson, D. J. (2010). Turbulent mixing of metal and silicate during planet accretion — And interpretation of the Hf–W chronometer. *Earth and Planetary Science Letters*, *295*(1-2), 177–186.

Davaille, A., & Limare, A. (2015). 7.03 - Laboratory Studies of Mantle Convection. In G. Schubert (Ed.), *Treatise on geophysics (second edition)* (Second Edition, pp. 73–144). Elsevier. https://doi.org/10.1016/B978-0-444-53802-4.00128-7

Davaille, A. (1999a). Simultaneous generation of hotspots and superswells by convection in a heterogeneous planetary mantle. *Nature*, *402*(6763), 756–760.

Davaille, A. (1999b). Two-layer thermal convection in miscible viscous fluids. *Journal of Fluid Mechanics*, *379*, 223–253.

Davaille, A., Girard, F., & Le Bars, M. (2002). How to anchor hotspots in a convecting mantle? *Earth and Planetary Science Letters*, *203*(2), 621–634.

Davaille, A., & Jaupart, C. (1993). Transient high-Rayleigh-number thermal convection with large viscosity variations. *Journal of Fluid Mechanics*, *253*, 141–166.

Davies, C., Pozzo, M., Gubbins, D., & Alfe, D. (2015). Constraints from material properties on the dynamics and evolution of Earth's core. *Nature Geoscience*, *8*(9), 678–685.

Davies, C. J., Pozzo, M., Gubbins, D., & Alfè, D. (2020). Transfer of oxygen to Earth's core from a long-lived magma ocean. *Earth and Planetary Science Letters*, *538*, 116208.

Davies, G. F. (1985). Heat deposition and retention in a solid planet growing by impacts. *Icarus*, *63*(1), 45–68.

Day, J. M. (2013). Hotspot volcanism and highly siderophile elements. *Chemical Geology*, *341*, 50–74.

Day, J. M., Pearson, D. G., Macpherson, C. G., Lowry, D., & Carracedo, J. C. (2010). Evidence for distinct proportions of subducted oceanic crust and lithosphere in HIMU-type mantle beneath El Hierro and La Palma, Canary Islands. *Geochimica et Cosmochimica Acta*, *74*(22), 6565–6589.

Deguen, R., Landeau, M., & Olson, P. (2014). Turbulent metal–silicate mixing, fragmentation, and equilibration in magma oceans. *Earth and Planetary Science Letters*, *391*, 274–287.

Deleplace, B., & Cardin, P. (2006). Viscomagnetic torque at the core mantle boundary. *Geophysical Journal International*, *167*(2), 557–566.

Deschamps, F., & Li, Y. (2019). Core-mantle boundary dynamic topography: Influence of postperovskite viscosity. *Journal of Geophysical Research: Solid Earth*, *124*(8), 9247–9264.

Deschamps, F., Rogister, Y., & Tackley, P. J. (2018). Constraints on core–mantle boundary topography from models of thermal and thermochemical convection. *Geophysical Journal International*, *212*(1), 164–188.

Dobson, D. P., & Brodholt, J. P. (2005). Subducted banded iron formations as a source of ultralow-velocity zones at the core–mantle boundary. *Nature*, *434*(7031), 371–374.

Dziewonski, A. M., & Anderson, D. L. (1981). Preliminary reference Earth model. *Physics of the earth and planetary interiors*, *25*(4), 297–356.

Eremets, M. I., Gregoryanz, E. A., Struzhkin, V. V., Mao, H.-k., Hemley, R. J., Mulders, N., & Zimmerman, N. M. (2000). Electrical conductivity of xenon at megabar pressures. *Physical review letters*, *85*(13), 2797.

Faure, P., Bouhifd, M. A., Boyet, M., Manthilake, G., Clesi, V., & Devidal, J.-L. (2020). Uranium and thorium partitioning in the bulk silicate Earth and the oxygen content of Earth's core. *Geochimica et Cosmochimica Acta*, *275*, 83–98.

Fearn, D. R., & Loper, D. E. (1981). Compositional convection and stratification of Earth's core. *Nature*, *289*(5796), 393–394.

Fischer, R. A., Nakajima, Y., Campbell, A. J., Frost, D. J., Harries, D., Langenhorst, F., Miyajima, N., Pollok, K., & Rubie, D. C. (2015). High pressure metal–silicate partitioning of Ni, Co, V, Cr, Si, and O. *Geochimica et Cosmochimica Acta*, *167*, 177–194.

Frost, D. J., Asahara, Y., Rubie, D. C., Miyajima, N., Dubrovinsky, L. S., Holzapfel, C., Ohtani, E., Miyahara, M., & Sakai, T. (2010). Partitioning of oxygen between the Earth's mantle and core. *Journal of Geophysical Research: Solid Earth*, *115*(B2).

Fuge, R., & Johnson, C. C. (1984). Evidence for the chalcophile nature of iodine. *Chemical Geology*, *43*(3-4), 347–352.

Fukai, Y., & Suzuki, T. (1986). Iron-water reaction under high pressure and its implication in the evolution of the Earth. *Journal of Geophysical Research: Solid Earth*, *91*(B9), 9222–9230.

Gaetani, G. A., & Grove, T. L. (1999). Wetting of mantle olivine by sulfide melt: Implications for Re/Os ratios in mantle peridotite and late-stage core formation. *Earth and Planetary Science Letters*, *169*(1-2), 147–163.

Gaffney, A. M., Nelson, B. K., Reisberg, L., & Eiler, J. (2005). Oxygen–osmium isotope systematics of west maui lavas: A record of shallow-level magmatic processes. *Earth and Planetary Science Letters*, *239*(1-2), 122–139.

Galer, S., & O'nions, R. (1985). Residence time of thorium, uranium and lead in the mantle with implications for mantle convection. *Nature*, *316*(6031), 778–782.

Gerya, T. (2019). *Introduction to numerical geodynamic modelling*. Cambridge University Press.

Gerya, T. V., & Yuen, D. A. (2003). Characteristics-based marker-in-cell method with conservative finite-differences schemes for modeling geological flows with strongly variable transport properties. *Physics of the Earth and Planetary Interiors*, *140*(4), 293–318.

Ghanbarzadeh, S., Hesse, M. A., & Prodanović, M. (2017). Percolative core formation in planetesimals enabled by hysteresis in metal connectivity. *Proceedings of the National Academy of Sciences*, *114*(51), 13406–13411.

Glane, S., & Buffett, B. (2018). Enhanced core-mantle coupling due to stratification at the top of the core. *Frontiers in Earth Science*, *6*, 171.

Goles, G. G., & Anders, E. (1962). Abundances of iodine tellurium and uranium in meteorites. *Geochimica et Cosmochimica Acta*, *26*(7), 723–737.

Gomi, H., Ohta, K., Hirose, K., Labrosse, S., Caracas, R., Verstraete, M. J., & Hernlund, J. W. (2013). The high conductivity of iron and thermal evolution of the Earth's core. *Physics of the Earth and Planetary Interiors*, *224*, 88–103.

Gonnermann, H. M., & Mukhopadhyay, S. (2007). Non-equilibrium degassing and a primordial source for helium in ocean-island volcanism. *Nature*, *449*(7165), 1037–1040.

Gray, C., & Compston, W. (1974). Excess ^{26}Mg in the Allende meteorite. *Nature*, *251*(5475), 495–497.

Gubbins, D., & Davies, C. (2013). The stratified layer at the core–mantle boundary caused by barodiffusion of oxygen, sulphur and silicon. *Physics of the Earth and Planetary Interiors*, *215*, 21–28.

Gubbins, D., Masters, T., & Jacobs, J. (1979). Thermal evolution of the Earth's core. *Geophysical Journal International*, *59*(1), 57–99.

Gülcher, A. J., Gebhardt, D. J., Ballmer, M. D., & Tackley, P. J. (2020). Variable dynamic styles of primordial heterogeneity preservation in the Earth's lower mantle. *Earth and Planetary Science Letters*, *536*, 116160.

Hager, B., & Richards, M. (1989). Long-wavelength variations in Earth's geoid: Physical models and dynamical implications. *Philosophical Transactions of the Royal Society of London. Series A, Mathematical and Physical Sciences*, *328*(1599), 309–327.

Hager, B. H., Clayton, R. W., Richards, M. A., Comer, R. P., & Dziewonski, A. M. (1985). Lower mantle heterogeneity, dynamic topography and the geoid. *Nature*, *313*(6003), 541–545.

Haisch Jr, K. E., Lada, E. A., & Lada, C. J. (2001). Disk frequencies and lifetimes in young clusters. *The Astrophysical Journal Letters*, *553*(2), L153.

Halliday, A. N. (2000). Hf-W chronometry and inner solar system accretion rates. *From Dust to Terrestrial Planets*, 355–370.

Halliday, A. N. (2013). The origins of volatiles in the terrestrial planets. *Geochimica et Cosmochimica Acta*, *105*, 146–171.

Halliday, A. N., & Kleine, T. (2006). Meteorites and the timing, mechanisms, and conditions of terrestrial planet accretion and early differentiation. *Meteorites and the early solar system II*, 775–801.

Hallis, L. J., Huss, G. R., Nagashima, K., Taylor, G. J., Halldórsson, S. A., Hilton, D. R., Mottl, M. J., & Meech, K. J. (2015). Evidence for primordial water in Earth's deep mantle. *Science*, *350*(6262), 795–797.

Hansen, U., & Yuen, D. A. (1988). Numerical simulations of thermal-chemical instabilities at the core–mantle boundary. *Nature*, *334*(6179), 237–240.

Harper, C. L., & Jacobsen, S. B. (1992). Evidence from coupled ^{147}Sm–^{143}Nd and ^{146}Sm–^{142}Nd systematics for very early (4.5-Gyr) differentiation of the Earth's mantle. *Nature*, *360*(6406), 728–732.

Harrison, T. M. (2009). The Hadean crust: evidence from > 4 Ga zircons. *Annual Review of Earth and Planetary Sciences*, *37*, 479–505.

Hart, S. R., Ravizza, G. E., & Basu, A. (1996). Os partitioning between phases in lherzolite and basalt. *Geophysical Monograph-American Geophysical Union*, *95*, 123–134.

Hayashi, C., Nakazawa, K., & Mizuno, H. (1979). Earth's melting due to the blanketing effect of the primordial dense atmosphere. *Earth and Planetary Science Letters*, *43*(1), 22–28.

Helffrich, G. (2012). How light element addition can lower core liquid wave speeds. *Geophysical Journal International*, *188*(3), 1065–1070.

Helffrich, G., Ballmer, M. D., & Hirose, K. (2018). Core-exsolved SiO2 dispersal in the earth's mantle. *Journal of Geophysical Research: Solid Earth*, *123*(1), 176–188.

Helffrich, G., & Kaneshima, S. (2010). Outer-core compositional stratification from observed core wave speed profiles. *Nature*, *468*(7325), 807–810.

Hernlund, J. W., & McNamara, A. K. (2015). 7.11 - The Core–Mantle Boundary Region. In G. Schubert (Ed.), *Treatise on geophysics (second edition)* (Second Edition, pp. 461–519). Elsevier. https://doi.org/10.1016/B978-0-444-53802-4.00136-6

Hernlund, J., & Geissman, M. (2016). Chemical reaction between a basally molten mantle and core. *Abstract #133, 15th symp., study of the earth's deep interior (sedi)*.

Hernlund, J. W., & Jellinek, A. M. (2010). Dynamics and structure of a stirred partially molten ultralow-velocity zone. *Earth and Planetary Science Letters*, *296*(1-2), 1–8.

Hernlund, J. W., & Tackley, P. J. (2007). Some dynamical consequences of partial melting in Earth's deep mantle. *Physics of the Earth and Planetary Interiors*, *162*(1-2), 149–163.

Hernlund, J. W., & Bonati, I. (2019). Modeling Ultralow Velocity Zones as a Thin Chemically Distinct Dense Layer at the Core-Mantle Boundary. *Journal of Geophysical Research: Solid Earth*, *124*(8), 7902–7917.

Herring, T. A., Buffett, B. A., Mathews, P., & Shapiro, I. I. (1991). Forced nutations of the Earth: influence of inner core dynamics: 3. Very long interferometry data analysis. *Journal of Geophysical Research: Solid Earth*, *96*(B5), 8259–8273.

Heyn, B. H., Conrad, C. P., & Trønnes, R. G. (2020). Core-mantle boundary topography and its relation to the viscosity structure of the lowermost mantle. *Earth and Planetary Science Letters*, *543*, 116358.

Hide, R., Clayton, R., Hager, B., Spieth, M., & Voorhdes, C. (1993). Topographic core-mantle coupling and fluctuations in the earth's rotation. *Geophysical Monograph Series*, (76), 107–120.

Hier-Majumder, S., & Revenaugh, J. (2010). Relationship between the viscosity and topography of the ultralow-velocity zone near the core-mantle boundary. *Earth and Planetary Science Letters*, *299*(3), 382–386. https://doi.org/10.1016/j.epsl.2010.09.018

Hinkley, T. K., Lamothe, P. J., Wilson, S. A., Finnegan, D. L., & Gerlach, T. M. (1999). Metal emissions from Kilauea, and a suggested revision of the estimated worldwide metal output by quiescent degassing of volcanoes. *Earth and Planetary Science Letters*, *170*(3), 315–325.

Hirose, K., Morard, G., Sinmyo, R., Umemoto, K., Hernlund, J., Helffrich, G., & Labrosse, S. (2017). Crystallization of silicon dioxide and compositional evolution of the Earth's core. *Nature*, *543*(7643), 99–102.

Hirose, K., Shimizu, N., Van Westrenen, W., & Fei, Y. (2004). Trace element partitioning in Earth's lower mantle and implications for geochemical consequences of partial melting at the core–mantle boundary. *Physics of the Earth and Planetary Interiors*, *146*(1-2), 249–260.

Hirose, K., Takafuji, N., Sata, N., & Ohishi, Y. (2005). Phase transition and density of subducted MORB crust in the lower mantle. *Earth and Planetary Science Letters*, *237*(1-2), 239–251.

Hirose, K., Wood, B., & Vočadlo, L. (2021). Light elements in the Earth's core. *Nature Reviews Earth & Environment*, 1–14.

Hirschmann, M. M., Withers, A., Ardia, P., & Foley, N. (2012). Solubility of molecular hydrogen in silicate melts and consequences for volatile evolution of terrestrial planets. *Earth and Planetary Science Letters*, *345*, 38–48.

Hofmann, A. W. (1997). Mantle geochemistry: The message from oceanic volcanism. *Nature*, *385*(6613), 219–229.

Holme, R. (1998). Electromagnetic core—mantle coupling—I. Explaining decadal changes in the length of day. *Geophysical journal international*, *132*(1), 167–180.

Holzapfel, C., Rubie, D. C., Frost, D. J., & Langenhorst, F. (2005). Fe-Mg interdiffusion in (Mg,Fe)SiO_3 perovskite and lower mantle reequilibration. *Science*, *309*(5741), 1707–1710. https://doi.org/10.1126/science.1111895

Honda, M., McDougall, I., Patterson, D. B., Doulgeris, A., & Clague, D. A. (1993). Noble gases in submarine pillow basalt glasses from Loihi and Kilauea, Hawaii: a solar component in the Earth. *Geochimica et Cosmochimica Acta*, *57*(4), 859–874.

Hopp, J., & Trieloff, M. (2005). Refining the noble gas record of the Réunion mantle plume source: Implications on mantle geochemistry. *Earth and Planetary Science Letters*, *240*(3-4), 573–588.

Humayun, M., Qin, L., & Norman, M. (2004). Geochemical Evidence for Excess Iron in the Mantle Beneath Hawaii. *Science*, *306*, 91. https://doi.org/10.1126/science.1101050

Humayun, M. (2011). A model for osmium isotopic evolution of metallic solids at the core-mantle boundary. *Geochemistry, Geophysics, Geosystems*, *12*(3).

Iizuka-Oku, R., Yagi, T., Gotou, H., Okuchi, T., Hattori, T., & Sano-Furukawa, A. (2017). Hydrogenation of iron in the early stage of Earth's evolution. *Nature communications*, *8*(1), 1–7.

Ireland, T. J., Walker, R. J., & Garcia, M. O. (2009). Highly siderophile element and ^{187}Os isotope systematics of Hawaiian picrites: implications for parental melt composition and source heterogeneity. *Chemical Geology*, *260*(1-2), 112–128.

Ireland, T., Walker, R., & Brandon, A. (2011). ^{186}Os–^{187}Os systematics of Hawaiian picrites revisited: new insights into Os isotopic variations in ocean island basalts. *Geochimica et Cosmochimica Acta*, *75*(16), 4456–4475. https://doi.org/10.1016/j.gca.2011.05.015

Irifune, T., & Tsuchiya, T. (2015). 2.03 - Phase Transitions and Mineralogy of the Lower Mantle. In G. Schubert (Ed.), *Treatise on geophysics (second edition)* (Second Edition, pp. 33–60). Elsevier. https://doi.org/10.1016/B978-0-444-53802-4.00030-0

Irving, J. C., Cottaar, S., & Lekić, V. (2018). Seismically determined elastic parameters for Earth's outer core. *Science advances*, *4*(6), eaar2538.

Ismail-Zadeh, A., & Tackley, P. (2010). *Computational methods for geodynamics*. Cambridge University Press.

Jackson, A. (1997). Time-dependency of tangentially geostrophic core surface motions. *Physics of the earth and planetary interiors*, *103*(3-4), 293–311.

Jackson, C. R., Bennett, N. R., Du, Z., Cottrell, E., & Fei, Y. (2018). Early episodes of high-pressure core formation preserved in plume mantle. *Nature*, *553*(7689), 491–495.

Jackson, L., & Mound, J. (2010). Geomagnetic variation on decadal time scales: What can we learn from Empirical Mode Decomposition? *Geophysical research letters*, *37*(14).

Jacobson, S. A., Rubie, D. C., Hernlund, J., Morbidelli, A., & Nakajima, M. (2017). Formation, stratification, and mixing of the cores of Earth and Venus. *Earth and Planetary Science Letters*, *474*, 375–386.

Jagoutz, E., Palme, H., Baddenhausen, H., Blum, K., Cendales, M., Dreibus, G., Spettel, B., Lorenz, V., & Wänke, H. (1979). The abundances of major, minor and trace elements in the earth's mantle as derived from primitive ultramafic nodules. *Lunar and Planetary Science Conference Proceedings*, *10*, 2031–2050.

Jault, D., & Le Mouël, J.-L. (1990). Core-mantle boundary shape: Constraints inferred from the pressure torque acting between the core and the mantle. *Geophysical Journal International*, *101*(1), 233–241.

Jeanloz, R., & Ahrens, T. J. (1980). Equations of state of FeO and CaO. *Geophysical Journal International*, *62*(3), 505–528.

Jellinek, A. M., & Manga, M. (2004). Links between long-lived hot spots, mantle plumes, D", and plate tectonics. *Reviews of Geophysics*, *42*(3).

Jenny, P., Pope, S. B., Muradoglu, M., & Caughey, D. A. (2001). A hybrid algorithm for the joint PDF equation of turbulent reactive flows. *Journal of Computational Physics*, *166*(2), 218–252.

Jephcoat, A. P., Bouhifd, M. A., & Porcelli, D. (2008). Partitioning experiments in the laser-heated diamond anvil cell: Volatile content in the Earth's core. *Philosophical Transactions of the Royal Society A: Mathematical, Physical and Engineering Sciences*, *366*(1883), 4295–4314.

Jephcoat, A., Mao, H.-k., Finger, L., Cox, D., Hemley, R., & Zha, C.-s. (1987). Pressure-induced structural phase transitions in solid xenon. *Physical review letters*, *59*(23), 2670.

Jurewicz, S., & Jones, J. (1995). Preliminary results of olivine/metal wetting experiments and the direct measurement of metal phase interconnectivity. *Lunar and Planetary Science Conference*, *26*.

Kanda, R., & Stevenson, D. (2006). Suction mechanism for iron entrainment into the lower mantle. *Geophys. Res. Lett.*, *33*, L02310. https://doi.org/10.1029/2005GL025009

Kaneoka, I., & Takaoka, N. (1978). Excess ^{129}Xe and high ^{3}He/^{4}He ratios in olivine phenocrysts of Kapuho lava and xenolithic dunites from Hawaii. *Earth and Planetary Science Letters*, *39*(3), 382–386.

Kaneshima, S. (2016). Seismic scatterers in the mid-lower mantle. *Physics of the Earth and Planetary Interiors*, *257*, 105–114.

Kaneshima, S., & Matsuzawa, T. (2015). Stratification of earth's outermost core inferred from SmKS array data. *Progress in Earth and Planetary Science*, *2*(1), 1–15.

Karato, S.-i. (2008). *Deformation of Earth Materials: An Introduction to the Rheology of Solid Earth*. Cambridge University Press. https://doi.org/10.1017/CBO9780511804892

Karki, B. B., & Stixrude, L. P. (2010). Viscosity of $MgSiO_3$ Liquid at Earth's Mantle Conditions: Implications for an Early Magma Ocean. *Science*, *328*(5979), 740–742. https://doi.org/10.1126/science.1188327

Kellogg, L., & King, S. (1993). Effect of mantle plumes on the growth of D" by reaction between the core and mantle. *Geophys. Res. Lett.*, *20*, 379–382.

Kellogg, L., & Wasserburg, G. (1990). The role of plumes in mantle helium fluxes. *Earth and Planetary Science Letters*, *99*(3), 276–289.

Kellogg, L. H., Hager, B. H., & van der Hilst, R. D. (1999). Compositional stratification in the deep mantle. *Science*, *283*(5409), 1881–1884.

Kleine, T., & Walker, R. J. (2017). Tungsten isotopes in planets. *Annual review of earth and planetary sciences*, *45*, 389–417.

Knittle, E. (1998). The Solid/Liquid Partitioning of Major and Radiogenic Elements at Lower Mantle Pressures: Implications for the Core-Mantle Boundary Region. *The core-mantle boundary region* (pp. 119–130). American Geophysical Union (AGU). https://doi.org/10.1029/GD028p0119

Knittle, E., & Jeanloz, R. (1991). Earth's core-mantle boundary: Results of experiments at high pressures and temperatures. *Science*, *251*(5000), 1438–1443.

Koelemeijer, P., Deuss, A., & Trampert, J. (2012). Normal mode sensitivity to Earth's D" layer and topography on the core-mantle boundary: what we can and cannot see. *Geophysical Journal International*, *190*(1), 553–568.

Komabayashi, T., Hirose, K., Nagaya, Y., Sugimura, E., & Ohishi, Y. (2010). High-temperature compression of ferropericlase and the effect of temperature on iron spin transition. *Earth and Planetary Science Letters*, *297*(3-4), 691–699.

Konter, J. G., Pietruszka, A. J., Hanan, B. B., Finlayson, V. A., Craddock, P. R., Jackson, M. G., & Dauphas, N. (2016). Unusual $\delta^{5}6$Fe values in samoan rejuvenated lavas generated in the mantle. *Earth and Planetary Science Letters*, *450*, 221–232.

Kuang, W., & Bloxham, J. (1997). On the dynamics of topographical core-mantle coupling. *Physics of the earth and planetary interiors*, *99*(3-4), 289–294.

Kuang, W., & Chao, B. F. (2001). Topographic core-mantle coupling in geodynamo modeling. *Geophysical research letters*, *28*(9), 1871–1874.

Kurz, M., Jenkins, W., & Hart, S. (1982). Helium isotopic systematics of oceanic islands and mantle heterogeneity. *Nature*, *297*(5861), 43–47.

Labrosse, S. (2015). Thermal evolution of the core with a high thermal conductivity. *Physics of the Earth and Planetary Interiors*, *247*, 36–55.

Labrosse, S., Hernlund, J., & Coltice, N. (2007). A crystallizing dense magma ocean at the base of the Earth's mantle. *Nature*, *450*(7171), 866–869.

Landeau, M., Deguen, R., Phillips, D., Neufeld, J. A., Lherm, V., & Dalziel, S. B. (2021). Metal-silicate mixing by large Earth-forming impacts. *Earth and Planetary Science Letters*, *564*, 116888.

Landeau, M., Olson, P., Deguen, R., & Hirsh, B. H. (2016). Core merging and stratification following giant impact. *Nature Geoscience*, *9*(10), 786–789.

Lassak, T. M., McNamara, A. K., Garnero, E. J., & Zhong, S. (2010). Core–mantle boundary topography as a possible constraint on lower mantle chemistry and dynamics. *Earth and Planetary Science Letters*, *289*(1-2), 232–241.

Lassak, T. M., McNamara, A. K., & Zhong, S. (2007). Influence of thermochemical piles on topography at Earth's core–mantle boundary. *Earth and Planetary Science Letters*, *261*(3-4), 443–455.

Lassiter, J., & Hauri, E. (1998). Osmium-isotope variations in Hawaiian lavas: evidence for recycled oceanic lithosphere in the Hawaiian plume. *Earth and Planetary Science Letters*, *164*(3-4), 483–496.

LaTourrette, T., & Wasserburg, G. (1998). Mg diffusion in anorthite: Implications for the formation of early solar system planetesimals. *Earth and Planetary Science Letters*, *158*(3-4), 91–108.

Lay, T., & Young, C. J. (1990). The stably-stratified outermost core revisited. *Geophysical Research Letters*, *17*(11), 2001–2004.

Lebrun, T., Massol, H., Chassefière, E., Davaille, A., Marcq, E., Sarda, P., Leblanc, F., & Brandeis, G. (2013). Thermal evolution of an early magma ocean in interaction with the atmosphere. *Journal of Geophysical Research: Planets*, *118*(6), 1155–1176.

Lécuyer, C., Gillet, P., & Robert, F. (1998). The hydrogen isotope composition of seawater and the global water cycle. *Chemical Geology*, *145*(3-4), 249–261.

Lee, C.-T. A., Yin, Q.-z., Lenardic, A., Agranier, A., O'Neill, C. J., & Thiagarajan, N. (2007). Trace-element composition of Fe-rich residual liquids formed by fractional crystallization: Implications for the Hadean magma ocean. *Geochimica et Cosmochimica Acta*, *71*(14), 3601–3615.

Lee, T., Papanastassiou, D., & Wasserburg, G. (1976). Demonstration of ^{26}Mg excess in Allende and evidence for ^{26}Al. *Geophysical Research Letters*, *3*(1), 41–44.

Lenardic, A., & Kaula, W. (1993). A numerical treatment of geodynamic viscous flow problems involving the advection of material interfaces. *Journal of Geophysical Research: Solid Earth*, *98*(B5), 8243–8260.

Lesher, C. E., Dannberg, J., Barfod, G. H., Bennett, N. R., Glessner, J. J., Lacks, D. J., & Brenan, J. M. (2020). Iron isotope fractionation at the core–mantle boundary by thermodiffusion. *Nature Geoscience*, *13*(5), 382–386. https://doi.org/10.1038/s41561-020-0560-y

Li, Y., Vočadlo, L., Sun, T., & Brodholt, J. P. (2020). The earth's core as a reservoir of water. *Nature Geoscience*, 1–6.

Lim, K. W., Bonati, I., & Hernlund, J. W. (2021). A Hybrid Mechanism for Enhanced Core-Mantle Boundary Chemical Interaction. *Geophysical Research Letters*, *48*(23), e2021GL094456. https://doi.org/10.1029/2021GL094456

Lupton, J., & Craig, H. (1975). Excess ^{3}He in oceanic basalts: Evidence for terrestrial primordial helium. *Earth and Planetary Science Letters*, *26*(2), 133–139.

Mabry, J., Lan, T., Burnard, P., & Marty, B. (2013). High-precision helium isotope measurements in air. *Journal of Analytical Atomic Spectrometry*, *28*(12), 1903–1910.

MacPherson, G. J., Davis, A. M., & Zinner, E. K. (1995). The distribution of aluminum-26 in the early solar system—A reappraisal. *Meteoritics*, *30*(4), 365–386.

Malavergne, V., Bureau, H., Raepsaet, C., Gaillard, F., Poncet, M., Surble, S., Sifré, D., Shcheka, S., Fourdrin, C., Deldicque, D., et al. (2019). Experimental constraints on the fate of H and C during planetary core-mantle differentiation. Implications for the Earth. *Icarus*, *321*, 473–485.

Mamajek, E. E. (2009). Initial Conditions of Planet Formation: Lifetimes of Primordial Disks. *AIP Conference Proceedings*, *1158*(1), 3–10. https://doi.org/10.1063/1.3215910

Manga, M., & Jeanloz, R. (1996). Implications of a metal-bearing chemical boundary layer in D" for mantle dynamics. *Geophys. Res. Lett.*, *23*, 3091–3094.

Mann, U., Frost, D. J., & Rubie, D. C. (2008). The wetting ability of Si-bearing liquid Fe-alloys in a solid silicate matrix—percolation during core formation under reducing conditions? *Physics of the Earth and Planetary Interiors*, *167*(1), 1–7. https://doi.org/10.1016/j.pepi.2007.12.002

Mao, W. L., Mao, H.-k., Sturhahn, W., Zhao, J., Prakapenka, V. B., Meng, Y., Shu, J., Fei, Y., & Hemley, R. J. (2006). Iron-rich post-perovskite and the origin of ultralow-velocity zones. *Science*, *312*(5773), 564–565.

Marty, B. (2012). The origins and concentrations of water, carbon, nitrogen and noble gases on Earth. *Earth and Planetary Science Letters*, *313*, 56–66.

Mathews, P., & Guo, J. (2005). Viscoelectromagnetic coupling in precession-nutation theory. *Journal of Geophysical Research: Solid Earth*, *110*(B2).

Matsuda, J., Sudo, M., Ozima, M., Ito, K., Ohtaka, O., & Ito, E. (1993). Noble gas partitioning between metal and silicate under high pressures. *Science*, *259*(5096), 788–790.

Matyska, C., Yuen, D. A., Wentzcovitch, R. M., & Čížková, H. (2011). The impact of variability in the rheological activation parameters on lower-mantle viscosity stratification and its dynamics. *Physics of the Earth and Planetary Interiors*, *188*(1-2), 1–8.

McCoy-West, A. J., Fitton, J. G., Pons, M.-L., Inglis, E. C., & Williams, H. M. (2018). The Fe and Zn isotope composition of deep mantle source regions: Insights from Baffin Island picrites. *Geochimica et Cosmochimica Acta*, *238*, 542–562.

McDonough, W. (2014). 3.16 - compositional model for the earth's core. In H. D. Holland & K. K. Turekian (Eds.), *Treatise on geochemistry (second edition)* (Second Edition, pp. 559–577). Elsevier. https://doi.org/10.1016/B978-0-08-095975-7.00215-1

McDonough, W. F., & Sun, S.-S. (1995). The composition of the Earth. *Chemical geology*, *120*(3-4), 223–253.

McKenzie, D. (1984). The generation and compaction of partially molten rock. *Journal of petrology*, *25*(3), 713–765. https://doi.org/10.1093/petrology/25.3.713

McNamara, A. K., & Zhong, S. (2004). Thermochemical structures within a spherical mantle: Superplumes or piles? *Journal of Geophysical Research: Solid Earth*, *109*(B7).

Melosh, H. J. (1990a). Fluid dynamics of core formation. In H. E. Newsom & J. H. Jones (Eds.), *Origin of the earth* (pp. 231–249). Oxford Univ. Press.

Melosh, H. J. (1990b). Giant impacts and the thermal state of the early Earth. In H. E. Newsom & J. H. Jones (Eds.), *Origin of the earth* (pp. 69–84). Oxford Univ. Press.

Meyer, D., & Jenny, P. (2004). Conservative velocity interpolation for PDF methods. *PAMM: Proceedings in Applied Mathematics and Mechanics*, *4*(1), 466–467.

Minarik, W. G., Ryerson, F. J., & Watson, E. B. (1996). Textural entrapment of core-forming melts. *Science*, *272*(5261), 530–533.

Montelli, R., Nolet, G., Dahlen, F., Masters, G., Engdahl, E. R., & Hung, S.-H. (2004). Finite-frequency tomography reveals a variety of plumes in the mantle. *Science*, *303*(5656), 338–343.

Morelli, A., & Dziewonski, A. M. (1987). Topography of the core–mantle boundary and lateral homogeneity of the liquid core. *Nature*, *325*(6106), 678–683.

Moresi, L.-N., & Solomatov, V. (1995). Numerical investigation of 2D convection with extremely large viscosity variations. *Physics of Fluids*, *7*(9), 2154–2162.

Morgan, J. W., Horan, M. F., Walker, R. J., & Grossman, J. N. (1995). Rheniumum concentration and isotope systematics in group IIAB iron meteorites. *Geochimica et Cosmochimica Acta*, *59*(11), 2331–2344.

Morgan, W. (1971). Convection plumes in the lower mantle. *Nature*, *230*, 42–43.

Morris, S. (1982). The effects of a strongly temperature-dependent viscosity on slow flow past a hot sphere. *Journal of Fluid Mechanics*, *124*, 1–26.

Morris, S., & Canright, D. (1984). A boundary-layer analysis of Benard convection in a fluid of strongly temperature-dependent viscosity. *Physics of the Earth and planetary interiors*, *36*(3-4), 355–373.

Mound, J., & Buffett, B. (2007). Viscosity of the Earth's fluid core and torsional oscillations. *Journal of Geophysical Research: Solid Earth*, *112*(B5).

Mound, J. E., & Buffett, B. A. (2006). Detection of a gravitational oscillation in length-of-day. *Earth and Planetary Science Letters*, *243*(3-4), 383–389.

Muir, J. M., & Brodholt, J. P. (2015a). Elastic properties of ferropericlase at lower mantle conditions and its relevance to ULVZs. *Earth and Planetary Science Letters*, *417*, 40–48.

Muir, J. M., & Brodholt, J. P. (2015b). Elastic properties of ferrous bearing $MgSiO_3$ and their relevance to ULVZs. *Geophysical Journal International*, *201*(1), 496–504.

Muir, J. M., & Brodholt, J. P. (2020). Ferric iron in bridgmanite and implications for ULVZs. *Physics of the Earth and Planetary Interiors*, *306*, 106505.

Mukhopadhyay, S. (2012). Early differentiation and volatile accretion recorded in deep-mantle neon and xenon. *Nature*, *486*(7401), 101–104.

Mundl-Petermeier, A., Walker, R., Fischer, R., Lekic, V., Jackson, M., & Kurz, M. (2020). Anomalous ^{182}W in high ^{3}He/^{4}He ocean island basalts: Fingerprints of Earth's core? *Geochimica et Cosmochimica Acta*, *271*, 194–211.

Mundl-Petermeier, A., Walker, R., Jackson, M., Blichert-Toft, J., Kurz, M., & Halldórsson, S. A. (2019). Temporal evolution of primordial tungsten-182 and ^{3}He/^{4}He signatures in the Iceland mantle plume. *Chemical Geology*, *525*, 245–259.

Mundl-Petermeier, A., Touboul, M., Jackson, M., Day, J., Kurz, M., Lekic, V., Helz, R., & J. Walker, R. (2017). Tungsten-182 heterogeneity in modern ocean island basalts. *Science*, *356*, 66–69. https://doi.org/10.1126/science.aal4179

Nakajima, M., & Stevenson, D. J. (2015). Melting and mixing states of the Earth's mantle after the Moon-forming impact. *Earth and Planetary Science Letters*, *427*, 286–295.

Nataf, H., & Richter, F. (1982). Convection experiments in fluids with highly temperature-dependent viscosity and the thermal evolution of the planets. *Physics of the Earth and planetary interiors*, *29*(3-4), 320–329.

Nishio-Hamane, D., Yagi, T., Sata, N., Fujita, T., & Okada, T. (2010). No reactions observed in Xe-Fe system even at Earth core pressures. *Geophysical Research Letters*, *37*(4).

Ogawa, M. (2000). Coupled magmatism–mantle convection system with variable viscosity. *Tectonophysics*, *322*(1-2), 1–18.

Ogawa, M., Schubert, G., & Zebib, A. (1991). Numerical simulations of three-dimensional thermal convection in a fluid with strongly temperature-dependent viscosity. *Journal of fluid mechanics*, *233*, 299–328.

Ohtani, E., & Ringwood, A. (1984). Composition of the core, I. Solubility of oxygen in molten iron at high temperatures. *Earth and planetary science letters*, *71*(1), 85–93.

Ohtani, E. (1985). The primodial terrestrial magma ocean and its implication for stratification of the mantle. *Physics of the Earth and Planetary Interiors*, *38*(1), 70–80.

Ohtani, E., & Sawamoto, H. (1987). Melting experiment on a model chondritic mantle composition at 25 GPa. *Geophysical Research Letters*, *14*(7), 733–736.

Okuchi, T. (1997). Hydrogen partitioning into molten iron at high pressure: Implications for Earth's core. *Science*, *278*(5344), 1781–1784.

Olson, P. (2015). 8.01 - Core Dynamics: An Introduction and Overview. In G. Schubert (Ed.), *Treatise on geophysics (second edition)* (Second Edition, pp. 1–25). Elsevier. https://doi.org/10.1016/B978-0-444-53802-4.00137-8

Olson, P., Schubert, G., & Anderson, C. (1987). Plume formation in the D"-layer and the roughness of the core–mantle boundary. *Nature*, *327*(6121), 409–413.

Olson, P., & Sharp, Z. D. (2018). Hydrogen and helium ingassing during terrestrial planet accretion. *Earth and Planetary Science Letters*, *498*, 418–426.

O'Rourke, J., & Stevenson, D. (2016). Powering Earth's dynamo with magnesium precipitation from the core. *Nature*, *529*, 387–389. https://doi.org/10.1038/nature16495

Otsuka, K., & Karato, S.-i. (2012). Deep penetration of molten iron into the mantle caused by a morphological instability. *Nature*, *492*(7428), 243–246. https://doi.org/10.1038/nature11663

Ozawa, H., Hirose, K., Mitome, M., Bando, Y., Sata, N., & Ohishi, Y. (2008). Chemical equilibrium between ferropericlase and molten iron to 134 GPa and implications for iron content at the bottom of the mantle. *Geophysical Research Letters*, *35*(5).

Pahlevan, K., Schaefer, L., & Hirschmann, M. M. (2019). Hydrogen isotopic evidence for early oxidation of silicate Earth. *Earth and Planetary Science Letters*, *526*, 115770.

Patankar, S. V. (2018). *Numerical heat transfer and fluid flow*. CRC press.

Pepin, R. O. (1992). ORIGIN OF NOBLE GASES IN THE TERRESTRIAL PLANETS. *Annual Review of Earth and Planetary Sciences*, *20*(1), 389–430. https://doi.org/10.1146/annurev.ea.20.050192.002133

Péron, S., Moreira, M., Colin, A., Arbaret, L., Putlitz, B., & Kurz, M. D. (2016). Neon isotopic composition of the mantle constrained by single vesicle analyses. *Earth and Planetary Science Letters*, *449*, 145–154.

Petford, N., Yuen, D., Rushmer, T., Brodholt, J., & Stackhouse, S. (2005). Shear-induced material transfer across the core-mantle boundary aided by the post-perovskite phase transition. *Earth, planets and space*, *57*(5), 459–464.

Pető, M. K., Mukhopadhyay, S., & Kelley, K. A. (2013). Heterogeneities from the first 100 million years recorded in deep mantle noble gases from the Northern Lau Back-arc Basin. *Earth and Planetary Science Letters*, *369*, 13–23.

Piet, H., Badro, J., Nabiei, F., Dennenwaldt, T., Shim, S.-H., Cantoni, M., Hébert, C., & Gillet, P. (2016). Spin and valence dependence of iron partitioning in Earth's deep mantle. *Proceedings of the National Academy of Sciences*, *113*(40), 11127–11130.

Poirier, J.-P., & le Mouël, J.-L. (1992). Does infiltration of core material into the lower mantle affect the observed geomagnetic field? *Physics of the earth and planetary interiors*, *73*(1-2), 29–37. https://doi.org/10.1016/0031-9201(92)90105-5

Poirier, J., Malavergne, V., & Mouël, J. L. (1998). Is there a thin electrically conducting layer at the base of the mantle? In M. Gurnis, M. Wysession, E. Knittle, & B. Buffett (Eds.), *The core-mantle boundary region* (pp. 131–137). American Geophysical Union Monograph.

Porcelli, D., & Wasserburg, G. (1995). Mass transfer of helium, neon, argon, and xenon through a steady-state upper mantle. *Geochimica et Cosmochimica Acta*, *59*(23), 4921–4937.

Poreda, R., & Farley, K. (1992). Rare gases in Samoan xenoliths. *Earth and Planetary Science Letters*, *113*(1-2), 129–144.

Pozzo, M., Davies, C., Gubbins, D., & Alfe, D. (2012). Thermal and electrical conductivity of iron at Earth's core conditions. *Nature*, *485*(7398), 355–358.

Puchtel, I. S., Brandon, A. D., Humayun, M., & Walker, R. J. (2005). Evidence for the early differentiation of the core from Pt–Re–Os isotope systematics of 2.8-Ga komatiites. *Earth and Planetary Science Letters*, *237*(1-2), 118–134.

Puchtel, I. S., Mundl-Petermeier, A., Horan, M., Hanski, E. J., Blichert-Toft, J., & Walker, R. J. (2020). Ultra-depleted 2.05 Ga komatiites of Finnish Lapland: Products of grainy late accretion or core-mantle interaction? *Chemical Geology*, *554*, 119801.

Pusok, A. E., Kaus, B. J., & Popov, A. A. (2017). On the quality of velocity interpolation schemes for marker-in-cell method and staggered grids. *Pure and Applied Geophysics*, *174*(3), 1071–1089.

Qin, L., & Humayun, M. (2008). The Fe/Mn ratio in MORB and OIB determined by ICP-MS. *Geochimica et Cosmochimica Acta*, *72*(6), 1660–1677.

Raquin, A., & Moreira, M. (2009). Atmospheric $^{38}Ar/^{36}Ar$ in the mantle: Implications for the nature of the terrestrial parent bodies. *Earth and Planetary Science Letters*, *287*(3-4), 551–558.

Raymond, S. N., Quinn, T., & Lunine, J. I. (2006). High-resolution simulations of the final assembly of Earth-like planets I. Terrestrial accretion and dynamics. *Icarus*, *183*(2), 265–282.

Reisberg, L., Zindler, A., Marcantonio, F., White, W., Wyman, D., & Weaver, B. (1993). Os isotope systematics in ocean island basalts. *Earth and Planetary Science Letters*, *120*(3-4), 149–167.

Reynolds, O. (1886). IV. On the theory of lubrication and its application to Mr. Beauchamp tower's experiments, including an experimental determination of the viscosity of olive oil. *Philosophical transactions of the Royal Society of London*, (177), 157–234.

Richter, F. M., Davis, A. M., DePaolo, D. J., & Watson, E. B. (2003). Isotope fractionation by chemical diffusion between molten basalt and rhyolite. *Geochimica et Cosmochimica Acta*, *67*(20), 3905–3923.

Richter, F. M., Nataf, H.-C., & Daly, S. F. (1983). Heat transfer and horizontally averaged temperature of convection with large viscosity variations. *Journal of Fluid Mechanics*, *129*, 173–192.

Ricolleau, A., Fei, Y., Corgne, A., Siebert, J., & Badro, J. (2011). Oxygen and silicon contents of Earth's core from high pressure metal–silicate partitioning experiments. *Earth and Planetary Science Letters*, *310*(3-4), 409–421.

Ringwood, A. E. (1979). *Origin of the Earth and Moon*. Springer-Verlag New York. https://doi.org/10.1007/978-1-4612-6167-4

Rizo, H., Boyet, M., Blichert-Toft, J., & Rosing, M. T. (2013). Early mantle dynamics inferred from ^{142}Nd variations in Archean rocks from southwest Greenland. *Earth and Planetary Science Letters*, *377*, 324–335.

Roberts, P., Yu, Z., & Russell, C. (2007). On the 60-year signal from the core. *Geophysical and Astrophysical Fluid Dynamics*, *101*(1), 11–35.

Roe, P. L. (1986). Characteristic-based schemes for the Euler equations. *Annual review of fluid mechanics*, *18*(1), 337–365.

Ross, A., Thybo, H., & Solidilov, L. (2004). Reflection seismic profiles of the core-mantle boundary. *Journal of Geophysical Research: Solid Earth*, *109*(B8).

Rost, S., Garnero, E. J., & Williams, Q. (2006). Fine-scale ultralow-velocity zone structure from high-frequency seismic array data. *Journal of Geophysical Research: Solid Earth*, *111*(B9).

Rubie, D. C., Gessmann, C. K., & Frost, D. J. (2004). Partitioning of oxygen during core formation on the Earth and Mars. *Nature*, *429*(6987), 58–61.

Rubie, D. C., Jacobson, S. A., Morbidelli, A., O'Brien, D. P., Young, E. D., de Vries, J., Nimmo, F., Palme, H., & Frost, D. J. (2015). Accretion and differentiation of the terrestrial planets with implications for the compositions of early-formed Solar System bodies and accretion of water. *Icarus*, *248*, 89–108.

Rubie, D. (2007). Formation of Earth's core. *Evolution of the Earth*, 51–90.

Rubie, D., Melosh, H., Reid, J., Liebske, C., & Righter, K. (2003). Mechanisms of metal–silicate equilibration in the terrestrial magma ocean. *Earth and Planetary Science Letters*, *205*(3-4), 239–255.

Rubie, D., Nimmo, F., & Melosh, H. (2015). 9.03 - Formation of the Earth's Core. In G. Schubert (Ed.), *Treatise on geophysics (second edition)* (Second Edition, pp. 43–79). Elsevier. https://doi.org/10.1016/B978-0-444-53802-4.00154-8

Ruzicka, A., Snyder, G. A., & Taylor, L. A. (2001). Comparative geochemistry of basalts from the Moon, Earth, HED asteroid, and Mars: Implications for the origin of the Moon. *Geochimica et Cosmochimica Acta*, *65*(6), 979–997.

Sakai, T., Kondo, T., Ohtani, E., Terasaki, H., Endo, N., Kuba, T., Suzuki, T., & Kikegawa, T. (2006). Interaction between iron and post-perovskite at core-mantle boundary and core signature in plume source region. *Geophysical research letters*, *33*(15).

Sarda, P., Moreira, M., Staudacher, T., Schilling, J.-G., & Allègre, C. J. (2000). Rare gas systematics on the southernmost Mid-Atlantic Ridge: Constraints on the lower mantle and the Dupal source. *Journal of Geophysical Research: Solid Earth*, *105*(B3), 5973–5996.

Sasaki, S. (1990). The primary solar-type atmosphere surrounding the accreting Earth: H_2O-induced high surface temperature. In H. E. Newsom & J. H. Jones (Eds.), *Origin of the earth* (pp. 195–209).

Sasaki, S., & Nakazawa, K. (1986). Metal-silicate fractionation in the growing Earth: Energy source for the terrestrial magma ocean. *Journal of Geophysical Research: Solid Earth*, *91*(B9), 9231–9238.

Schlaphorst, D., Thomas, C., Holme, R., & Abreu, R. (2016). Investigation of core–mantle boundary topography and lowermost mantle with P4KP waves. *Geophysical Journal International*, *204*(2), 1060–1071.

Schlichting, H. E., & Mukhopadhyay, S. (2018). Atmosphere impact losses. *Space Science Reviews*, *214*(1), 1–31.

Schubert, G., Turcotte, D. L., & Olson, P. (2001). *Mantle convection in the Earth and planets*. Cambridge University Press.

Schuessler, J. A., Schoenberg, R., & Sigmarsson, O. (2009). Iron and lithium isotope systematics of the Hekla volcano, Iceland—evidence for Fe isotope fractionation during magma differentiation. *Chemical Geology*, *258*(1-2), 78–91.

Secco, R. (1995). Viscosity of the outer core. *Mineral Physics and Crystallography, A Handbook of Physical Constants*, *2*, 218–226.

Shannon, M., & Agee, C. (1996). High pressure constraints on percolative core formation. *Geophysical Research Letters*, *23*(20), 2717–2720.

Shannon, M., & Agee, C. (1998). Percolation of core melts at lower mantle conditions. *Science*, *280*(5366), 1059–1061.

Sharp, Z. D. (2017). Nebular ingassing as a source of volatiles to the terrestrial planets. *Chemical Geology*, *448*, 137–150.

Shaw, D. M. (1970). Trace element fractionation during anatexis. *Geochimica et Cosmochimica Acta*, *34*(2), 237–243.

Shi, C. Y., Zhang, L., Yang, W., Liu, Y., Wang, J., Meng, Y., Andrews, J. C., & Mao, W. L. (2013). Formation of an interconnected network of iron melt at Earth's lower mantle conditions. *Nature Geoscience*, *6*(11), 971–975.

Shibazaki, Y., Ohtani, E., Terasaki, H., Suzuki, A., & Funakoshi, K.-i. (2009). Hydrogen partitioning between iron and ringwoodite: Implications for water transport into the Martian core. *Earth and Planetary Science Letters*, *287*(3-4), 463–470.

Sleep, N. H. (1988). Gradual entrainment of a chemical layer at the base of the mantle by overlying convection. *Geophysical Journal International*, *95*(3), 437–447.

Soderman, C. R., Matthews, S., Shorttle, O., Jackson, M. G., Ruttor, S., Nebel, O., Turner, S., Beier, C., Millet, M.-A., Widom, E., et al. (2021). Heavy $\delta^5$7Fe in ocean island basalts: A non-unique signature of processes and source lithologies in the mantle. *Geochimica et Cosmochimica Acta*, *292*, 309–332.

Solomatov, V. (2015). 9.04 - Magma Oceans and Primordial Mantle Differentiation. In G. Schubert (Ed.), *Treatise on geophysics (second edition)* (Second Edition, pp. 81–104). Elsevier. https://doi.org/10.1016/B978-0-444-53802-4.00155-X

Solomatov, V. S., & Stevenson, D. J. (1993). Suspension in convective layers and style of differentiation of a terrestrial magma ocean. *Journal of Geophysical Research: Planets*, *98*(E3), 5375–5390.

Solomatov, V. (1995). Scaling of temperature-and stress-dependent viscosity convection. *Physics of Fluids*, *7*(2), 266–274.

Solomon, S. C. (1979). Formation, history and energetics of cores in the terrestrial planets. *Physics of the Earth and Planetary Interiors*, *19*(2), 168–182.

Souriau, A., & Poupinet, G. (1991). The velocity profile at the base of the liquid core from PKP (BC+ Cdiff) data: an argument in favour of radial inhomogeneity. *Geophysical Research Letters*, *18*(11), 2023–2026.

Šrámek, O., Milelli, L., Ricard, Y., & Labrosse, S. (2012). Thermal evolution and differentiation of planetesimals and planetary embryos. *Icarus*, *217*(1), 339–354.

Stevenson, D. (1981). Models of the Earth's core. *Science*, *214*(4521), 611–619.

Stevenson, D. (1987). Limits on lateral density and velocity variations in the Earth's outer core. *Geophysical Journal International*, *88*(1), 311–319.

Stökl, A., Dorfi, E. A., Johnstone, C. P., & Lammer, H. (2016). Dynamical accretion of primordial atmospheres around planets with masses between 0.1 and 5 $M_\oplus$ in the habitable zone. *The Astrophysical Journal*, *825*(2), 86.

Sze, E. K., & van der Hilst, R. D. (2003). Core mantle boundary topography from short period PcP, PKP, and PKKP data. *Physics of the Earth and Planetary Interiors*, *135*(1), 27–46.

Tackley, P. J. (1998). Three-Dimensional Simulations of Mantle Convection with a Thermo-Chemical Basal Boundary Layer: D"? *The core-mantle boundary region* (pp. 231–253). American Geophysical Union (AGU). https://doi.org/10.1029/GD028p0231

Tackley, P. J., & King, S. D. (2003). Testing the tracer ratio method for modeling active compositional fields in mantle convection simulations. *Geochemistry, Geophysics, Geosystems*, *4*(4).

Tagawa, S., Sakamoto, N., Hirose, K., Yokoo, S., Hernlund, J., Ohishi, Y., & Yurimoto, H. (2021). Experimental evidence for hydrogen incorporation into Earth's core. *Nature communications*, *12*(1), 1–8.

Takafuji, N., Hirose, K., Mitome, M., & Bando, Y. (2005). Solubilities of O and Si in liquid iron in equilibrium with (Mg, Fe)SiO_3 perovskite and the light elements in the core. *Geophysical Research Letters*, *32*(6).

Takafuji, N., Hirose, K., Ono, S., Xu, F., Mitome, M., & Bando, Y. (2004). Segregation of core melts by permeable flow in the lower mantle. *Earth and Planetary Science Letters*, *224*(3), 249–257. https://doi.org/10.1016/j.epsl.2004.05.016

Tanaka, S. (2007). Possibility of a low P-wave velocity layer in the outermost core from global SmKS waveforms. *Earth and Planetary Science Letters*, *259*(3-4), 486–499.

Tanaka, S. (2010). Constraints on the core-mantle boundary topography from P4KP-PcP differential travel times. *Journal of Geophysical Research: Solid Earth*, *115*(B4).

Tarduno, J. A., Cottrell, R. D., Watkeys, M. K., Hofmann, A., Doubrovine, P. V., Mamajek, E. E., Liu, D., Sibeck, D. G., Neukirch, L. P., & Usui, Y. (2010). Geodynamo, solar wind, and magnetopause 3.4 to 3.45 billion years ago. *science*, *327*(5970), 1238–1240.

Ten, A., Yuen, D. A., Podladchikov, Y. Y., Larsen, T. B., Pachepsky, E., & Malevsky, A. V. (1997). Fractal features in mixing of non-Newtonian and Newtonian mantle convection. *Earth and planetary science letters*, *146*(3-4), 401–414.

Teng, F.-Z., Dauphas, N., & Helz, R. T. (2008). Iron isotope fractionation during magmatic differentiation in Kilauea Iki lava lake. *Science*, *320*(5883), 1620–1622.

Terasaki, H., Frost, D. J., Rubie, D. C., & Langenhorst, F. (2005). The effect of oxygen and sulphur on the dihedral angle between Fe–O–S melt and silicate minerals at high pressure: implications for Martian core formation. *Earth and Planetary Science Letters*, *232*(3-4), 379–392.

Thielmann, M., Golabek, G. J., & Marquardt, H. (2020). Ferropericlase control of lower mantle rheology: Impact of phase morphology. *Geochemistry, Geophysics, Geosystems*, *21*(2), e2019GC008688.

Tonks, W. B., & Melosh, H. J. (1993). Magma ocean formation due to giant impacts. *Journal of Geophysical Research: Planets*, *98*(E3), 5319–5333.

Touboul, M., Liu, J., O'Neil, J., Puchtel, I. S., & Walker, R. J. (2014). New insights into the Hadean mantle revealed by ^{182}W and highly siderophile element abundances of supracrustal rocks from the Nuvvuagittuq Greenstone Belt, Quebec, Canada. *Chemical Geology*, *383*, 63–75.

Trieloff, M., Kunz, J., & Allègre, C. J. (2002). Noble gas systematics of the Réunion mantle plume source and the origin of primordial noble gases in Earth's mantle. *Earth and Planetary Science Letters*, *200*(3-4), 297–313.

Trieloff, M., Kunz, J., Clague, D. A., Harrison, D., & Allègre, C. J. (2000). The nature of pristine noble gases in mantle plumes. *Science*, *288*(5468), 1036–1038.

Trompert, R., & Hansen, U. (1998). On the Rayleigh number dependence of convection with a strongly temperature-dependent viscosity. *Physics of Fluids*, *10*(2), 351–360.

Tsuchiya, T., Wentzcovitch, R. M., Da Silva, C. R., & De Gironcoli, S. (2006). Spin transition in magnesiowüstite in Earth's lower mantle. *Physical Review Letters*, *96*(19), 198501.

Turcotte, D. L., & Schubert, G. (2002). *Geodynamics*. Cambridge university press.

Umemoto, K., & Hirose, K. (2015). Liquid iron-hydrogen alloys at outer core conditions by first-principles calculations. *Geophysical Research Letters*, *42*(18), 7513–7520.

Umemoto, K., & Hirose, K. (2020). Chemical compositions of the outer core examined by first principles calculations. *Earth and Planetary Science Letters*, *531*, 116009.

Urey, H. C. (1955). The cosmic abundances of potassium, uranium, and thorium and the heat balances of the Earth, the Moon, and Mars. *Proceedings of the National Academy of Sciences of the United States of America*, *41*(3), 127.

Valley, J. W., Peck, W. H., King, E. M., & Wilde, S. A. (2002). A cool early Earth. *Geology*, *30*(4), 351–354.

van der Hist, R., Engdahl, R., Spakman, W., & Nolet, G. (1991). Tomographic imaging of subducted lithosphere below northwest pacific island arcs. *Nature*, *353*(6339), 37–43.

van der Meer, D. G., Spakman, W., Van Hinsbergen, D. J., Amaru, M. L., & Torsvik, T. H. (2010). Towards absolute plate motions constrained by lower-mantle slab remnants. *Nature Geoscience*, *3*(1), 36–40.

Van Keken, P., King, S., Schmeling, H., Christensen, U., Neumeister, D., & Doin, M.-P. (1997). A comparison of methods for the modeling of thermochemical convection. *Journal of Geophysical Research: Solid Earth*, *102*(B10), 22477–22495.

Van Orman, J. A., & Crispin, K. L. (2010). Diffusion in oxides. *Reviews in Mineralogy and Geochemistry*, *72*(1), 757–825.

Van Orman, J. A., Keshav, S., & Fei, Y. (2008). High-pressure solid/liquid partitioning of Os, Re and Pt in the Fe–S system. *Earth and Planetary Science Letters*, *274*(1-2), 250–257. https://doi.org/10.1016/j.epsl.2008.07.029

Vogt, M., Trieloff, M., Ott, U., Hopp, J., & Schwarz, W. H. (2021). Solar noble gases in an iron meteorite indicate terrestrial mantle signatures derive from Earth's core. *Communications Earth & Environment*, *2*(1), 1–7. https://doi.org/10.1038/s43247-021-00162-2

von Bargen, N., & Waff, H. S. (1986). Permeabilities, interfacial areas and curvatures of partially molten systems: Results of numerical computations of equilibrium microstructures. *Journal of Geophysical Research: Solid Earth*, *91*(B9), 9261–9276.

Wade, J., & Wood, B. (2005). Core formation and the oxidation state of the Earth. *Earth and Planetary Science Letters*, *236*(1-2), 78–95.

Walker, D. (2000). Core participation in mantle geochemistry: geochemical society Ingerson lecture, GSA Denver, October 1999. *Geochimica et Cosmochimica Acta*, *64*(17), 2897–2911.

Walker, R. J., Morgan, J. W., Beary, E. S., Smoliar, M. I., Czamanske, G. K., & Horan, M. F. (1997). Applications of the ^{190}Pt–^{186}Os isotope system to geochemistry and cosmochemistry. *Geochimica et Cosmochimica Acta*, *61*(22), 4799–4807.

Walker, R., Horan, M., Morgan, J., Becker, H., Grossman, J., & Rubin, A. (2002). Comparative ^{187}Re-^{187}Os systematics of chondrites: Implications regarding early solar system processes. *Geochimica et Cosmochimica Acta*, *66*(23), 4187–4201.

Watson, H. C., & Roberts, J. J. (2011). Connectivity of core forming melts: Experimental constraints from electrical conductivity and X-ray tomography. *Physics of the Earth and Planetary Interiors*, *186*(3-4), 172–182.

Weinberg, R. F., & Schmeling, H. (1992). Polydiapirs: Multiwavelength gravity structures. *Journal of Structural Geology*, *14*(4), 425–436.

Wetherill, G. W. (1980). Formation of the terrestrial planets. *Annual review of astronomy and astrophysics*, *18*(1), 77–113.

Wetherill, G. (1986). Accumulation of the terrestrial planets and implications concerning lunar origin. *Origin of the Moon*, 519–550.

Whaler, K. (1980). Does the whole of the Earth's core convect? *Nature*, *287*(5782), 528–530.

Wheeler, K. T., Walker, D., Fei, Y., Minarik, W. G., & McDonough, W. F. (2006). Experimental partitioning of uranium between liquid iron sulfide and liquid silicate: Implications for radioactivity in the Earth's core. *Geochimica et Cosmochimica Acta*, *70*(6), 1537–1547.

Wicks, J., Jackson, J., & Sturhahn, W. (2010). Very low sound velocities in iron-rich (Mg, Fe)O: Implications for the core-mantle boundary region. *Geophysical Research Letters*, *37*(15).

Williams, Q., & Garnero, E. J. (1996). Seismic evidence for partial melt at the base of Earth's mantle. *Science*, *273*(5281), 1528–1530. https://doi.org/10.1126/science.273.5281.1528

Wolfe, C. J., Bjarnason, I. T., VanDecar, J. C., & Solomon, S. C. (1997). Seismic structure of the Iceland mantle plume. *Nature*, *385*(6613), 245–247.

Wood, B. J., Walter, M. J., & Wade, J. (2006). Accretion of the Earth and segregation of its core. *Nature*, *441*(7095), 825–833.

Wu, J., Desch, S. J., Schaefer, L., Elkins-Tanton, L. T., Pahlevan, K., & Buseck, P. R. (2018). Origin of Earth's water: Chondritic inheritance plus nebular ingassing and storage of hydrogen in the core. *Journal of Geophysical Research: Planets*, *123*(10), 2691–2712.

Xiong, Z., Tsuchiya, T., & Van Orman, J. A. (2021). Helium and argon partitioning between liquid iron and silicate melt at high pressure. *Geophysical Research Letters*, *48*(3), e2020GL090769.

Yamazaki, D., & Karato, S.-i. (2001). Some mineral physics constraints on the rheology and geothermal structure of Earth's lower mantle. *American Mineralogist*, *86*(4), 385–391.

Yamazaki, D., Yoshino, T., Matsuzaki, T., Katsura, T., & Yoneda, A. (2009). Texture of (Mg,Fe)SiO_3 perovskite and ferro-periclase aggregate: Implications for rheology of the lower mantle. *Physics of the Earth and Planetary Interiors*, *174*(1-4), 138–144.

Yokochi, R., & Marty, B. (2004). A determination of the neon isotopic composition of the deep mantle. *Earth and Planetary Science Letters*, *225*(1-2), 77–88.

Yokoyama, Y., & Yukutake, T. (1991). Sixty year variation in a time series of the geomagnetic Gauss coefficients between 1910 and 1983. *Journal of geomagnetism and geoelectricity*, *43*(7), 563–584.

Yoshida, M. (2008). Core-mantle boundary topography estimated from numerical simulations of instantaneous mantle flow. *Geochemistry, Geophysics, Geosystems*, *9*(7).

Yoshino, T. (2019). Penetration of molten iron alloy into the lower mantle phase. *Comptes Rendus Geoscience*, *351*(2-3), 171–181.

Yoshino, T., Makino, Y., Suzuki, T., & Hirata, T. (2020). Grain boundary diffusion of W in lower mantle phase with implications for isotopic heterogeneity in oceanic island basalts by core-mantle interactions. *Earth and Planetary Science Letters*, *530*, 115887.

Yoshino, T., Walter, M. J., & Katsura, T. (2003). Core formation in planetesimals triggered by permeable flow. *Nature*, *422*(6928), 154–157.

Yoshino, T., Walter, M. J., & Katsura, T. (2004). Connectivity of molten fe alloy in peridotite based on in situ electrical conductivity measurements: Implications for core formation in terrestrial planets. *Earth and Planetary Science Letters*, *222*(2), 625–643.

Yu, S., & Garnero, E. J. (2018). Ultralow velocity zone locations: A global assessment. *Geochemistry, Geophysics, Geosystems*, *19*(2), 396–414.

Yuan, L., & Steinle-Neumann, G. (2020). Strong sequestration of hydrogen into the Earth's core during planetary differentiation. *Geophysical Research Letters*, *47*(15), e2020GL088303.

Yudovskaya, M. A., Tessalina, S., Distler, V. V., Chaplygin, I. V., Chugaev, A. V., & Dikov, Y. P. (2008). Behavior of highly-siderophile elements during magma degassing: A case study at the Kudryavy volcano. *Chemical Geology*, *248*(3-4), 318–341.

Yuen, D. A., Sabadini, R., & Boschi, E. V. (1982). Viscosity of the lower mantle as inferred from rotational data. *Journal of Geophysical Research: Solid Earth*, *87*(B13), 10745–10762.

Zahnle, K. J., Kasting, J. F., & Pollack, J. B. (1988). Evolution of a steam atmosphere during earth's accretion. *Icarus*, *74*(1), 62–97.

Zhang, Y., & Yin, Q.-Z. (2012). Carbon and other light element contents in the Earth's core based on first-principles molecular dynamics. *Proceedings of the National Academy of Sciences*, *109*(48), 19579–19583.

Zhong, S. (2006). Constraints on thermochemical convection of the mantle from plume heat flux, plume excess temperature, and upper mantle temperature. *Journal of Geophysical Research: Solid Earth*, *111*(B4).

Zhong, S., & Hager, B. H. (2003). Entrainment of a dense layer by thermal plumes. *Geophysical Journal International*, *154*(3), 666–676.